Urban Microclimatic Response to Landscape Changes via Land-Atmosphere Interactions

by

Jiyun Song

A Dissertation Presented in Partial Fulfillment
of the Requirements for the Degree
Doctor of Philosophy

Approved October 2016 by the
Graduate Supervisory Committee:

Zhihua Wang, Chair
Enrique R. Vivoni
Giuseppe Mascaro
Soe W. Myint
David Sailor

ARIZONA STATE UNIVERSITY

December 2016

ABSTRACT

Rapid urban expansion and the associated landscape modifications have led to significant changes of surface processes in built environments. These changes further interact with the overlying atmospheric boundary layer and strongly modulate urban microclimate. To capture the impacts of urban land surface processes on urban boundary layer dynamics, a coupled urban land-atmospheric modeling framework has been developed. The urban land surface is parameterized by an advanced single-layer urban canopy model (SLUCM) with realistic representations of urban green infrastructures such as lawn, tree, and green roof, etc. The urban atmospheric boundary layer is simulated by a single column model (SCM) with both convective and stable schemes. This coupled SLUCM-SCM framework can simulate the time evolution and vertical profile of different meteorological variables such as virtual potential temperature, specific humidity and carbon dioxide concentration. The coupled framework has been calibrated and validated in the metropolitan Phoenix area, Arizona. To quantify the model sensitivity, an advanced stochastic approach based on Markov-Chain Monte Carlo procedure has been applied. It is found that the development of urban boundary layer is highly sensitive to surface characteristics of built terrains, including urban land use, geometry, roughness of momentum, and vegetation fraction. In particular, different types of urban vegetation (mesic/xeric) affect the boundary layer dynamics through different mechanisms. Furthermore, this framework can be implanted into large-scale models such as Weather Research and Forecasting model to assess the impact of urbanization on regional climate.

ACKNOWLEDGMENTS

First of all, I would like to thank my supervisor Prof. Zhihua Wang. It is my honor to be the first PhD student of such as a passionate and productive young scientist. I appreciate all his efforts in guiding and training me in creative thinking, critical reasoning, professional writing, etc. during my PhD study period. I also appreciate all his supports when I was chasing academic opportunities such as conferences, graduate grants, etc. With his guidance and help, I have been growing up as a better academic researcher with rich experiences in both numerical modeling and field experiments. Besides, I would like to thank all the distinguished professors in my graduate committee including Prof. Enrique R. Vivoni, Prof. Giuseppe Mascaro, Prof. Soe W. Myint, and Prof. David Sailor for their valuable supports, advices and encouragements. I am very grateful for having opportunities to take classes and conduct collaborative research projects with them. These professors are always nice and supportive if I need their help.

Secondly, I would like to thank other excellent professors in Arizona State University (ASU), including Prof. Anthony Brazel, Prof. Larry Mays, Prof. Kamil Kaloush, Prof. Benjamin Ruddell, Prof. Matei Georgescu, Prof. Nancy Grimm, etc. In addition, I am grateful for all the supports from these helpful and friendly staff in ASU, including Ray Murdock, Stan Klonowski, Alicia Stiers, and Rose Petrini, etc. I also would like to thank Prof. Elie Bou-zeid from Princeton University, Prof. Winston Chow from National University of Singapore, and Dr. Ting Sun from University of Reading. Moreover, I am grateful for having a friendly and competitive study environment in ASU with the help and companion of friends including Jiachuan Yang, Chenghao Wang, Ruby Upreti, Tiantian Xiang, Adam Schreiner-McGraw, Nicole Pierini, Kristen Whitney,

Daniel Che and so on. Research sponsors are also greatly acknowledged, including National Science Foundation, Central Arizona-Phoenix Long-Term Ecological Research and U.S. Army Research Office.

Special thanks will go to Prof. Paul Linden and Prof. Alan Short from University of Cambridge who provide me with a precious opportunity to further pursue my academic dream as a postdoctoral researcher in the near future. In addition, I would like to thank Prof. Jun Xia (my previous supervisor of my Master's thesis) from Wuhan University in China for his continuous encouragement. Last but not least, strong spiritual support and encouragement from my parents and grandparents are highly appreciated.

TABLE OF CONTENTS

Page

Page

LIST OF TABLES

Table Page

LIST OF FIGURES

Figure Page

Figure Page

Figure Page

Figure Page

CHAPTER 1 INTRODUCTION

The world is undergoing rapid urbanization with the percentage of global population that live in urban areas increasing from 30% in 1950 to 47% in 2000, and projected to rise to 60% by 2030 (Collier, 2006; UN, 2012). Urban environment has some unique characteristics compared with natural environment, including large amounts of impervious artificial surfaces, the lack of vegetation cover, the presence of tall and dense building arrays, intensive human activities such as in industrial and/or transportation sectors. The rapid growth and the associated landscape modification of urban areas necessarily modify the surface energy and moisture balance by altering key physical and biophysical properties, with impacts on local and regional hydroclimate (Arnfield, 2003), leading to potential global climate responses via a cascade of land-atmosphere interactions (Niyogi et al., 2009). Urban land-use land-cover (LULC) changes, modified surface geometric and hydrothermal properties compounded by anthropogenic heat and moisture sources, contribute to numerous urban environmental features such as the urban heat island (UHI), air pollution, water pollution and urban flooding (Taha, 1997; Collier, 2006; Song et al., 2016c). To address these urban environmental issues, a better understanding on the urban land surface energy and water transport processes as well as urban land-atmosphere interactions is needed.

The last few decades have seen rapidly increasing research efforts in addressing urban environmental issues from different scales, including building scale, neighbourhood scale, regional scale, and global scale (Arnfield, 2003). At the building scale, building energy consumption for heating, cooling, ventilation, as well as the indoor and outdoor heat exchanges, can be resolved by commercial software such as EnergyPlus

(a cutting edge building energy simulation program developed by the US Department of Energy) (Sailor, 2008) or building energy models (BEM) (Kikegawa et al., 2003; Salamanca et al., 2010). At the neighbourhood scale, the urban microclimate can be simulated via two-dimensional (2-D) models such as an urban canopy model (UCM) (Masson, 2000; Kusaka et al., 2001; Martilli et al., 2002) or three-dimensional (3-D) models such as a computational fluid dynamics (CFD) model (Kim and Baik, 2004; Blocken, 2015). In UCMs, 2-D street canyon is the finest urban surface unit, which consists of roofs, walls and an infinite-long street between two facing walls (Kusaka et al., 2001). In CFD models, the urban surface is usually represented by 3-D building structure with resolution of 3-D air flow dynamics (Blocken, 2015).

A composition of microscale blocks in turn scale up to local scale (neighbourhoods) and ultimately mesoscale (the entire city) (Piringer et al., 2002; Arnfield, 2003). To assess the impacts of urban LULC changes on climate at a larger scale, land-atmosphere coupling has been utilized in regional climate models, such as the Weather Research and Forecasting (WRF) model (Skamarock et al., 2008; Trier et al., 2011; Chen et al., 2011; Georgescu et al., 2012, 2014) and general circulation models (e.g. Yang, 1995; Bonan et al., 2002). As spatial scales increase, the spatial variability will be reduced but modelling physics will be increased since different assemblages of processes need to be considered (Arnfield, 2003). Fundamental to the scale issue is the difference between the urban canopy layer (UCL) and the urban boundary layer (UBL), i.e. atmospheric boundary layer (ABL) over urban area (Arnfield, 2003). In the UCL (roughly from ground surface to roof level), the airflow and energy exchange processes are dominated by microscale and site-specific characteristics (Song and Wang, 2016a&b;

Song et al., 2016a). In the UBL (from ground surface to ~1000 m above the ground level), the atmospheric dynamics are affected by the presence of urban surface below and links local-scale and meso-scale phenomena (Arnfield, 2003). Therefore, a better understanding on the interactions between UCL and UBL is the key to assess the impact of urbanization on climate at different scales.

1.1 Urban land surface processes

Numerous urban surface models have been developed to incorporate urban features including the variety of surface morphology, abundance of impervious building materials, sparseness of vegetation, as well as emission of anthropogenic heat, water and pollutants (Grimmond et al., 2010). A common aim of all the urban surface models is to accurately predict surface energy budgets at the local scale (10^2-10^4 m) based on the fundamental principle of urban surface energy balance (Oke, 1988). Among all the urban surface models, a specific urban surface model should be selected for a specific application to balance the complexity of model physics and its computational requirements. In this dissertation, a 2-D rather than a 3-D urban canyon representation is adopted for the UCM. According to Grimmond et al. (2010), both 2-D and 3-D urban surface models can provide reasonable estimates of turbulent heat and moisture fluxes. But 3-D models are more complex than 2-D models by explicitly resolving the detailed momentum transfer and urban flow fields in canopies, which is more computationally costly and difficult to implement (Grimmond et al., 2009).

Broadly, there are two groups of UCMs, including the single-layer UCMs (SLUCM) (Masson, 2000; Kusaka et al., 2001; Wang et al., 2013) that focuses on the parametrization of the surface energy budget, and the more complex multilayer UCMs

(MLUCM) that also capture the momentum transport in urban canopies (Martilli et al., 2002; Dupont et al., 2004; Kondo et al., 2005). Both the SLUCM and MLUCM adopt the street canyon representation, consider active urban facets including road, wall, and roof, and focus on parametrization of surface energy budgets. A main difference between the two types of UCMs lies in the vertical structure of the street canyon. Specifically, the SLUCM resolves street canyon using a single vertical layer, whereas the MLUCM uses multiple layers in the vertical direction to represent the flow dynamics between different layers (Ryu et al., 2011; Kondo et al., 2005).

Most UCMs are capable of resolving the vertical transport of energy and predicting surface temperatures and sensible heat realistically, but are inadequate in representing the water transport due to the oversimplification of urban hydrological processes (Grimmond et al. 2010, 2011). To address this inadequacy, an improved SLUCM including an urban hydrologic model has been developed by Wang et al. (2013), which enables a more realistic representation of evapotranspiration, infiltration, irrigation, and soil moisture states in urban areas and improves the prediction of latent heat fluxes. Besides, the surface heterogeneity of each urban facet has also been considered in this new SLUCM. Specifically, each surface facet can have different material types, for example, ground surface can be a mixture of asphalt and grass, roof surface can be concrete pavement or vegetated, wall can be a combination of brick and glass. To parametrize the urban canopy dynamics more realistically, the representation of trees has been added in a SLUCM by Wang (2014) and a MLUCM by Krayenhoff et al. (2014). To resolve the new modeling challenges associated with the presence of trees such as the radiative shading, the Monte

Carlo method has been applied to trace the radiative exchanges in the street canyon with detailed parameterization schemes elaborated in section 4.1.2.

1.2 Atmospheric boundary-layer processes

1.2.1 Categories of atmospheric models

In this dissertation, the ABL (i.e. the lowest part of the troposphere) which extends from land surface to several kilometres (see Figure 1.1) is selected for analysis since it is directly influenced by the land surface and responds to surface forcing within an hour or less. The bottom 10% of the ABL is called the surface layer at both daytime and nighttime and is usually parameterized by Monin-Obukhov Similarity Theory (MOST). The upper 90% of the ABL at daytime is called convective mixed layer since the ABL is well-mixed due to buoyancy effect and strong turbulence. Above the convective mixed layer is the entrainment zone with above free air downward and overshooting thermals upward. On the other hand, the upper ABL at nighttime is called stable boundary layer due to negative buoyancy and less turbulence, with a residual layer and a capping inversion layer above.

There are plenty of ABL parameterization schemes, which can be categorized via two characteristics, including (1) the order of turbulence closure and (2) whether the mixing approach is local or non-local (Cohen et al., 2015).

To parameterize the ABL, the atmospheric variables within turbulence equations need to be decomposed into mean and perturbation components, representing the time-averaged conditions (background mean states) and turbulent fluctuations from the background mean state respectively. Equations pertaining to turbulence modeling always contain more unknown terms than known terms, resulting in the so-called “turbulence

closure" problem. To resolve this problem, the unknown term with higher-moment needs to be empirically related to lower-moment known terms. If the equations with only first moment are solved and the equations with second moment are empirically estimated, this method belongs to first-order closure technique such as in Medium-Range Forecast (MRF) model (Hong and Pan, 1996) and Yonsei University (YSU) model (Hong et al., 2006). If the equations with both first and second moment are solved while the equations with third moment are empirically estimated, this method is second-order closure technique such as in Mellor Yamada Nakanishi Nino 3.0 (MYNN3) model (Nakanishi and Niino, 2006). If not all of the prognostic equations for the second moments are solved, this method is called one-and-a-half order closure technique such as in Mellor-Yamada-Janjic (MYJ) model (Janjic, 1994) and Quasi Normal Scale Elimination (QNSE) model (Sukoriansky et al., 2005).

Another important difference between ABL models is whether it is local or non-local closure. Local closure assumes that turbulence is analogous to molecular diffusion, while non-local closure assumes that turbulence is a superposition of eddies (Stull, 1988). An unknown variable at any point in space is parameterized by known variables at this specific point in local closure models, but at numerous points of multiple vertical levels in non-local closure models (Cohen et al., 2015). Since vertical mixing throughout the ABL is primarily associated with large eddies that are rarely affected by local variations of static stability, local closure models cannot well represent the overall state of mixing in the ABL (Stensrud, 2009) although sometimes can be improved by incorporating higher orders of closure (Nakanishi and Niino, 2009). On the other hand, non-local closure models account for counter-gradient fluxes and represent deep ABL dynamics more

accurately than local closure models (Stull, 1991). According to Stull (1988), non-local methods have been used mostly with first-order closure. One of the most widely used non-local first order atmospheric models in numerical weather prediction is the YSU model based on non-local K-profile method (Troen and Mahrt, 1986; Noh et al., 2003; Hong et al., 2006). This model is well evaluated for different stability conditions, computationally inexpensive, and better in predicting convective boundary layer than local closure schemes (Pagowski, 2004; Dimitrova et al., 2014). Hereafter, the development history of first-order non-local K-profile method will be reviewed.

1.2.2 The first-order non-local *K*-profile method

The time evolution and spatial distribution of atmospheric variable in the ABL can be resolved by the following conservation equation (Troen and Mahrt, 1986; Stull, 1988):

$$\frac{\partial X}{\partial t} = -\frac{\partial}{\partial z}(\overline{w'X'}), \tag{1.1}$$

where X is a generic atmospheric state variable, which can be virtual potential temperature θ_v, specific humidity q, zonal wind u, meridional wind v, or carbon dioxide concentration c, etc., t denotes time evolution, z is the altitude above surface, w is the vertical wind speed, and $\overline{w'X'}$ is the vertical kinematic eddy flux, with the over-bar denoting the ensemble average.

Troen and Mahrt (1986) considers the non-local mixing atmospheric effect and parametrized the vertical flux in the convective boundary layer (CBL) as

$$-\overline{w'X'} = K\left(\frac{\partial X}{\partial z} - \gamma\right), \tag{1.2}$$

where K is the eddy diffusivity coefficient and γ is a correction term to local gradient by considering the non-local mixing due to large convective eddies. For virtual potential temperature (θ_v) and specific humidity (q), the eddy diffusivity coefficient ($K = K_h$) can be calculated from

$$K_h = P_r^{-1} K_m , \tag{1.3}$$

where P_r is the Prandtl number, K_m is the eddy viscosity, which can be parameterized by

$$K_m = k w_s z \left(1 - \frac{z}{z_h} \right)^2 . \tag{1.4}$$

Here, k is the von Karman constant (k =0.4), z is the distance from ground surface, z_h is the ABL height, w_s is the velocity scale at the top of surface layer (~10% ABL) and is parametrized by

$$w_s = u_* \phi_m^{-1} , \tag{1.5}$$

where u_* is the surface friction velocity and ϕ_m is the wind profile function according to similarity theory (Businger et al., 1971), as

$$\phi_m = \begin{cases} 1 + 4.7 z / L & \text{(stable)} \\ \left(1 - 16 z / L\right)^{-1/4} & \text{(unstable)} \end{cases} \tag{1.6}$$

with L denoting the Obukhov length.

Noh et al. (2003) modified Troen and Mahrt's governing equation, viz. Eqn. (1.2) by incorporating the heat flux contribution from the entrainment at the top of the ABL (when $z = z_h$) as

$$-\overline{w'X'} = K\left(\frac{\partial X}{\partial z} - \gamma\right) - \left(\overline{w'X'}\right)_{z_h}\left(\frac{z}{z_h}\right)^3, \tag{1.7}$$

and extending the atmospheric profiles above the ABL (when as $z > z_h$) as

$$-\overline{w'X'} = K\frac{\partial X}{\partial z}. \tag{1.8}$$

Hong et al. (2006) further improved the method of Noh et al. (2003) by taking the moisture effect into account in turbulent mixing. In addition, the parametrization of vertical eddy flux in the stable boundary layer (SBL) is added into the K-profile model with the exclusion of the non-local mixing term as in the CBL scheme (Hong, 2010). The main equations in the first-order non-local *K*-profile model are summarized in Table 1.1.

Table 1.1: Parameterization schemes for convective and stable boundary layers

variables	CBL	SBL
kinematic fluxes	$-\overline{w'x'} = K_x\left(\frac{\partial x}{\partial z} - \gamma_x\right) - \overline{\left(w'x'\right)}_{z_h}\left(\frac{z}{z_h}\right)^3$ (Hong, 2010)	$-\overline{w'x'} = K_x\frac{\partial x}{\partial z} - \overline{\left(w'x'\right)}_{z_h}\left(\frac{z}{z_h}\right)^3$ (Hong, 2010)
eddy diffusivity	$K_c = P_r^{-1}kw_m z\left(1-\frac{z}{z_h}\right)^2$ (Hong et al., 2006)	$K_c = kw_m z\left(1-\frac{z}{z_h}\right)^2$ (Hong, 2010)
velocity scale	$w_m = \left(u_*^3 + \frac{8kw_{*b}^3 z}{z_h}\right)^{1/3}$ (Hong et al., 2006)	$w_m = u_*$ (Hong, 2010)
ABL height	$z_h = \frac{Ri_{Bc}U^2}{\beta\Delta\theta_v}$ (Noh et al., 2003)	

Notes: z_h is the boundary-layer height, w the vertical velocity scale, u_* the friction velocity, $\gamma_{\theta v}$ the lapse rate in the free atmosphere, θ_v the virtual potential temperature, K_c the eddy diffusivity, γ the non-local mixing term, P_r the Prandtl number, k the von Karman constant, and subscripts '0', '*b*', '*s*', '*m*', '*h*', '*e*' denoting at the initial stage, corrected by incorporating moisture, on the surface, in the mixed-layer, at the boundary-layer top, and in the entrainment respectively, Ri_{BC} is the critical bulk Richardson number, U is the horizontal wind speed, $\beta = g/T_0$ is the buoyancy

parameter with g the acceleration due to gravity and T_0 the reference temperature, $\Delta\theta_v$ is the virtual potential temperature difference across the ABL.

1.3 Urban land-atmosphere interactions

Numerous studies on land-atmosphere coupling have been conducted using regional and global climate modeling frameworks (Chen and Avissar, 1994; Chen and Dudhia, 2001; Meehl and Tebaldi, 2004; Koster et al., 2004; Seneviratne et al., 2006; Fischer et al., 2007). It has been found that increased greenhouse gas concentrations could enhance the intensity and frequency of heatwaves (Meehl and Tebaldi, 2004; Seneviratne et al., 2006). In addition, soil moisture conditions of land surface have significant impacts on air temperature and precipitation patterns through land – atmosphere interactions (Eltahir et al., 1998; Koster et al., 2004; Fischer et al., 2007). For example, Fischer et al. (2007) reported that most of the recent European summer heat waves are closely related to the preceding dry soils resulting from a pronounced spring precipitation deficit. de Vrese et al. (2016) found that irrigation in South Asian could lead to increased precipitation in Eastern Africa, which could be attributed to increased moisture flux and advection effect.

Among these large-scale (regional or global) land-atmosphere coupling researches, the direct impacts of urban land surface changes on urban microclimate are underexplored since the spatial resolution in regional or global climate models is too big to incorporate detailed urban characteristics. In addition, recent urban environmental studies incorporating boundary-layer dynamics were mostly based on mesoscale weather prediction models such as the WRF model (Georgescu et al., 2014; Li et al., 2014; Sharma et al., 2016). While comprehensive physics of land-atmosphere interactions can

be captured by the fully-integrated mesoscale models, it is hard to disentangle the effect of individual dynamic modules (e.g. subsurface transport, plant biophysics, radiation parameterization, atmospheric schemes, etc.) and their relative contribution to the final signal in environmental changes. This is largely due to the uncertainty challenge in mesoscale modeling inherent in complex model structures, large parameter space, and coupling of multiple dynamic modules (Hargreaves, 2010). This leads to the outstanding challenge faced in this study that "How can the impact of urban landscape changes on the urban environment be singled out from that of the complexity of total environmental physics?"

To address this, a stand-alone scalable urban land-atmosphere coupling framework (see Figure 1.1) has been developed with detailed model physics described in Chapter 2. In this coupling framework, the urban land surface processes will be parameterized by the latest SLUCM including an improved urban hydrological module (Wang et al., 2011a, 2013; Sun et al., 2013a) while the urban boundary layer dynamics will be parameterized by a single column model (SCM), a modified version of the YSU boundary layer scheme based on a first-order non-local closure technique. The coupled SLUCM-SCM framework is tested to be capable of predicting the urban surface energy and water budgets with improved accuracy. Using the proposed model, a range of scenarios of urban LULC changes (such as changes of geometric and hydrothermal properties) can be simulated, and their impact on the boundary-layer growth and temperature/humidity distribution under both convective and stable conditions can be assessed. In Chapter 3, an advanced Monte Carlo method has been used to quantify the sensitivity of urban boundary layer dynamics to urban land surface characteristics based on the proposed

SLUCM-SCM framework. In Chapter 4, the impact of various forms of urban green infrastructure including trees, lawns, and green roofs on urban microclimate has been investigated. In addition, the implications of green infrastructure on urban air quality issues have been discussed. Lastly in Chapter 5, the main contributions of this dissertation have been summarized and some possible future works and challenges have been discussed.

It is noteworthy that in this study, the coupled model framework was mainly tested and applied in Phoenix, Arizona, a stereotypical semiarid city. In particular, the impacts of different urban heat mitigation strategies, such as the implementation of white (by increasing roof albedo) and green roofs (by adding vegetation cover on rooftops) on arid urban thermal environment have been assessed. According to United Nations (2011), semiarid and arid regions cover approximately 40% of the global land area and are home to two billion people, 90% of whom live in developing countries such as in Africa and Asia, which are prospected to experience the most rapid urbanization during the next few decades. Therefore, the proposed modeling framework and its applications can be further extended to cities in arid or semiarid regions worldwide, which is expected to have significant implications to urban planning and mitigation strategies for the sustainable development of cities in future generations.

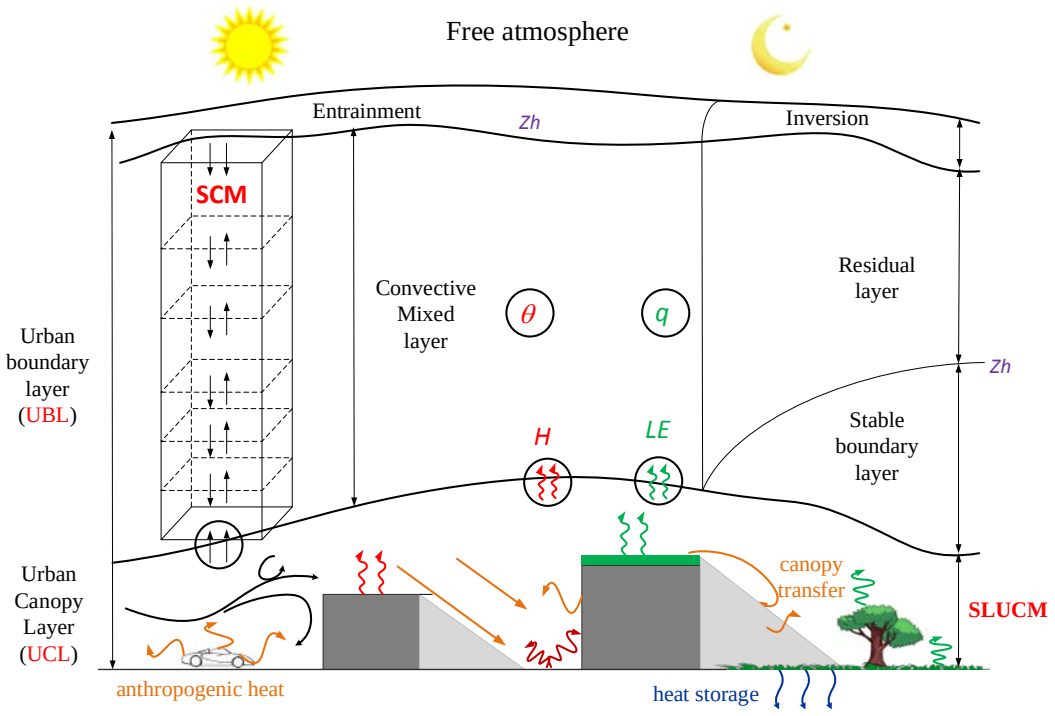

Figure 1.1: Schematic of urban land-atmosphere interactions (Here, *H* and *LE* denote the surface sensible and latent heat flux, θ and q denote atmospheric virtual potential temperature and specific humidity respectively, z_h denotes the ABL height.)

CHAPTER 2 MODEL DEVELOPMENT OF URBAN LAND-ATMOSPHERE COUPLING SYSTEM

In this chapter, a scalable coupled urban land-atmosphere modelling framework is proposed. The urban surface processes are parameterized via the latest SLUCM including an improved urban hydrological module (Wang et al., 2011a, 2013; Sun et al., 2013a). The urban atmospheric processes are parameterized by the SCM based on a first-order non-local closure technique. The model performances of the SLUCM, the SCM, and the coupled SLUCM-SCM are evaluated against field measurements (surface and ABL states) over multiple experimental fields. The coupled SLUCM-SCM framework is then applied to study the transport of heat and moisture in the integrated urban land-atmosphere system with different landscape characteristics, e.g. by changing urban geometry, surface albedo, vegetation fraction and aerodynamic roughness. The corresponding variation in ABL responses (primarily the evolution of ABL height as well as atmospheric temperature and humidity profiles in the ABL) helps to demonstrate the effectiveness of different urban planning strategies, particularly for UHI mitigation such as cool and green roofs.

2.1 Single-layer urban canopy model (SLUCM)

To capture the coupled transport and co-evolution of water and energy budgets in a built environment, here the latest SLUCM with a realistic urban hydrological model developed by Wang et al. (2011a, 2013) was adopted. The SLUCM employs the common single-layer street canyon representation for urban areas (Nunez and Oke, 1977; Masson, 2000; Kusaka, 2001) and takes into account the effect of urban green infrastructure (see Figure 2.1). Different urban facets experience time-varying exposures to sunlight and are

composed of different materials with different thermal and aerodynamic properties, thus resulting in different net shortwave and longwave radiative exchange within the urban canyon. The model explicitly resolves radiative trapping and shading effects inside the street canyon, taking into account the canyon orientation and the diurnal variation of solar azimuth angle. Besides, surface heterogeneity for each urban facet (i.e. roof, wall, and ground) is also included: e.g. the ground can consist of, but is not limited to, engineered (asphalt or concrete) pavements, vegetation or bare soil; similarly, wall materials can be brick or glass; roofs can be paved or vegetated. Furthermore, the urban hydrological module in the SLUCM is capable of predicting water transport over both natural and engineered surfaces, especially evapotranspiration from urban lawns and water retention on porous pavements. Forced by air temperature, humidity, pressure, wind speed and shortwave and longwave radiation fluxes, the SLUCM not only predicts the surface energy balance (i.e. net radiation, surface temperature and sensible and ground heat fluxes), but also hydrological processes (infiltration, evapotranspiration and irrigation) and sub-surface soil moisture states in urban areas.

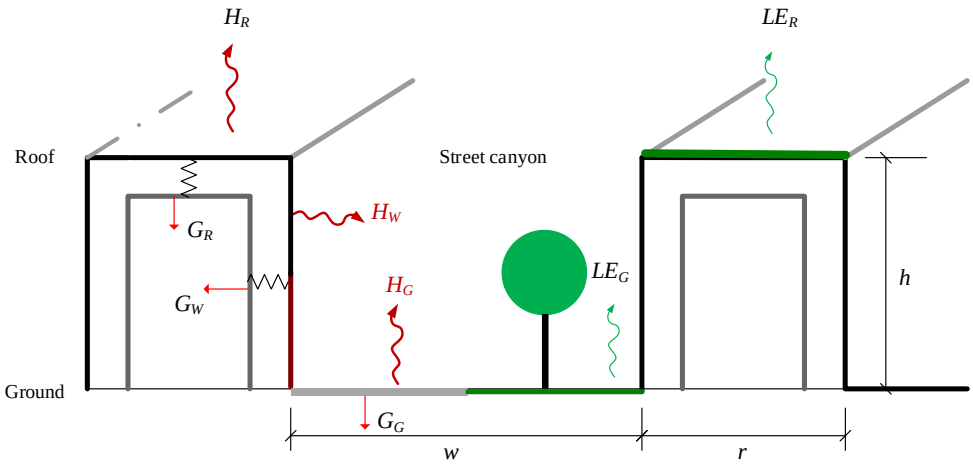

Figure 2.1: Schematic of surface energy partitioning in the advanced SLUCM.

Based on the assumption that the thermal energy involved in advection, radiative flux divergence, and canyon air temperature change is small in comparison with the energy stored in urban surfaces (Nunez and Oke, 1977), the energy balance in the SLUCM for the whole urban canopy layer is given by,

$$R_n + A_F = H_u + LE_u + G \tag{2.1}$$

where R_n is the net radiation, A_F is the anthropogenic heat and moisture fluxes, H and LE are the turbulent sensible and latent heat fluxes arising from the entire urban canopy layer with the subscript u denoting the urban canopy, and G is the conductive heat flux aggregated over all urban facets, taking into account the actual thickness and thermal mass of roofs, walls and ground.

The net radiation R_n for a generic urban facet (such as a roof) is calculated as

$$R_n = S^{\downarrow} + L^{\downarrow} - S^{\uparrow} - L^{\uparrow} \tag{2.2}$$

where $S^{\downarrow}$ and $L^{\downarrow}$ are the downwelling shortwave and longwave radiative fluxes respectively, $S^{\uparrow} = aS^{\downarrow}$ is the upwelling shortwave radiative flux with a the surface albedo, and $L^{\uparrow} = \varepsilon\sigma T_s^4$ is the upwelling longwave radiative flux, ε is the emissivity, σ is the Stefan-Boltzmann constant, and T_s is the surface temperature. The computation of net radiation inside a street canyon involves shading and radiative trapping effects, as detailed in Sect. 4.1.

The total turbulent fluxes H_u and LE_u from the urban area can be obtained as the areal averages of the fluxes from roof and canyon, viz.

$$H_u = r\sum_{k=1}^{N_R} f_{R,k} H_{R,k} + wH_{can}\,, \tag{2.3}$$

$$LE_u = r\sum_{k=1}^{N_R} f_{R,k} LE_{R,k} + wLE_{can}, \tag{2.4}$$

while the canyon turbulent fluxes are aggregated from all canyon sub-facets, i.e. walls and ground, viz.

$$H_{can} = \frac{2h}{w}\sum_{k=1}^{N_W} f_{W,k} H_{W,k} + \sum_{k=1}^{N_G} f_{G,k} H_{G,k} \tag{2.5}$$

$$LE_{can} = \frac{2h}{w}\sum_{k=1}^{N_W} f_{W,k} LE_{W,k} + \sum_{k=1}^{N_G} f_{G,k} LE_{G,k} \tag{2.6}$$

where subscripts *can*, *R*, *W*, *G* denote street canyon, roof, wall, and ground respectively, $r = R / (R + W)$, $h = B / (R + W)$ and $w = W / (R + W)$ are the normalized (dimensionless) roof width, building height and road width respectively, with *R*, *B* and *W* the corresponding physical dimensions, N_R, N_W and N_G are the number of sub-facet types of roof, wall and ground, and $f_{R,k}$, $f_{W,k}$, and $f_{G,k}$ are the areal fractions of each sub-facet.

Sensible heat fluxes in the SLUCM are parametrized as (Masson, 2000; Wang et al., 2013),

$$H = \frac{c_p \rho_a \left(T_s - T_a\right)}{r_a} \tag{2.7}$$

for all urban facets, and latent heat fluxes are calculated from

$$LE_{eng} = \begin{cases} 0, & \text{if } \delta_w = 0 \\ \dfrac{\rho_a L_v \left(q^*_{eng} - q_a\right)}{r_a}, & \text{if } \delta_w > 0 \end{cases} \tag{2.8}$$

for engineered surfaces, and

$$LE_{nat} = \begin{cases} \dfrac{L_v \rho_a \left(q^*_{veg} - q_a \right)}{r_a + r_s}, & \text{for vegetation} \\ \beta_e \dfrac{L_v \rho_a \left(q^*_{soil} - q_a \right)}{r_a}, & \text{for bare soil} \end{cases} \tag{2.9}$$

for natural surfaces, where ρ_a is the density of the air, c_p is the specific heat capacity of the air, T_a is air temperature, δ_w is the actual depth of water retention on the engineered surface, L_v is the latent heat of water vaporization, q_a is the specific humidity of the air, q^* is the saturated specific humidity, r_a is the aerodynamic resistance, r_s is the stomatal resistance, and β_e is a potential evaporation reduction factor.

The aerodynamic resistance between canyon facets (i.e. ground and wall) and air was formulated by Rowley et al. (1930) and Rowley and Eckley (1932) and parametrized as

$$r_a = \left(11.8 + 4.2 \sqrt{U_{can}^2 + W_{can}^2} \right)^{-1} \quad \text{for ground and wall}, \tag{2.10}$$

where U_{can} and W_{can} are the wind speed that along and perpendicular to canyon street. On the other hand, the aerodynamic resistance above the roof or canyon is computed using Monin-Obukhov similarity theory according to Mascart et al. (1995):

$$r_a = \begin{cases} \dfrac{C}{U_a a^2 \left(z_R \right) F_h \left(z_R \right)} & \text{above roof} \\ \dfrac{C}{\left(U_a - U_{can} \right) a^2 \left(z_R - z_T \right) F_h \left(z_R - z_T \right)} & \text{above canyon} \end{cases}, \tag{2.11}$$

where a^2 is the drag coefficient under neutral conditions, F_h is empirical functions of bulk Richardson number ($\mathrm{Ri_b}$), altitude (z), roughness length of momentum (z_{0m}) and heat (z_{0h}).

The stomatal resistance is parametrized based on a physiological approach (Noilhan and Planton, 1989; Niyogi and Raman, 1997):

$$r_s = r_{s,\min} F_{SR} F_W F_e F_T \,/\, \mathrm{LAI}\,, \tag{2.12}$$

where $r_{s,min}$ is the minimum stomatal resistance depending on the vegetation type ($r_{s,min}$ = 40 s m^{-1} for urban lawn); LAI is the leaf area index; and F is the adjusting factor with the subscripts *SR, W, e, T* relating to solar radiation, soil-water content, vapour pressure deficit and temperature respectively.

The factor β_e reflects the constraint on actual evaporation by soil water availability and can be parametrized as (Brutsaert 2005)

$$\beta_e = \frac{W - W_r}{W_s - W_r}\,, \tag{2.13}$$

where W is the volumetric soil water content, and W_s and W_r are the saturated and residual soil water content respectively. The actual soil water content can be computed by solving the Richards equation:

$$\frac{\partial W}{\partial t} = \frac{\partial}{\partial z}\left(D\frac{\partial W}{\partial z} + K + F_W \right), \tag{2.14}$$

where D and K are the hydraulic diffusivity and hydraulic conductivity for unsaturated soils respectively, estimated using van Genuchten (1980), and $F_W = P + Q_F - Ro - E_T$ is the water availability term with precipitation P, anthropogenic water Q_F, surface run-off Ro, and evapotranspiration E_T. Detailed parameterization of urban vegetation (mesic and xeric) is presented in Section 4.1.

In addition, the thermal fields in solid media, i.e. temperatures and soil heat fluxes, are computed by solving the heat conduction equation based on the Green's function

approach (Wang et al. 2011a), where thermal conductivity *k* and heat capacity *C* are needed. The anthropogenic heat and water budgets are ignored due to the lack of experimental data, but are recommended to be included whenever data are available.

2.2 Single column model (SCM)

The evolution of the boundary-layer height and spatial distributions of temperature and humidity in the UBL for both convective and stable conditions are parametrized in the SCM (a first-order non-local closure technique) (Hong et al., 2006) (see Figure 1.1). The SCM has a relatively simple representation of the UBL, but can capture the growth of the boundary layer with reasonable accuracy. Here the thermal field in the atmosphere is described using the virtual potential temperature θ_v, accounting for the effect of water vapour and pressure on boundary-layer stability (Ouwersloot and Vilà-Guerau de Arellano 2013). The virtual potential temperature (θ_v) for unsaturated air with mixing ratio *f* is defined as

$$\theta_v = \theta\left(1+0.61f\right), \tag{2.15}$$

where θ is the potential temperature and is defined as

$$\theta = T\left(\frac{p_0}{p}\right)^{0.286}, \tag{2.16}$$

with *T* denoting absolute air temperature, p_0 denoting the reference pressure (usually measured at the sea surface level), and *p* denoting air pressure at a certain altitude.

For the surface layer, mean profiles of the virtual potential temperature θ_v and the specific humidity *q* follow approximately logarithmic law distributions, based on Monin-Obukhov similarity theory (Businger et al. 1971; Stull 1988). In the UBL, mean profiles of θ_v and *q* are governed by the following diffusion equation (Troen and Mahrt 1986):

$$\frac{\partial X}{\partial t} = \frac{\partial}{\partial z}(-\overline{w'X'}), \tag{2.17}$$

where $X = \theta_v$ or q is a generic atmospheric state variable, t denotes time, z denotes altitude, w is the vertical wind speed, and $\overline{w'X'}$ is the vertical kinematic eddy flux with the over-bar denoting the ensemble average, subscripts "s" and "z_h" will be used to represent for the surface condition and boundary-layer top condition respectively in the subsequent context.

The heat and moisture fluxes in the convective (CBL) and stable (SBL) boundary layer can be parametrized as (Noh et al. 2003)

$$\overline{w'X'} = \begin{cases} -K_c\left(\frac{\partial X}{\partial z} - \gamma_c\right) + \overline{(w'X')}_{z_h}\left(\frac{z}{z_h}\right)^3 & \text{for CBL} \\ -K_c\frac{\partial X}{\partial z} + \overline{(w'X')}_{z_h}\left(\frac{z}{z_h}\right)^3 & \text{for SBL} \end{cases}. \tag{2.18}$$

Here, K_c is the eddy diffusivity coefficient, which is given by

$$K_c = \begin{cases} P_r^{-1} k w_s z\left(1 - \frac{z}{z_h}\right)^2 & \text{for CBL} \\ k w_s z\left(1 - \frac{z}{z_h}\right)^2 & \text{for SBL} \end{cases}, \tag{2.19}$$

where P_r is the Prandtl number, k is the von-Karman constant (=0.4), w_s is the velocity scale determined by

$$w_s = \begin{cases} \left(u_*^3 + \frac{8 k w_{*b}^3 z}{z_h}\right)^{1/3} & \text{for CBL} \\ u_* & \text{for SBL} \end{cases}, \tag{2.20}$$

γ_c is a non-local mixing term by incorporating the contribution of the large-scale eddies to the total flux and can be parametrized by (Troen and Mahrt 1986; Noh et al. 2003)

$$\gamma_c = C\frac{\left(\overline{w'X'}\right)_s}{w_s z_h}. \tag{2.21}$$

The kinematic heat and moisture fluxes at the lower boundary of the mixed layer (or equivalently, at the top of the surface layer) can be derived from H_u and LE_u, as predicted by the SLUCM:

$$\left(\overline{w'\theta'}\right)_s = \frac{H_u}{\rho_a c_p}, \tag{2.22}$$

$$\left(\overline{w'q'}\right)_s = \frac{LE_u}{\rho_a L_v}, \tag{2.23}$$

where the subscript *s* denotes the atmospheric surface layer. According to the definition of virtual potential temperature,

$$\left(\overline{w'\theta_v'}\right)_s = 0.61\bar{\theta}\left(\overline{w'q'}\right)_s + \left(1+0.61\bar{q}\right)\left(\overline{w'\theta'}\right)_s. \tag{2.24}$$

The turbulent fluxes at the top of the ABL for scalars θ_v and q are parametrized by

$$\left(\overline{w'\theta_v'}\right)_{z_h} = -0.15\left(\frac{\theta_v}{g}\right)w_m^3 / z_h, \tag{2.25}$$

$$\left(\overline{w'q'}\right)_{z_h} \approx 0. \tag{2.26}$$

A conventional method used to determine z_h involves a bulk Richardson number formulation based on the assumption that continuous turbulence vanishes beyond z_h (Troen and Mahrt 1986; Zilitinkevich and Baklanov 2002),

$$z_h = \frac{Ri_{Bc}U^2}{\beta\Delta\theta_v}, \tag{2.27}$$

where Ri_{Bc} is the critical bulk Richardson number, $\beta = g/T_0$ is the buoyancy parameter with g the acceleration due to gravity and T_0 the reference temperature, U is the horizontal wind speed at z_h, and $\Delta\theta_v = \theta_v(z_h) - \theta_s$ with θ_s calculated from

$$\theta_s = \theta_v(z_1) + \theta_T . \tag{2.28}$$

Here θ_T is the scaled potential temperature excess in the surface layer, given by

$$\theta_T = C\frac{\left(\overline{w'\theta'}\right)_s}{w_s}, \tag{2.29}$$

where C is a coefficient of proportionality (often set as 6.5 according to Troen and Mahrt 1986). The variable w_s is the velocity scale for the entire UBL, defined as

$$w_s = (u_*^3 + 7\varepsilon\kappa w_*^3)^{1/3}, \tag{2.30}$$

where u_* is the surface friction velocity, $\varepsilon = z_1/z_h \approx 0.1$ is the ratio of the surface-layer height to that of the UBL, κ is the von Karman constant, and w_* is the convective velocity scale given by

$$w_* = \left[\frac{g}{T_0}\left(\overline{w'\theta'}\right)_s z_h\right]^{1/3}. \tag{2.31}$$

Although the bulk Richardson number method outlined above is a widely used approach to estimate the boundary-layer height adopted by many numerical weather prediction models, the method is limited by the uncertainty associated with the selection of the Ri_{Bc} value that varies with surface roughness and flow history and has high spatial variability (Zilitinkevich and Baklanov 2002; Jeričević and Grisogono 2006), leading to numerical instability. In this chapter, a recently developed analytical solution to determine daytime z_h (Ouwersloot and Vilà-Guerau de Arellano 2013) and a classic

prognostic growth rate equation to determine nighttime z_h (Deardorff, 1971; Yu, 1977) were adopted. The daytime z_h is given by

$$z_h = \left\{ \begin{array}{l} z_{h0}^2 + \dfrac{(2+4w_e)}{\gamma_{\theta v}} \left[\Delta\theta_{v,0} z_{h0}^{\frac{1+w_e}{w_e}} - \left(\dfrac{w_e}{1+2w_e} \right) \gamma_{\theta v} z_{h0}^{\frac{1+2w_e}{w_e}} \right] \left(\hat{z}_h^{-\frac{1}{w_e}} - z_{h0}^{-\frac{1}{w_e}} \right) \\ + \left(\dfrac{2+4w_e}{\gamma_{\theta v}} \right) \int_{t_0}^{t} \left(\overline{w'\theta_v'} \right)_s dt \end{array} \right\}^{1/2}, \tag{2.32}$$

where z_{h0} is the initial CBL height, w_e is the entrainment rate at the inversion, $\gamma_{\theta v}$ is the lapse rate in the free atmosphere, $\Delta\theta_s$ is the potential temperature difference across the inversion, and $\hat{z}_h$ is a correction term given by

$$\hat{z}_h = \left[z_{h0}^2 + \left(\frac{2+4w_e}{\gamma_{\theta v}} \right) \int_{t_0}^{t} \left(\overline{w'\theta_v'} \right)_s dt \right]^{1/2}. \tag{2.33}$$

The nighttime z_h is calculated by

$$z_h(t) = z_h(t-1) + \frac{\partial z_h}{\partial t} \Delta t, \tag{2.34}$$

where the boundary layer height growth rate is given by

$$\frac{\partial z_h}{\partial t} = 0.025 u_* \left[1 - z_h / (0.35 u_* / f \right]. \tag{2.35}$$

Using the SCM schemes outlined above, the profiles of θ_v and q in the CBL or SBL can be estimated. Note that the residual layer above SBL keep similar pattern as CBL, therefore the profiles of θ_v and q are constant in the residual layer. However, it is more complex to parametrize the profiles of temperature and humidity above CBL. The following assumptions are used to obtain the spatial distributions of θ_v and q in the entrainment zone of CBL,

a) According to Deardorff et al. (1980), the thickness of the entrainment zone δ is estimated by

$$\frac{\delta}{z_h} = d_1 + \frac{d_2}{Ri_*}, \tag{2.36}$$

where $d_1 = 0.02$ and $d_2 = 0.05$ are empirical constants (Noh et al., 2003), and $Ri_* = (g/T_0) z_h \Delta\theta / w_*^2$ is the convective Richardson number.

b) The heat or moisture flux in the entrainment zone is proportional to the jump in θ_v or q at the inversion (Hong et al. 2006). Specifically

$$\Delta\theta_v|_{z_h} = \overline{(w'\theta_v')}_{z_h} / w_e, \tag{2.37}$$

$$\Delta q|_{z_h} = \overline{(w'q')}_{z_h} / w_e. \tag{2.38}$$

The entrainment rate w_e is typically in the range 0.01 to 0.20 m s^{-1} (Stull, 1988).

c) The lapse rates $\gamma_{\theta v}$ and γ_q are considered to be constant in the free troposphere above the CBL (Kim et al., 2006; Ouwersloot and Vilà-Guerau de Arellano, 2013).

Based on the above assumptions, the profiles of θ_v and q in the entrainment zone and the free atmosphere can be estimated as

$$\theta_v = \begin{cases} \theta_{vm} + \dfrac{\Delta\theta_v}{\delta}(z - z_h), & z_h < z < (z_h + \delta) \\ \theta_{vm} + \Delta\theta_v + \gamma_{\theta v}\left[z - (z_h + \delta)\right], & z > (z_h + \delta) \end{cases}, \tag{2.39}$$

$$q = \begin{cases} q_m + \dfrac{\Delta q}{\delta}(z - z_h), & z_h < z < (z_h + \delta) \\ q_m + \Delta q + \gamma_q\left[z - (z_h + \delta)\right], & z > (z_h + \delta) \end{cases}, \tag{2.40}$$

where θ_m and q_m are the virtual potential temperature and specific humidity at the top of the mixed layer (Kim et al., 2006).

To better clarify the parameterization of atmospheric profiles of θ_v and q, a sketch of typical atmospheric profiles under both convective and stable conditions is presented in Figure 2.2. Note that in general q profile is similar under both convective and stable conditions, therefore only one profile under convective condition is presented in Figure 2.2 (a).

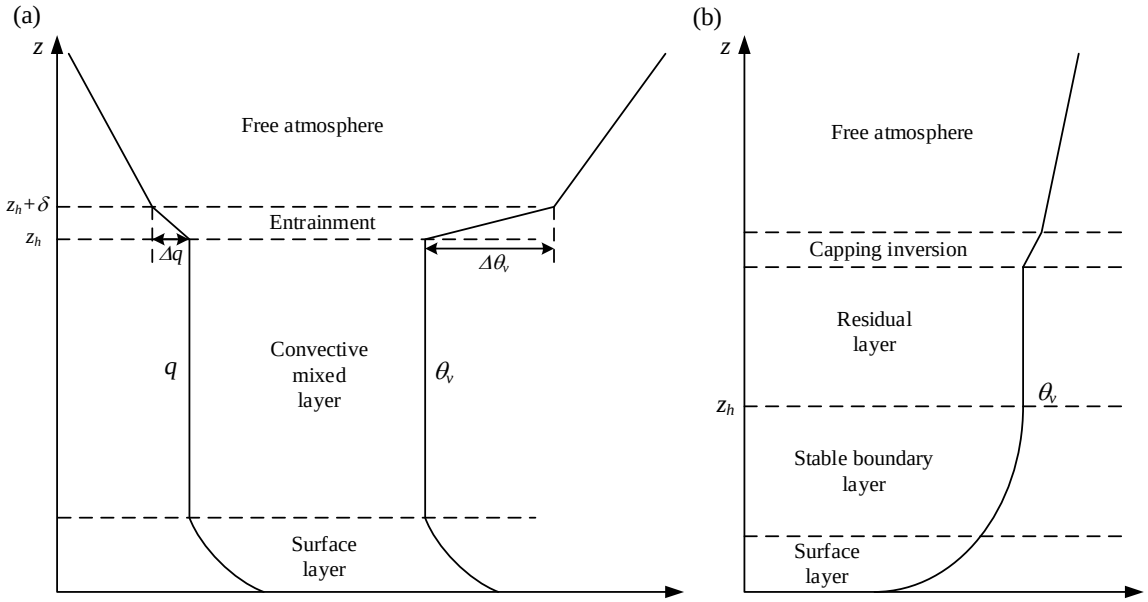

Figure 2.2: Sketch of typical atmospheric profiles of θ_v and q within (a) convective and (b) stable boundary layer.

In summary, the main vertical exchanges between the SLUCM and SCM are the heat and moisture fluxes from UCL to UBL (as seen in Figure 1.1). The surface turbulent sensible (H_u) and latent heat (LE_u) flux calculated by the SLUCM needs to be converted and linearly interpolated to kinematic eddy heat ($\overline{w'\theta_v'}$) and moisture ($\overline{w'q'}$) flux via Eqns. (2.22)-(2.24). With these kinematic eddy heat and moisture fluxes arising from urban surface as lower boundary condition and prescribed / measured initial boundary layer condition (i.e. initial boundary layer height and profiles of temperature and

humidity), the SCM can simulate the time evolution of ABL height as well as temperature and humidity values at different vertical levels in the ABL (the ABL depth at each time step is discretized to six levels). Note that this integrated SLUCM-SCM framework only permits one-way (i.e. bottom-up) coupling in the vertical direction at its present setting.

2.3 Model evaluation

2.3.1 Evaluation of the SLUCM

Model predictions by the SLUCM are compared against field measurements from two eddy-covariance (EC) towers located at Phoenix, Arizona and Princeton, New Jersey, USA. Site information of the two EC towers is described in Table 2.1 (see Chow et al., 2014; Sun et al., 2013b; Ramamurthy et al., 2014 for more details). Meteorological forcing data used to test the SLUCM were collected from June 12-17, 2012 (all clear days) during a pre-monsoon season at Phoenix, and from May 4-9, 2010 for Princeton covering a variety of weather conditions. Results of the comparison between model predictions and field measurements are shown in Figure 2.3, which includes net radiation, sensible heat and latent heat fluxes. Note that the first day in each dataset is selected for model calibration and the remaining days are for model validation. The calibrated model input parameters for Phoenix site are presented in Table 2.2, the calibrated model input parameters for Princeton site can be found in Wang *et al*. (2013). The root-mean-square errors (*RMSE*) for R_n, H_u, LE_u are 20, 34, 20 W m^{-2} respectively for the Phoenix site, and 16, 37, 18 W m^{-2} respectively for the Princeton site. It is clear that the SLUCM is capable of predicting the surface energy budget with reasonable accuracy. The realistic representation of land-surface processes by the SLUCM, especially turbulent sensible and

latent heat fluxes arising from urban canopies, then provide reliable boundary conditions to the overlying CBL.

Table 2.1: Geographic information of the two sites at Phoenix, Arizona and Princeton, New Jersey, USA

Experiment site	Phoenix	Princeton
Location	33.48 ^{o}N 112.14 ^{o}W	40.35 ^{o}N 74.65 ^{o}W
Measurement height (m)	22.1	23.2
Building height (m)	3.5	18.9
Land-use types	Residential	Suburban

(a)

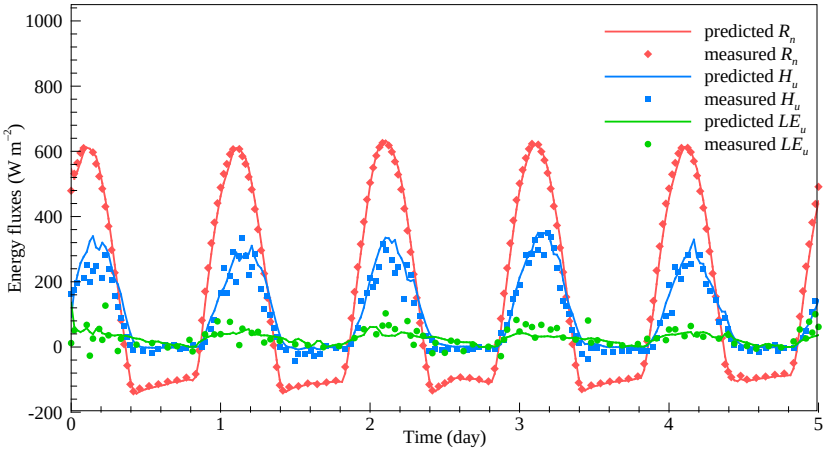

(b)

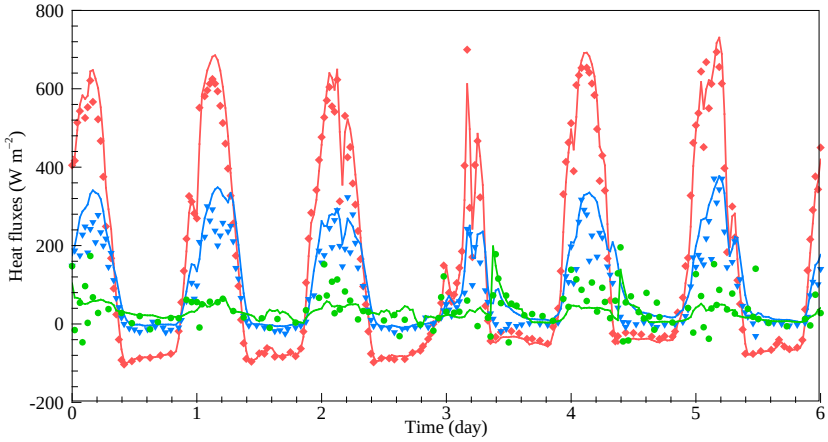

Figure 2.3: Comparison of predicted sensible heat, latent heat and net radiative fluxes by the SLUCM and field measurements at (a) Phoenix, Arizona from June 12 to June 17, 2012, and (b) Princeton, New Jersey from May 4 to May 9, 2010.

2.3.2 Evaluation of the SCM

To assess the SCM performance, two sets of atmospheric profiling data are used, including, (1) measurements for March 26 2005, at the Point Reyes site (38° 5' 27.6" N, 122° 57' 25.80" W) in California, USA based on a balloon-borne sounding system (SONDE) (Atmospheric Radiation Measurement Program, 2011), and (2) Day 33 data (August 17 1967) from the Wangara experiment at Hay, New South Wales (34° 30' S, 144° 56' E) (Clarke et al., 1971). Weather conditions during the measurements at both sites were highly convective, cloudless and free of synoptic frontal influences.

For the Point Reyes site, the surface sensible and latent heat fluxes and atmospheric temperature and humidity profiles were measured at 0930 PST (local time) on March 26 2005. The SCM is initialized with neutral virtual potential temperature and humidity profiles at the time when the CBL starts to develop (early morning). The initial values of temperature and humidity in the CBL are set to be the same as values at the top of the surface layer. Driven by the surface sensible and latent heat fluxes, the SCM determines corresponding atmospheric temperature and humidity profiles. Comparisons between predicted and measured vertical distributions of temperature and humidity in the mixed layer are in Figure 2.4a&b. The *RMSE* values are 0.15 K for mean θ_v and 1.07×10^{-4} kg kg^{-1} for mean q in the mixed layer.

At the Wangara site, there were no direct measurements of surface sensible and latent heat fluxes. To drive the SCM, a simple "slab" model, reduced from the SLUCM without the presence of street canyons, was used to calculate these heat fluxes with the measured surface meteorological forcing, including net radiation, ground heat flux, near-surface air temperature/humidity, atmospheric pressure and wind speed. Figure 2.4c&d

shows comparisons of the SCM predictions and measurements of θ_v and q at 1200 and 1500 AEST (local time). The *RMSE* values are 0.55 K and 0.48 K of mean θ_v in the mixed layer, and 1.02×10^{-4} kg kg^{-1} and 9.23×10^{-5} kg kg^{-1} at 1200 and 1500 AEST respectively.

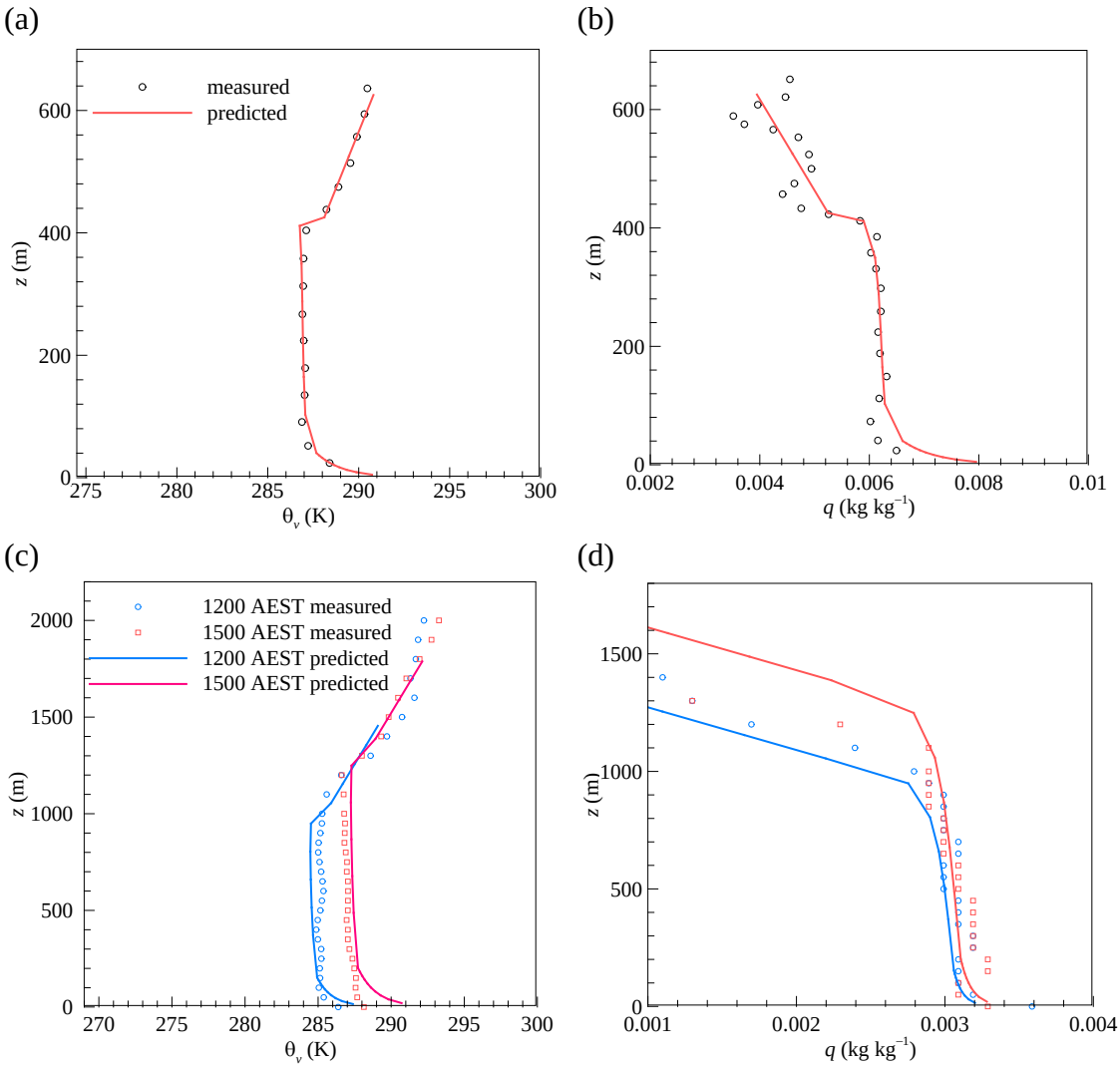

Figure 2.4: Comparison of the SCM predictions and field measurements of (a) virtual potential temperature and (b) specific humidity at 0930 PST on March 26, 2005 in Point Reyes site, California, USA, and (c) virtual potential temperature and (d) specific humidity at 1200 and 1500 AEST on Day 33 of the Wangara experiment in New South Wales, AUS.

2.3.3 Evaluation of the coupled SLUCM-SCM

To evaluate the coupled SLUCM-SCM framework outlined in Section 2.1, experiment data of temperature and humidity profiles were obtained from NOAA/ESRL radiosonde database (http://esrl.noaa.gov/raobs/) for two typical convective days, i.e. July 2nd, 2013 and July 9th, 2013 at Phoenix site (33.45 N, 111.95 W), Arizona. All atmospheric data in the ESRL Radiosonde database were subjected to gross error and hydrostatic consistency checks according to Schwartz and Govett (1992). The coupled modeling framework was driven by surface meteorological variables measured by a network of wireless meteorological stations (33.44 N, 111.92 W) (see Song and Wang, 2015b for details). The comparison of the simulated and observed profiles of virtual potential temperature and specific humidity is shown in Figure 2.5 for the two days at 16:44 pm and 16:37 pm (local time), respectively. Major difference between the observed and modeled profiles occurs in the surface layer. This is mainly due to that the SCM in the modelling framework uses Monin-Obukhov similarity theory (MOST) for parameterizing the surface layer profiles. MOST assumes homogeneity of turbulence and surface conditions, which is rarely satisfied for the ABL over a built terrain.

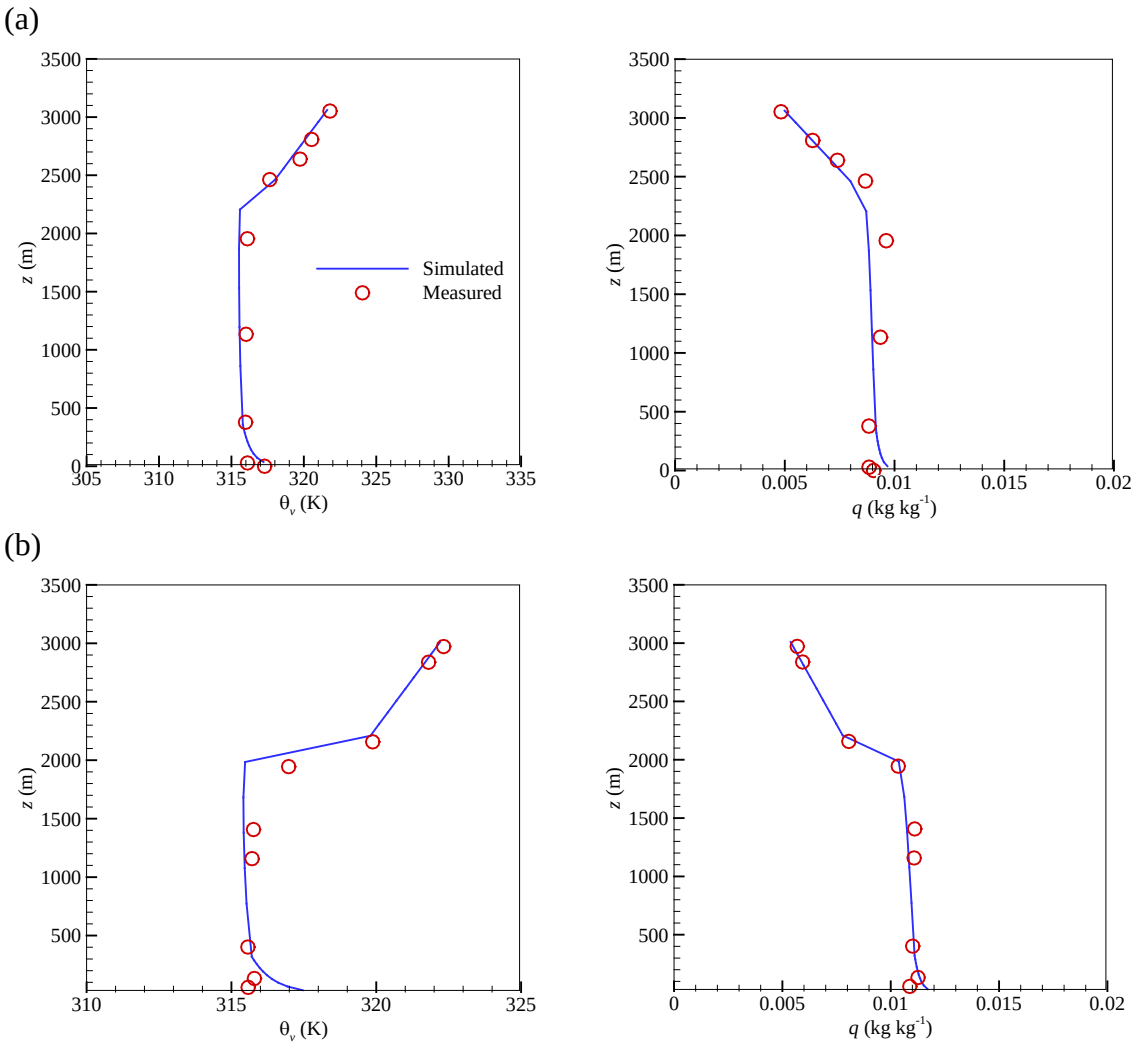

Figure 2.5: Comparison of simulated and measured atmospheric profiles of virtual potential temperature θ_v and specific humidity q for two time points, i.e. (a) 16:44 (local time) on July 2nd, 2013, and (b) 16:37 (local time) on July 9th, 2013 at NOAA-ESRL Phoenix site.

2.4 Case study of the coupled SLUCM-SCM

In this section, four cases are designed to assess the impact of urban LULC changes on the atmosphere using the coupled SLUCM-SCM framework, by changing (1) street canyon aspect ratio, (2) roof albedo, (3) roof vegetation fraction, and (4) aerodynamic roughness length. Given that the SLUCM predictions are more sensitive to roof properties (Loridan et al., 2010; Wang et al., 2011b), we focus more on the effect of

roof characteristics than that of the street canyon. The coupled model is driven by meteorological forcing (air temperature, pressure, humidity, wind speed, and downwelling radiation) for a sunny day (June 13, 2012) in Phoenix, Arizona, with sunrise at 0518 MST (local time) and sunset at 1939 MST. The list of input parameters required by the coupled SLUCM-SCM for a baseline scenario which reproduces the real condition at study site is presented Table 2.2. Surface temperatures for different urban canyon facets (roof, wall, and ground) were initialized based on the availability of field measurements from weather stations. In the subsequent context of case studies, all the input parameters are kept as constant as in the baseline scenario (Table 2.2), unless otherwise specified.

Table 2.2: List of input parameters for the coupled SLUCM-SCM framework

Variable	Symbol	Value
Surface dimensional parameters		
Roof level (building height) (m)	z_R	3.5
Reference height of atmospheric measurements (m)	z_a	21.95
Normalized building height	h	0.10
Normalized roof width	r	0.45
Normalized road width	w	0.55
Roughness length for momentum above roof (m)	$z_{m,R}$	0.01
Roughness length for heat above roof (m)	$z_{h,R}$	0.002
Roughness length for momentum above canyon (m)	$z_{m,can}$	0.01
Roughness length for heat above canyon (m)	$z_{h,can}$	0.002
Surface thermal parameters		
Albedo of conventional (paved) roof	$a_{R,c}$	0.10
Albedo of vegetated roof (green-roof)	$a_{R,v}$	0.15
Albedo of wall	a_W	0.25
Albedo of ground	a_G	0.15
Emissivity of conventional roof	$\varepsilon_{R,c}$	0.95
Emissivity of vegetated roof	$\varepsilon_{R,v}$	0.93
Emissivity of wall	ε_W	0.95
Emissivity of ground	ε_G	0.95
Thermal conductivity of conventional roof (W m^{-1} K^{-1})	$k_{R,c}$	0.6
Thermal conductivity of vegetated roof (W m^{-1} K^{-1})	$k_{R,v}$	1.0
Thermal conductivity of wall (W m^{-1} K^{-1})	k_W	1.3
Thermal conductivity of ground (W m^{-1} K^{-1})	k_G	1.2
Heat capacity of conventional roof (J m^{-3} K^{-1})	$C_{R,c}$	1.9×10^{6}
Heat capacity of vegetated roof (J m^{-3} K^{-1})	$C_{R,v}$	2.1×10^{6}
Heat capacity of wall (J m^{-3} K^{-1})	C_W	1.5×10^{6}
Heat capacity of ground (J m^{-3} K^{-1})	C_G	1.1×10^{6}
Surface hydrological parameters		
Saturated soil water content (soil porosity)	W_s	0.48
Residual soil water content	W_r	0.15
Saturated hydraulic conductivity (m s^{-1})	K_s	3.38×10^{-6}
Atmospheric parameters		
Entrainment rate at the inversion (m s^{-1})	w_e	0.2
Lapse rate of virtual potential temperature in free atmosphere (K m^{-1})	$\gamma_{\theta v}$	0.006

2.4.1 Effects of canyon-aspect ratio

The canyon-aspect ratio, defined as h/w, is a primary indicator of urban morphology in the SLUCM, and has a significant impact on the partitioning of radiative heat inside a street canyon (Theeuwes et al., 2014). Detailed formulation of the shortwave and longwave radiation in a street canyon, as functions of the canyon dimension, is presented in Appendix A. Increasing h/w values implies that the morphology of a built environment changes from sparse to dense building arrays or from shallow to deep street canyons. The variation of CBL height corresponding to h/w = 0.25, 2, and 8 is shown in Figure 2.6(a), where transition occurs at about 10.5 h after the formation of the CBL. According to Eq. 23, the evolution of CBL height is strongly related to the surface sensible heat flux as shown in Figure 2.7, where a non-linear relation is found between H_s and h/w, i.e. larger h/w values lead to larger H_s in early morning and late afternoon but smaller H_s in the middle of the day. The main contributor to this non-linear effect could be the evolution of surface temperatures and heat fluxes inside the street canyon, governed by two counteracting processes, viz. the shading effect of the direct shortwave radiation and the trapping effect of diffuse shortwave radiation and longwave radiation. Schematics of the shading and trapping effects for urban canyons with different building aspect ratios are presented in Figure 2.8.

To elaborate on the governing mechanisms, Figure 2.9 conceptually illustrates the relationship between the change in canyon surface temperature ΔT_{can}, averaged over walls and ground, and building-aspect ratios and zenith angles. First, with the same magnitude of incoming solar radiation, canyon-aspect ratio is a significant factor in dictating ΔT_{can}. Canyons with larger h/w, i.e. taller buildings or narrower streets, tend to

be warmer since more heat is trapped due to more reflections between canyon facets (trapping effect). In contrast, canyons with larger h/w are cooler because of a larger shaded area (shading effect). The combined effect due to h/w leads to a maximum ΔT_{can} in the moderate h/w range, as shown in Figure 2.9(a) (Theeuwes et al., 2014). Secondly, the zenith angle of incoming solar radiation is also important for radiative trapping and shading effects. The zenith angle is directly related to (i) the number of reflections experienced by a radiative ray inside the street canyon, and (ii) the magnitude of the incoming solar radiation depending on the time of the day. If zenith angle is close to 90 degrees, i.e. early morning or late afternoon, the trapping effect is significant due to multiple radiative reflections between canyon facets, while the shading effect is small due to low incoming solar radiation. In contrast, the street canyon exhibits a smaller trapping effect and a larger shading effect around noon when the zenith angle is close to zero. The resultant effect on ΔT_{can} as a function of the zenith angle (or time of the day) for a certain h/w is shown in Figure 2.9(b). Overall, interactions between radiative trapping and shading effects lead to the non-linear effect of h/w on the sensible heat flux arising from the urban canopy during daytime (Figure 2.7), which is then manifested in the diurnal evolution of the CBL height (Figure 2.6a).

The effect of h/w on the spatial distribution of θ_v in the mixed layer is presented in Figure 2.10. To illustrate the temporal variation of the θ_v profiles, six time points were selected for comparison, viz. early morning (0700 MST), late morning (1000 MST), noon (1200 MST), early afternoon (1400 MST), late afternoon (1600 MST) and dusk (1900 MST). In the morning, when the trapping effect is dominant, the canyon with $h/w = 8$ exhibits largest θ_v, while the differences among h/w cases decrease with time. This can be

interpreted as the trapping effect diminishes and the shading effect becomes dominant due to the change of zenith angle. This trend continues in the afternoon till the excess temperature arising from dense urban areas (large h/w) is completely offset by the shading effect. Eventually, close to dusk, the trapping effect overtakes the shading effect again when the solar angle of incidence decreases. But the combined effect of complex radiative interactions results in the street canyon with moderate h/w = 2 has the highest θ_v in the mixed layer at 1900 MST, consistent with the speculation illustrated in Figure 2.9(a).

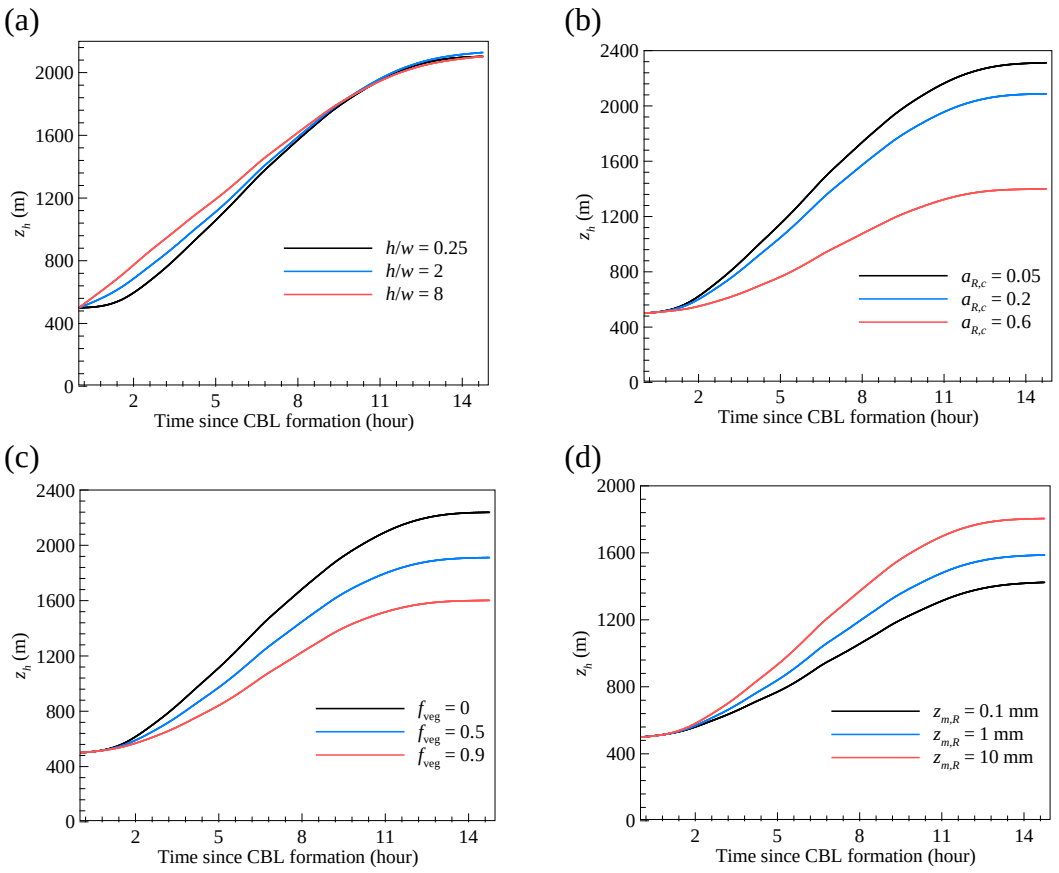

Figure 2.6: Time evolution of the ABL height z_h with different land-surface characteristics: (a) aspect ratio h/w = 0.25, 2 and 8; (b) roof albedo $a_{R,c}$ = 0.05, 0.2 and 0.6; (c) roof vegetation fraction f_{veg} = 0, 0.5 and 0.9; and (d) roof aerodynamic roughness $z_{m,R}$ = 0.1, 1 and 10 mm.

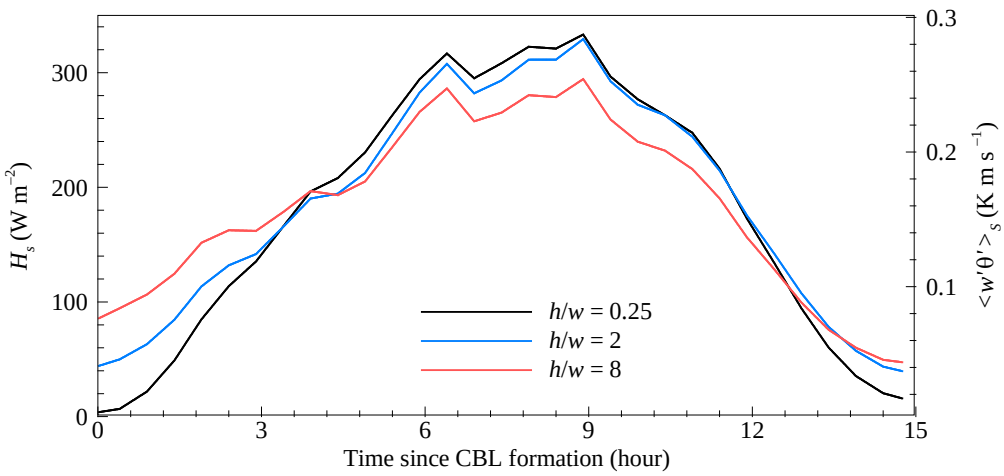

Figure 2.7: Time evolution of sensible heat in the surface layer H_s for canyon aspect ratio h/w = 0.25, 2 and 8, respectively. The corresponding kinematic heat flux $\left(\overline{w'\theta'}\right)_s$ values are also indicated on the right (the bracket notation is used instead of overhead bar for ensemble mean on the axis).

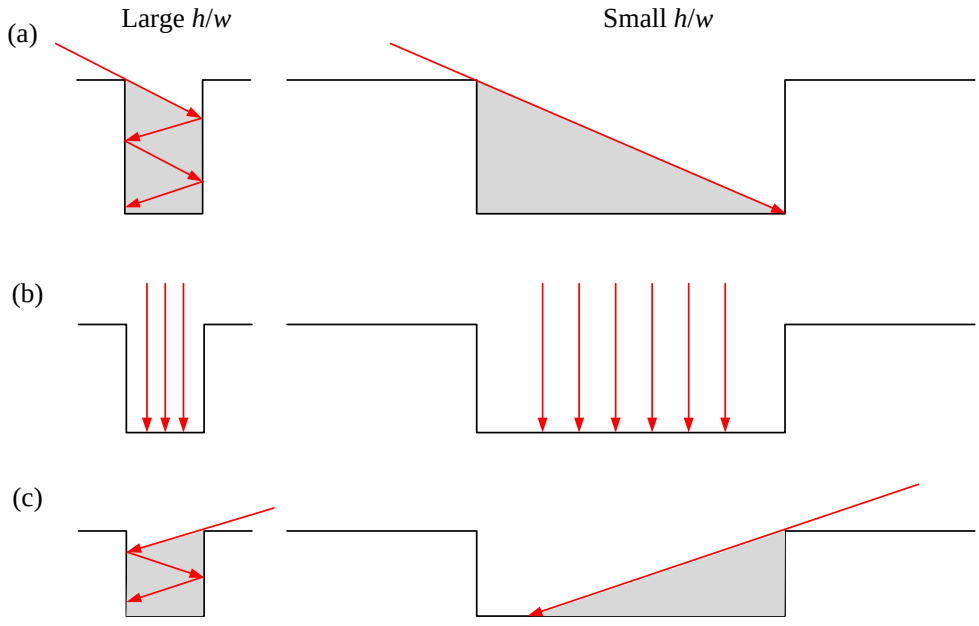

Figure 2.8: Illustration of radiative trapping and shading effects in street canyons with different aspect ratios, at different time of the day: (a) early morning, (b) noon and (c) late afternoon, with various angles of incidence of solar radiation. Note that the sketched canyon dimensions are not to scale and do not present the actual street canyons.

(a)

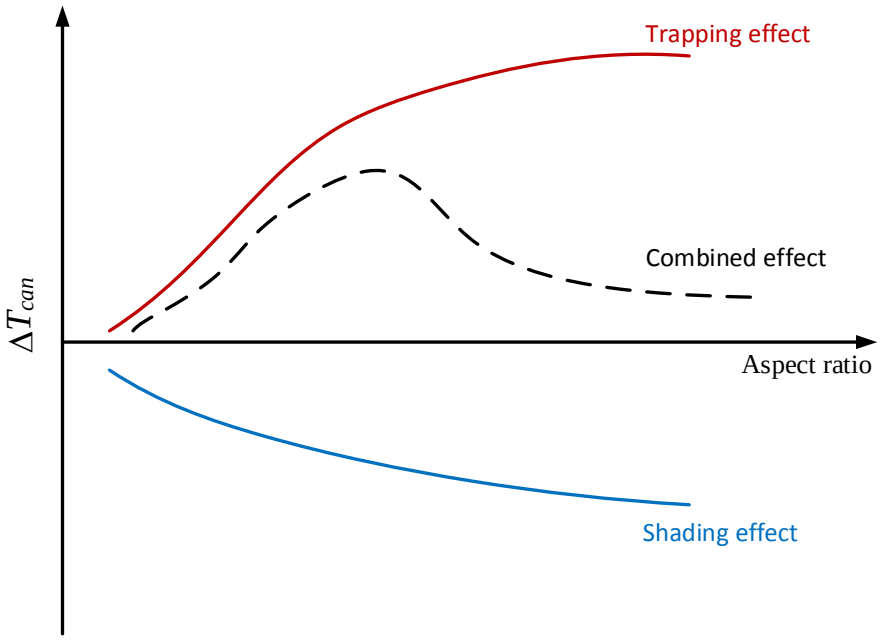

(b)

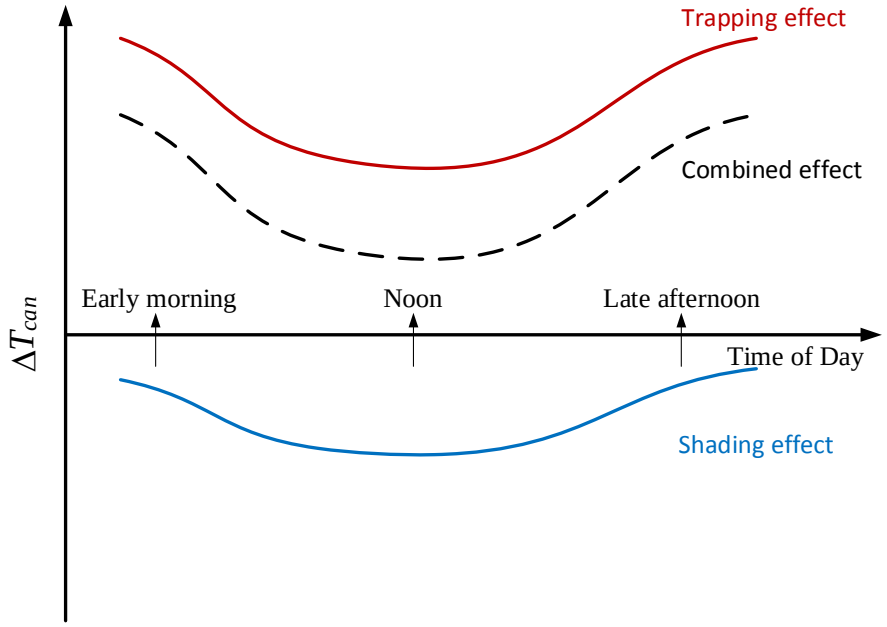

Figure 2.9: Conceptual sketches of the effects of radiative trapping and shading on changes of averaged canyon surface temperatures (ΔT_{can}) as a function of (a) aspect ratio and (b) time of day.

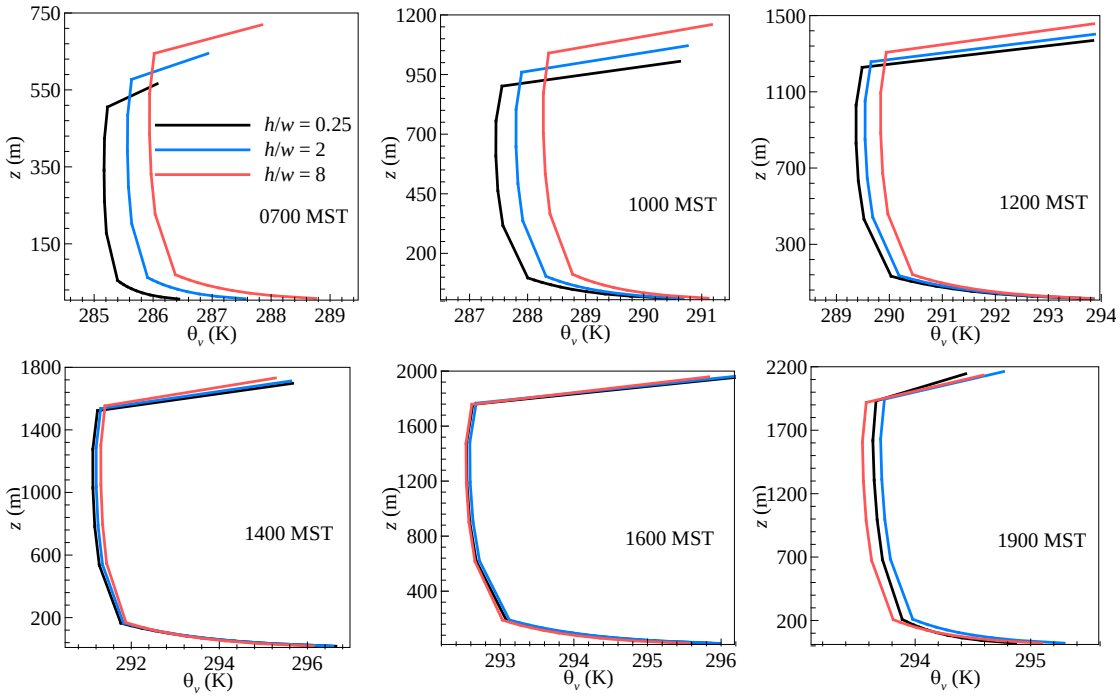

Figure 2.10: Model predictions of virtual potential temperature profiles in the ABL at 0700, 1000, 1200, 1400, 1600 and 1900 MST for canyon aspect ratios h/w = 0.25, 2 and 8.

2.4.2 Effects of roof albedo

Roofs with high albedo (customarily referred to as “cool roofs” in building communities) have attracted extensive interest as a popular strategy to mitigate the canopy UHI (Akbari et al. 2012; Jacobson and Ten Hoeve 2012). However, the impact of surface albedo on the ABL over an urban area is less frequently discussed. Here three cases with different albedos of conventional (paved) roofs, viz. $a_{R,c}$ = 0.05, 0.2 and 0.6, were simulated to investigate the effect of cool roofs on the CBL temperature. Physically, higher albedo leads to lower roof surface temperature, which reduces sensible heat fluxes above the roof and the urban surface and reduces the CBL height in turn, as shown in Figure 2.6(b). In Figure 2.11, it is clear that higher $a_{R,c}$ values also result in lower θ_v in the mixed layer. Note that the simulation results in this case are based on meteorological

conditions for a clear day in a desert city without clouds and aerosols in the ABL. In the presence of clouds and aerosols, the transport of shortwave and longwave radiation in the ABL, atmospheric stability and the land-surface energy partitioning are all modified (Stull 1988). Such complexities are not incorporated in the current numerical framework.

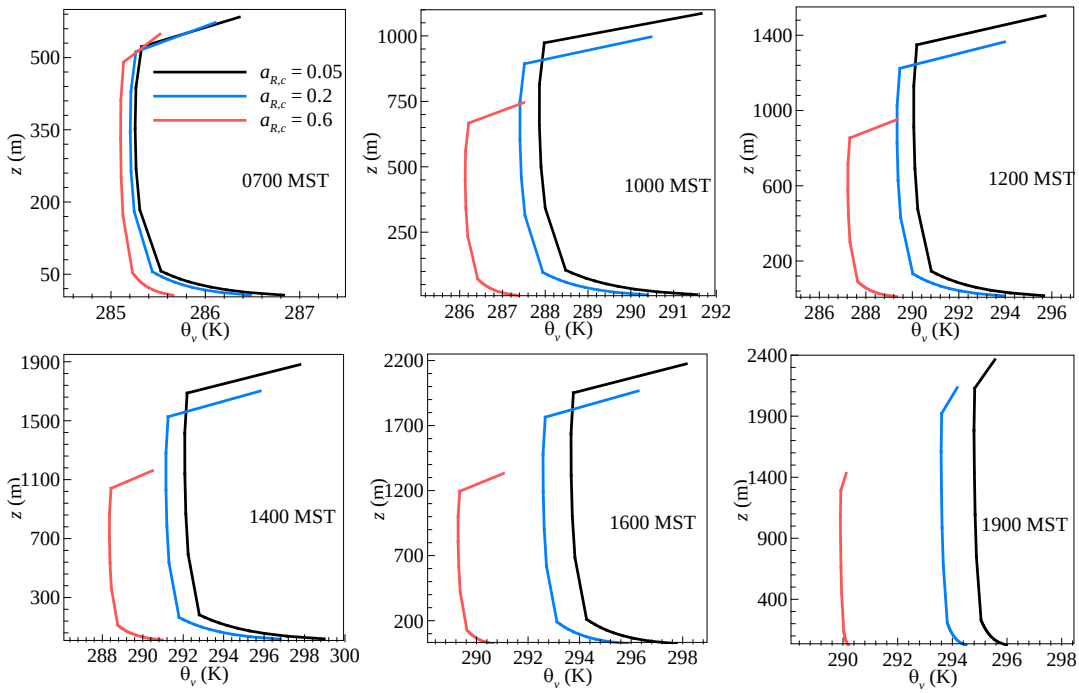

Figure 2.11: Model predictions of virtual potential temperature profiles in the ABL at 0700, 1000, 1200, 1400, 1600 and 1900 MST for roof albedo $a_{R,c}$ = 0.05, 0.2 and 0.6.

2.4.3 Effects of vegetation fraction

"Green" urban infrastructures, e.g. green roofs, urban lawns, urban agriculture, etc., are gaining increasing popularity as an effective means of reducing adverse urban environmental effects such as UHI mitigation, stormwater management and the preservation of ecological diversity (Dvorak and Volder, 2010; Sailor et al., 2012; Sun et al., 2013a). Previous studies using the SLUCM have found that the vegetation fraction in built environments is critical in determining the vertical transport of heat and moisture within urban canopies (Wang et al., 2011b; Yang and Wang, 2014). Using the coupled

SLUCM-SCM framework, three vegetated roof fractions f_{veg} = 0, 0.5, 0.9 were chosen to investigate the effect of green roofs on the CBL. The growth of ABL height is presented in Figure 2.6(c), while the distributions of θ_v and q in the mixed layer are shown in Figure 2.12 and Figure 2.13, for different f_{veg}. In general, larger f_{veg} values lead to greater latent heat and smaller sensible heat fluxes. Consequently, an increase in green roof fraction in urban canopies results in a significant cooling effect, which can effectively "penetrate" throughout the entire CBL.

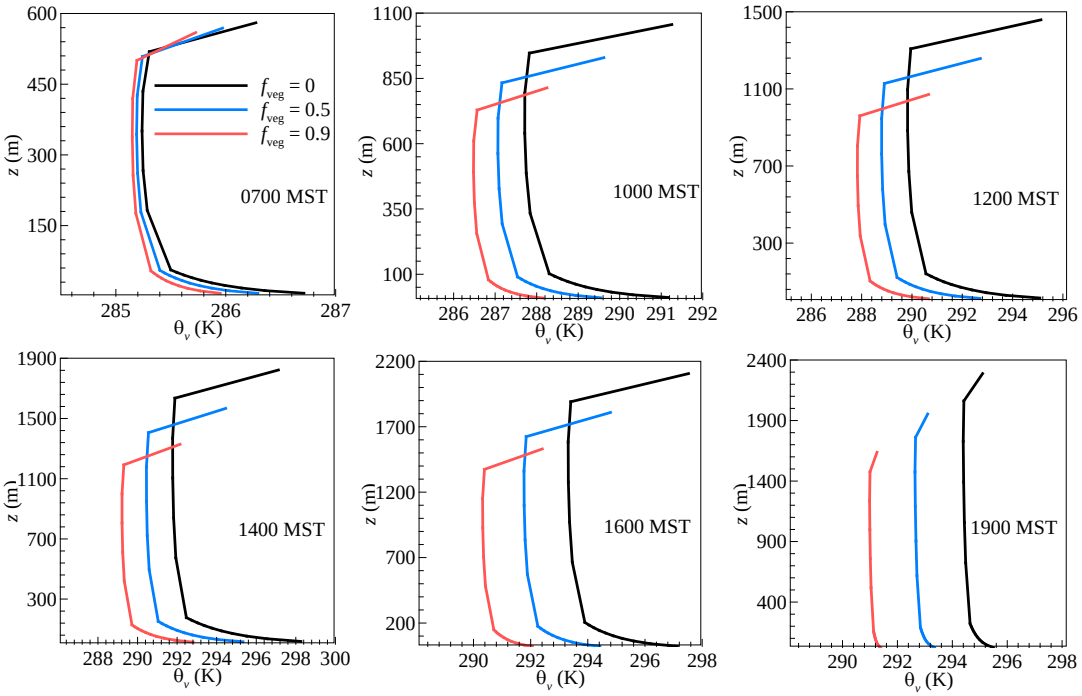

Figure 2.12: Model predictions of virtual potential temperature profiles in the ABL at 0700, 1000, 1200, 1400, 1600 and 1900 MST for roof vegetation fraction f_{veg} = 0, 0.5 and 0.9.

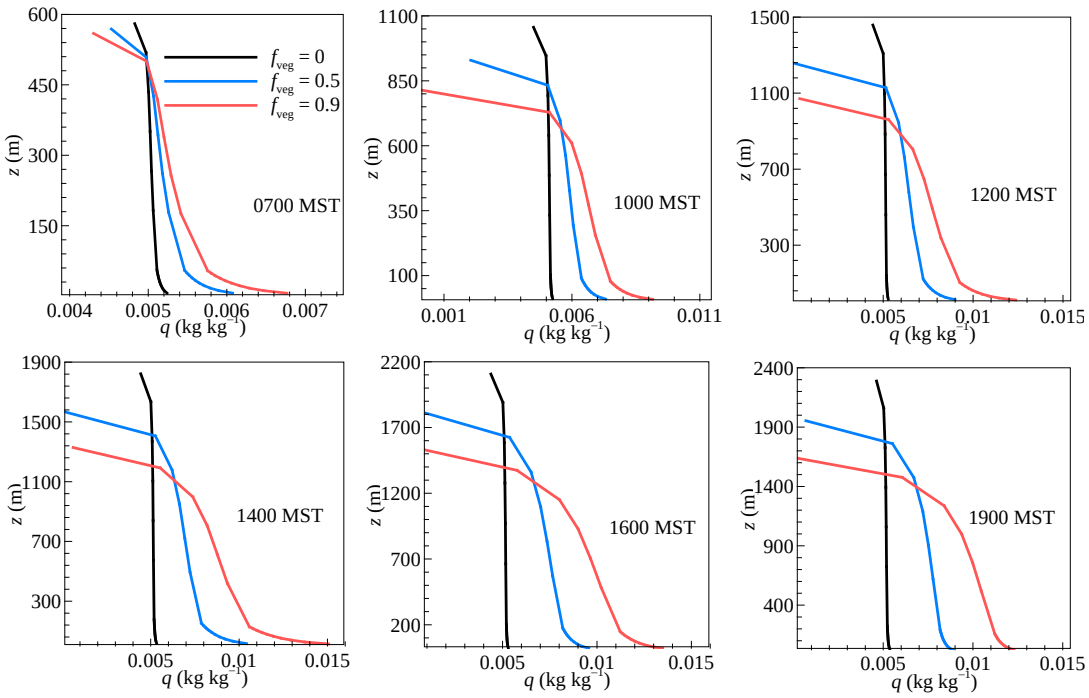

Figure 2.13: Model predictions of specific humidity profiles in the ABL at 0700, 1000, 1200, 1400, 1600 and 1900 MST for roof vegetation fraction f_{veg} = 0, 0.5 and 0.9.

2.4.4 Effects of aerodynamic roughness length

The turbulent transport of momentum, heat and moisture in the ABL is sensitive to the surface aerodynamic roughness (Mascart et al., 1995). As shown in Eqs. 7-9, the aerodynamic resistance r_a directly affects the magnitude of sensible and latent heat fluxes. It is well-known that r_a decreases nonlinearly with the surface roughness length (for example, changing the surface from a smooth concrete surface to a porous concrete surface or from short grasses to tall shrubs) (e.g. Stull, 1988). In this case study, the values of roof roughness length for momentum transfer were modified (viz. $z_{m,R}$ = 0.1, 1, and 10 mm) to investigate the same set of ABL responses (i.e. z_h and mixed-layer θ_v and q). It is expected that roofs with larger $z_{m,R}$ induce lower r_a, which in turn leads to larger H_s and LE_s due to the enhanced vertical turbulent transfer of heat and moisture. The enhanced sensible and latent heat fluxes from the surface layer then lead to higher z_h and

higher θ_v and q in the mixed layer, as shown in Figure 2.6(d), Figure 2.14, and Figure 2.15 respectively. In the context of urban planning, particularly for UHI mitigation, results of this case study also demonstrate that altering roof roughness lengths is effective in regulating the transport of heat and moisture from built terrains to the overlying CBL, without fundamental changes to the urban morphology.

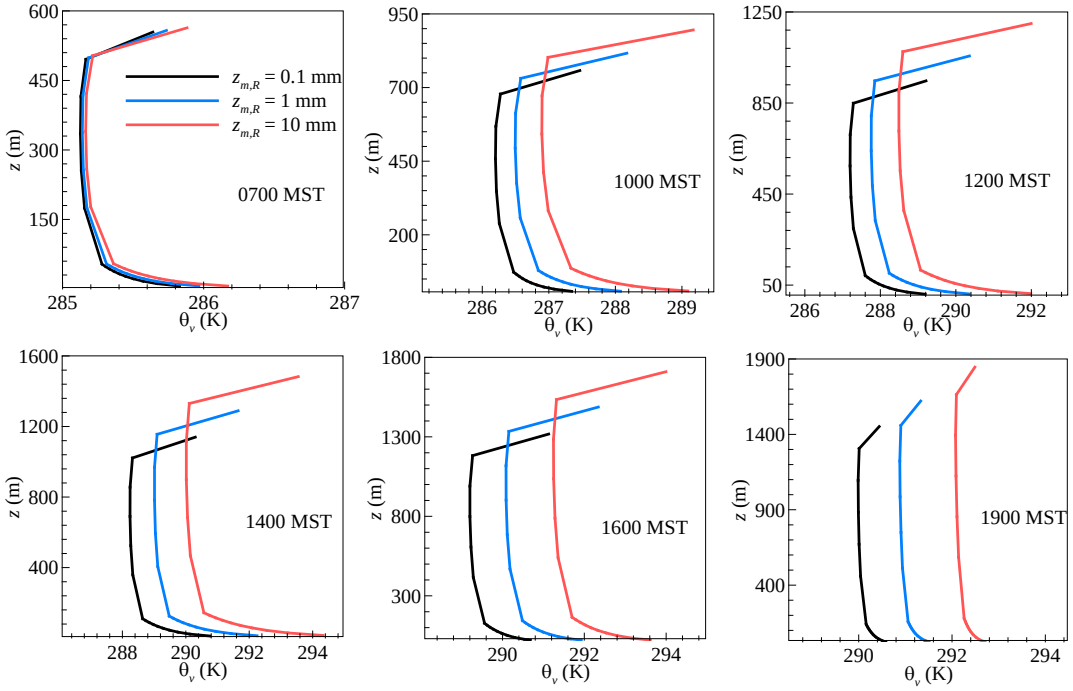

Figure 2.14: Model predictions of virtual potential temperature profiles in the ABL at 0700, 1000, 1200, 1400, 1600 and 1900 MST for roof aerodynamic roughness length $z_{m,R}$ = 0.1, 1 and 10 mm.

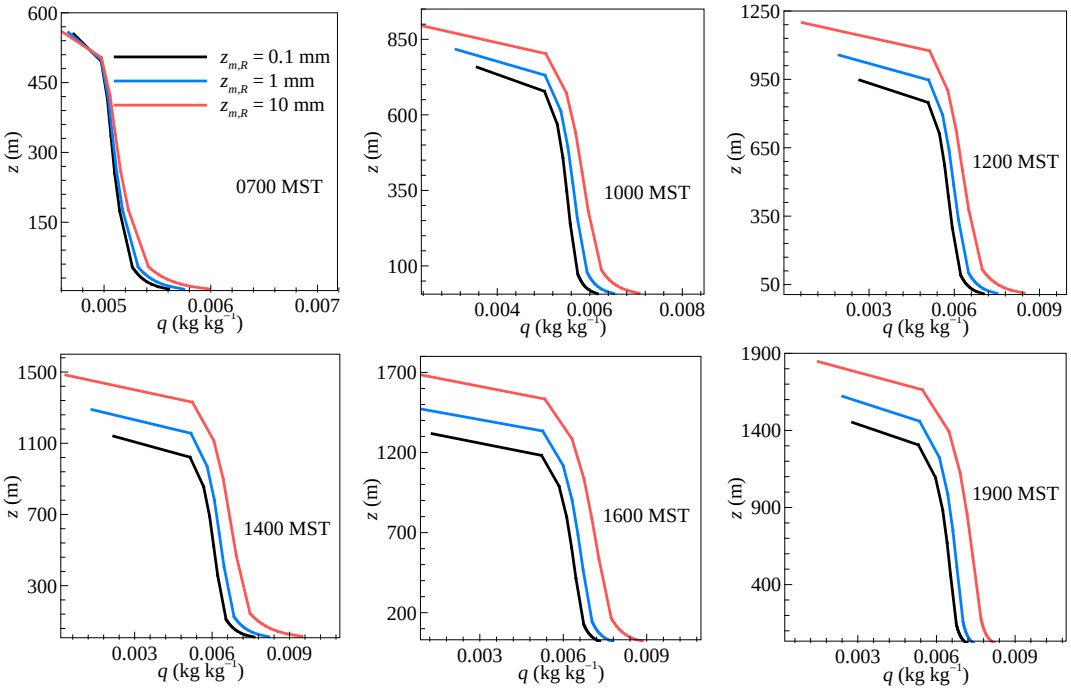

Figure 2.15: Model predictions of specific humidity profiles in the ABL at 0700, 1000, 1200, 1400, 1600 and 1900 MST for roof aerodynamic roughness length $z_{m,R}$ = 0.1, 1 and 10 mm.

2.5 Summary

In this chapter, a new SLUCM-SCM framework is developed for modelling the urban land-atmosphere interactions, with the SLUCM enabling the realistic representation of urban surface hydrologic processes including evapotranspiration, infiltration, irrigation, and sub-surface soil moisture. The model was validated against field measurements of net radiation and sensible and latent heat fluxes in urban canopy layers, as well as vertical distributions of temperature and humidity and the growth of ABL height. The coupled model is found to be robust and captures the vertical transport of heat and moisture from the surface layer to the overlying CBL via land-atmosphere interactions.

The numerical framework was then applied to study the impact of urban landscape characteristics, including morphology, albedo, vegetation fraction and aerodynamic roughness on the growth of the ABL and the distributions of temperature and humidity in the mixed layer under convective conditions. Results of case studies show that changes in land-surface properties (hydrothermal or geometric) have a significant impact on the evolution of the overlying boundary layer. In particular, the urban morphology, represented by the canyon-aspect ratio h/w, imposes non-linear effects on the ABL responses (z_h growth and θ_v distribution in the mixed layer), through rather complex interactions of the opposing radiative trapping and shading effects co-evolving throughout the daytime. It is also found that widely-used urban planning strategies especially for surface UHI mitigation, such as cool and green roofs and modification of the vertical turbulent transfer through enhanced aerodynamic conductance, are effective in affecting the transport of momentum, heat and moisture in the urban boundary layers.

Preliminary results from applications of the new SLUCM-SCM framework in the current study necessitate a few important questions for future research on urban land-atmosphere interactions. First, model uncertainties inherent in the parameter space, as well as parametrization schemes, need to be carefully quantified. With a relatively large number of input parameters, model uncertainty and sensitivity analysis necessarily requires computationally efficient numerical procedures, e.g. using advanced stochastic methods.

CHAPTER 3 SENSITIVITY ANALYSIS OF THE COUPLED URBAN LAND-ATMOSPHERE MODEL

The coupled urban land-atmosphere model, i.e. SLUCM-SCM introduced in Chapter 2 is capable to predict the evolution of ABL dynamics. This modeling framework enables us to look into changes of atmospheric dynamics due to landscape modification using physical ABL parameterization, but not limited to the physics in the urban canopy layer (e.g. 2-m air temperature) prevailed in most previous study. However, the model predictability is significantly dependent on the accuracy of model input parameters. Therefore, sensitivity analysis is critical to quantify model uncertainties and improve model predictability. In this chapter, an advanced Monte Carlo method, viz. a Subset Simulation approach is adopted to test the model sensitivity (particularly ABL height, temperature and humidity) to urban land surface changes. The sensitivity analysis in this chapter will allow us to investigate some fundamental questions such as: How effective is a certain urban mitigation approach (such as the implementation of white roof or the installation of green roof) in modifying the CBL structure and to what elevation? What alternative strategies do we have in urban landscape planning in addition to the popular options such as green/white roofs?

3.1 Subset simulation

In urban climate modeling, the capability of assessing critical responses of atmospheric processes to urban land use land cover change is of paramount significance for assessment of climatic extremes. The SLUCM-SCM framework coupling urban land surface processes and CBL dynamics involves a large number of input parameters, which leads to high dimensionality of input space for the following statistical analysis. Hence an

advanced Monte Carlo method, i.e. Subset Simulation (Au and Beck, 2001; Au and Wang, 2014) is adopted for subsequent sensitivity study, which is efficient in simulating rare (very small probability) events and robust for high dimensionality. Instead of simulating rare events as in direct MCS method with expensive computational cost, Subset Simulation breaks down extreme events with small exceedance probability into a sequence of more frequent events by introducing intermediate exceedance events. The targeted small exceedance probability is then expressed as a product of larger conditional probabilities of each intermediate event. In addition, MCMC technique is adopted based on effective accept/reject rules in Subset Simulations to improve computational efficiency.

As illustrated in Figure 3.1, the sampling technique employed in the Subset Simulation proceeds as follows: In level 0 (initial state), the unconditional samples of uncertain parameters follow a prescribed probability distribution function (PDF) (Figure 3.1a). Conditional samples in level 1 are defined using a given intermediate conditional probability p_0 (e.g. $p_0 = 0.1$ stands for 10% of the level 0 samples will be selected as conditional samples) (Figure 3.1b). These samples are then generated by MCMC procedure using importance sampling at the exceedance probability $P(Y > y_1) = p_0$ (Y is a targeted response of model and y_1 is a threshold value) (Figure 3.1c). Subsequent conditional sampling are conducted by MCMC with the intermediate exceedance probability target, i.e. $P(Y > y_i) = p_0^i$ (i = 1, 2, 3, … denoting conditional levels) until simulations reach the final target with $p_f = p_0^N$, where p_f is the target probability of a rare event and N the total number of conditional levels (Figure 3.1d). Using this method, a rare event, e.g. with target exceedance probability of $p_f = 10^{-4}$ (i.e. the probability of

occurrence is less than 1 in 10,000), can be effectively broken down into 4 different sampling (1 unconditional MCS and 3 subsequent conditional MCMC) levels, each samples a moderate conditional probability of $p_0 = 0.1$.

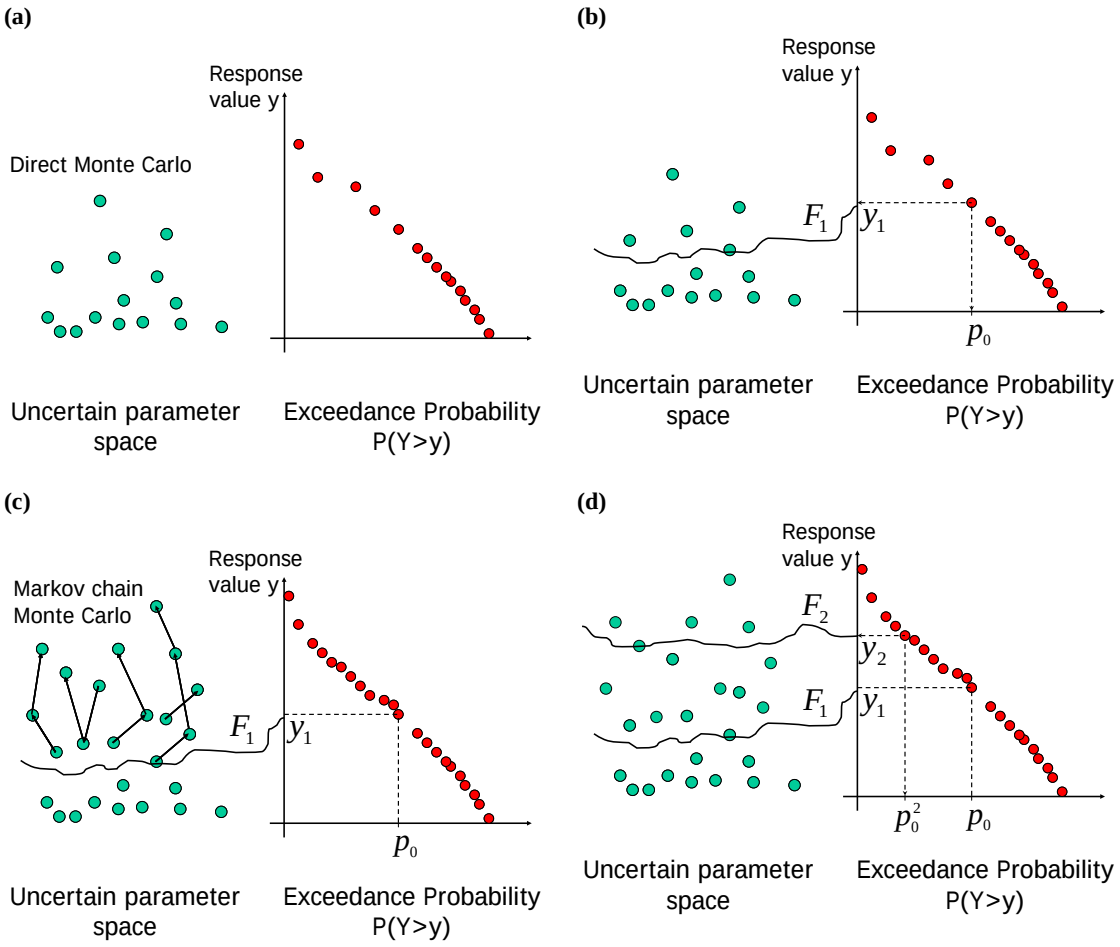

Figure 3.1: Schematic of Subset Simulation procedure: (a) level 0 (initial phase) sampling by direct MCS, (b) determination of level 1 samples F_1 given conditional exceedance probability p_0, (c) populating conditional samples in level 1 by MCMC procedure, and (d) forwarding algorithm to subsequent conditional levels till the target exceedance probability $p_f = p_0^N$ is reached.

To evaluate the statistical quality of Subset Simulation, the coefficient of variation (c.o.v., defined as the ratio of the standard deviation to the mean) was computed using a typical statistical average of 30 independent runs. The resulted c.o.v. of Subset Simulation as a function of exceedance probability is shown in Figure 3.2, where c.o.v. of

direct MCS is also shown for comparison. Estimate of c.o.v. of direct MCS can be analytically formulated as $[(1-p_i)/(p_i N_T)]^{1/2}$ (Au and Beck, 2001), where p_i is the exceedance probability and N_T the number of samples at corresponding MCMC level i. It is clear that the c.o.v. of Subset Simulation is significantly smaller than that of direct MCS, especially at the higher MCMC level (smaller probability), indicating less statistical error for exceedance probability estimates using Subset Simulation.

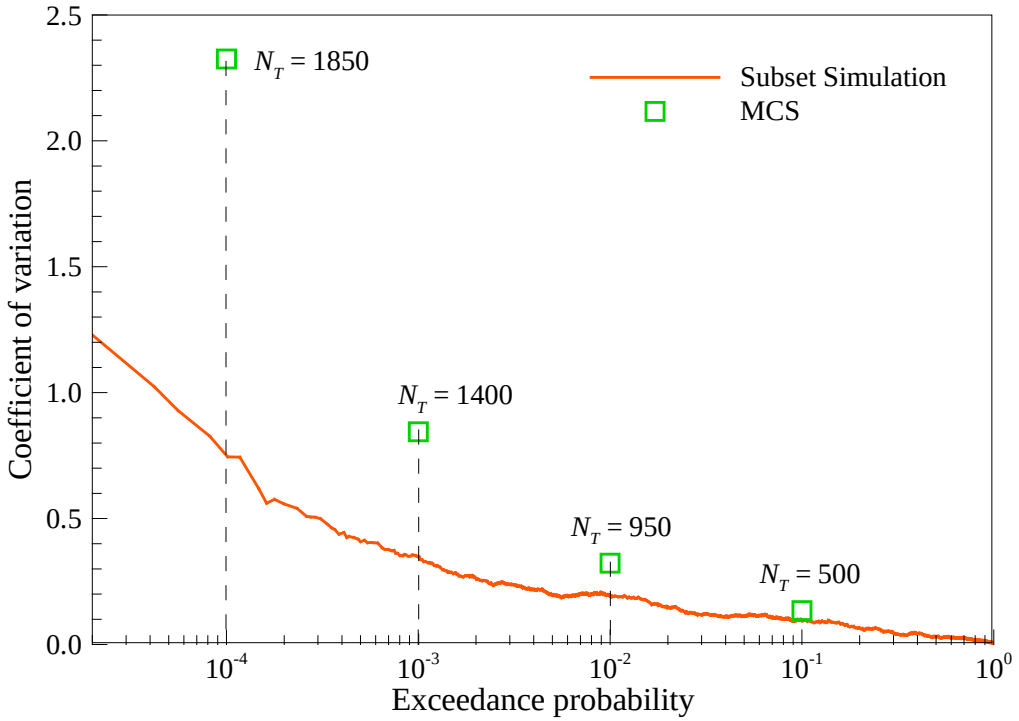

Figure 3.2: Comparison of the coefficient of variation (c.o.v.) of exceedance probability in Subset Simulation and direct MCS.

3.2 Results of sensitivity analysis

In this section, Subset Simulation was applied to analyze the sensitivity of the coupled SLUCM-SCM to different input parameters. The meteorological forcing in the surface layer was prescribed using field measurements of an eddy covariance tower on a clear day (14 June 2012) provided by the Central Arizona-Phoenix Long Term Ecological Research (CAP LTER) project (Chow et al., 2014). The inputs of diurnal air temperature, relative humidity, and downwelling shortwave and longwave radiation are plotted in Figure 3.3, with the daytime from 6:00 am to 7:30 pm (local time) for the development of CBL. With the prescribed meteorological forcing, the surface sensible and latent heat fluxes are predicted by the SLUCM, which then in turn drive the SCM to estimate temperature and humidity profiles in the mixed layer. The input parameters of SLUCM-SCM (including surface dimensional and hydrothermal parameters for the SLUCM and atmospheric parameters for the SCM) in the control case are presented in Table 2.2. Note that the initial soil water content for green roofs in the SLUCM is set as 90% saturated for the subsequent 13.5-hour of simulation after the beginning of CBL development such that the evaporative power of green roofs is not constrained by soil water availability. Among the model inputs as described in Table 2.2, 15 parameters are selected for subsequent sensitivity analysis, including 6 surface thermal parameters (i.e. a_{Rv}, $C_{Rv,}$ k_{Rv}, a_{Rc}, C_{Rc}, k_{Rc}), 3 surface hydrological parameters (i.e. W_s, W_r, K_s), 4 surface dimensional parameters (i.e. r, h/w, $Z_{m,Rc}$, $Z_{m,Rv}$), and 2 atmospheric parameters (i.e. w_e, $\gamma_{\theta v}$) as listed in Table 3.1 (Note that the subscripts *Rc* and *Rv* denote conventional and green roof respectively). In addition, PDFs of these parameters are determined based on previous studies (Ouwersloot and Vilà-Guerau de Arellano, 2013; Wang et al., 2011a; Yang and

Wang, 2014b) and local conditions in our study area. Care must be taken here that this particular selection of uncertain parameter space is by no means exhaustive or unique, and is subject to the limitation of parameterization used in the numerical framework and the subsequent analysis can, at best, represents only the *model* physics. Since the initial parameter distribution by direct MCS are pivotal to the statistical sampling efficiency of Subset Simulations, PDFs for uncertain parameters are carefully selected to constitute a physically realistic parameter space. In addition, it was found that normal (Gaussian) distribution is more realistic for thermal and hydrological parameters with the expected value in a physical range having higher probability, while the distributions of dimensional (geometric) parameters are subject to engineering design and is therefore more uniform (Wang et al., 2011a). The two atmospheric parameters at the top of CBL (i.e. entrainment rate and lapse rate) are also set as uniform distribution to achieve same probability for different top boundary conditions according to Ouwersloot and Vilà-Guerau de Arellano (2013).

Table 3.1: Summary of statistics of uncertain parameters used in the sensitivity study

Type	Parameter	Unit	PDF	Min	Max	Mean	Std dev
Surface thermal parameters	a_{Rv}	-	Normal	0.05	0.6	0.18	0.045
	C_{Rv}	MJ m^{-3} K^{-1}	Normal	0.1	2	0.72	0.18
	k_{Rv}	W m^{-1} K^{-1}	Normal	0.15	4	0.85	0.213
	a_{Rc}	-	Normal	0	1	0.15	0.0375
	C_{Rc}	MJ m^{-3} K^{-1}	Normal	0.1	4	1.52	0.38
	k_{Rc}	W m^{-1} K^{-1}	Normal	0.2	3	1.2	0.3
Surface hydrological parameters	W_s	-	Normal	0.3	0.6	0.44	0.074
	W_r	-	Normal	0.04	0.2	0.074	0.025
	K_s	m s^{-1}	Normal	0.1	100	1.7	0.43
Surface dimensional parameters	r	-	Uniform	0.3	0.8	-	-
	h/w	-	Uniform	0.25	8	-	-
	$Z_{m,Rc}$	mm	Uniform	0.1	5	-	-
	$Z_{m,Rv}$	mm	Uniform	10	200	-	-
Atmospheric parameters	w_e	m s^{-1}	Uniform	0.1	0.3	-	-
	$\gamma_{\theta v}$	K km^{-1}	Uniform	3	7	-	-

(a)

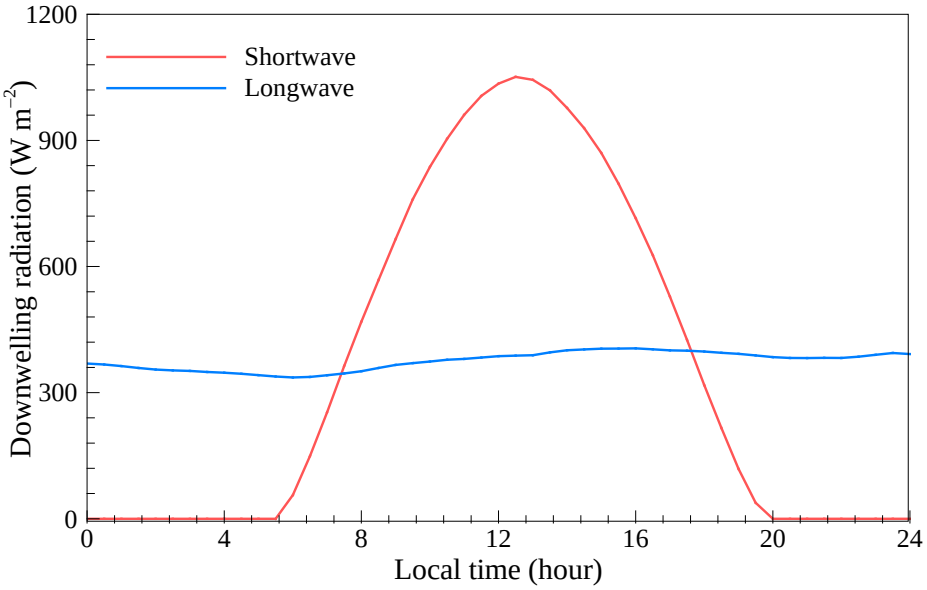

(b)

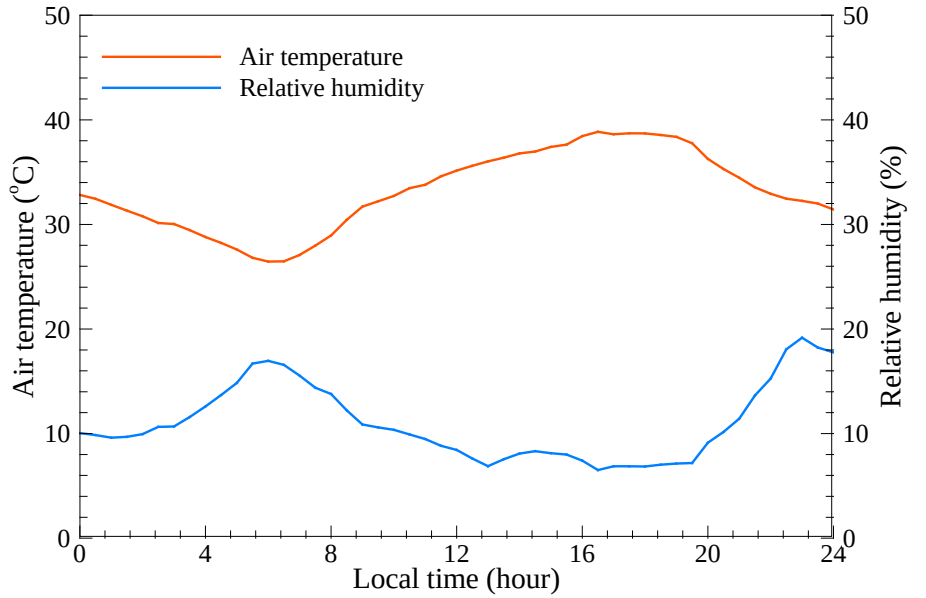

Figure 3.3: The diurnal surface atmospheric forcing of June 14, 2012 (a clear day) in Phoenix, AZ: (a) downwelling shortwave and longwave radiation and (b) air temperature and relative humidity. The daytime data between starting point (6:00 am local time) and ending point (7:30 pm local time) are used to drive the SLUCM-SCM under convective condition.

3.2.1 Critical model responses

Three atmospheric variables, i.e. the critical CBL height (z_h), the mean virtual potential temperature (θ_v), and the mean specific humidity (q) in the mixed layer are selected as model responses to assess the impact of urban land surface characteristics on the overlying atmosphere. The surface meteorological conditions as prescribed in Figure 3.3 are kept as invariant, while only the surface landscape properties (i.e. thermal, hydrological, dimensional parameters) will be changed. For each monitored output, three different cases with the fraction of green roof vegetation of 0, 0.5, and 1.0, respectively were simulated. Note that vegetation on ground (though the model is capable of) is excluded in the current model setting, so roof vegetation is the only moisture source. This model set-up allows us to analyze exclusively the effectiveness of green roofs, one of the urban environmental mitigation strategies of particular interest to researchers and city planners. For all three cases, three conditional levels are used with a conditional probability of $p_0 = 0.1$, which is equivalent to a sequence of exceedance probabilities of 10^{-1}, 10^{-2}, and 10^{-3} for MCMC levels 1, 2 and 3, respectively. In total, 270 simulations were run (30 independent simulations per case for 9 cases) with 1450 realizations of the set of 15 uncertain parameters in each run to ensure the simulation results are statistically significant.

Plots of exceedance probabilities versus various model responses averaged over 30 simulations are presented in Figure 3.4. The variations of critical model outputs with three different green roof fractions indicate the sensitivity of roof greening degrees on CBL dynamics. In Figure 3.4 (a)&(b), the CBL height and virtual potential temperature of mixed layer under three conditions of green roof fractions (i.e. $f_{veg} = 0$, 0.5, and 1)

were monitored. In general, larger green roof fractions lead to lower z_h and smaller θ_v. This is expected since urban landscapes with larger fraction of vegetation distribute solar energy into more latent heat and less sensible heat, due to evaporative cooling. Less sensible heat and reduced surface temperature both lead to reduced CBL height and virtual potential temperature.

It is also noteworthy that there exist log concavities for the exceedance probabilities of both critical z_h and θ_v with f_{veg} = 1 (100% roof greening). The occurrence of log concavities is related to energy balance in the street canyon where nonlinear effect of canyon aspect ratio h/w was observed (Song and Wang, 2015a). Detailed explanations of aspect ratio effects will be described in Section 4.1. In Figure 3.4 (c), the specific humidity of mixed layer under three conditions of green roof fractions (i.e. f_{veg} = 0.1, 0.5, and 1) was monitored. As roof is set as the only moisture source, urban land surface is completely dry with f_{veg} = 0 and resulted in no moisture in the atmosphere in the absence of horizontal advection. Larger green roof fraction tends to produce higher q in the overlying CBL. In contrast to z_h and θ_v, exceedance probability distribution of critical response of q does not exhibit log concavity because the moisture source is purely from roofs and canyon aspect ratio and building density have no contribution.

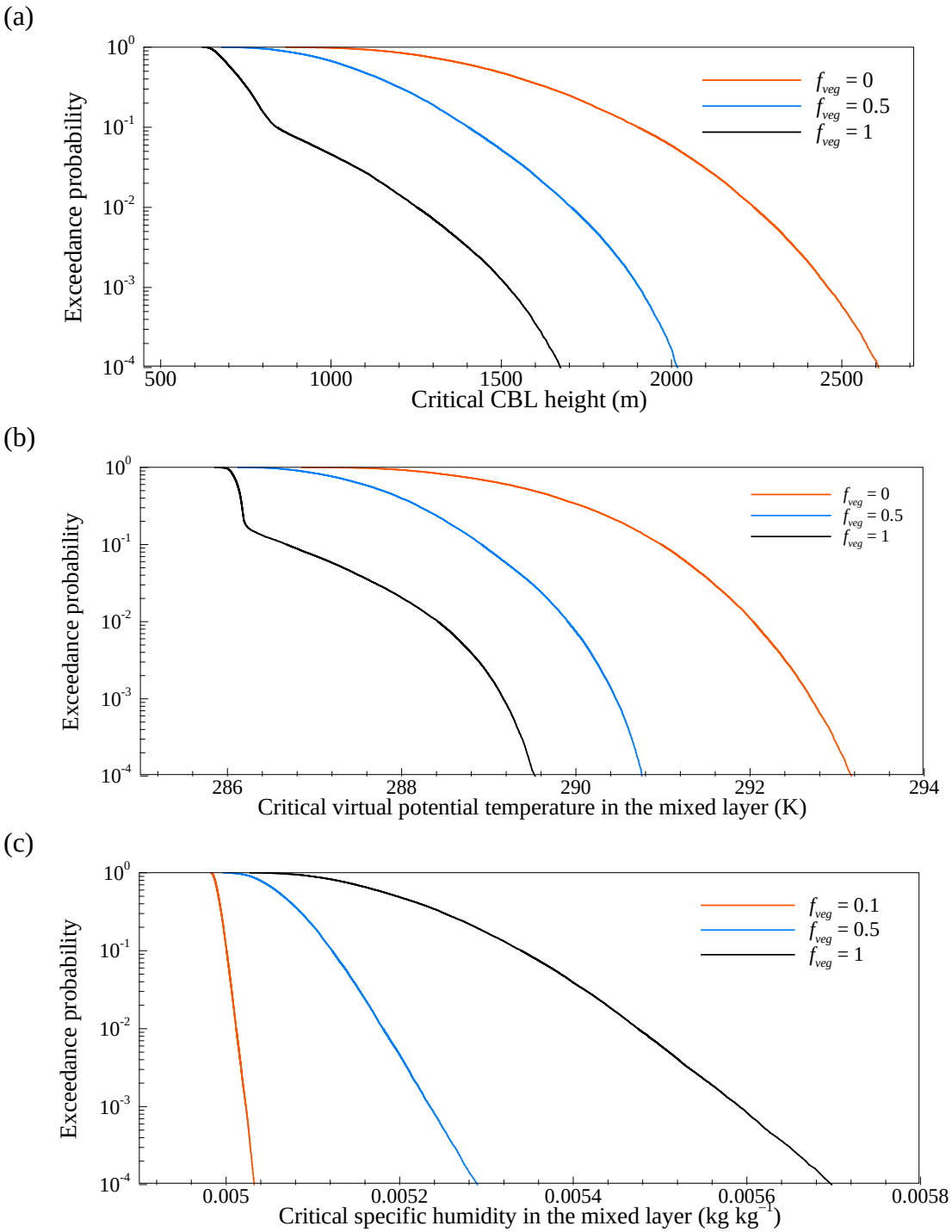

Figure 3.4: Estimates of exceedance probabilities for model outputs of critical (a) CBL height, (b) virtual potential temperature, and (c) specific humidity with different green roof fractions.

3.2.2 Statistical quantification of model sensitivity

In general, for an uncertain parameter, the deviation between the distribution of MCMC-generated conditional samples (in levels 1, 2, and 3) and the initial prescribed distribution sampled using direct MCS (level 0) indicates the significance of parameter sensitivity with respect to the corresponding model output. Figure 3.5 shows the comparison between conditional distribution (histograms) and initial distribution (dashed line) for two sample parameters, i.e. heat capacity of green roof C_{Rv} and canyon aspect ratio h/w respectively, for a typical simulation with f_{veg} = 1.0 and critical q as model output. It is clear that the critical response of q is more sensitive to C_{Rv} with noticeable deviation of sample distribution at each conditional level (Figure 3.5a), while h/w is relatively insignificant in influencing q with small deviation of sample distribution (Figure 3.5b). The result is physical as variation of C_{Rv} affects roof surface energy balance, which in turn influences the humidity profile in the CBL through surface moisture flux. On the contrary, since green roofs are the only moisture source in our setting, altering h/w has negligible effect on the atmospheric moisture for the street canyon with no vegetation on ground or wall.

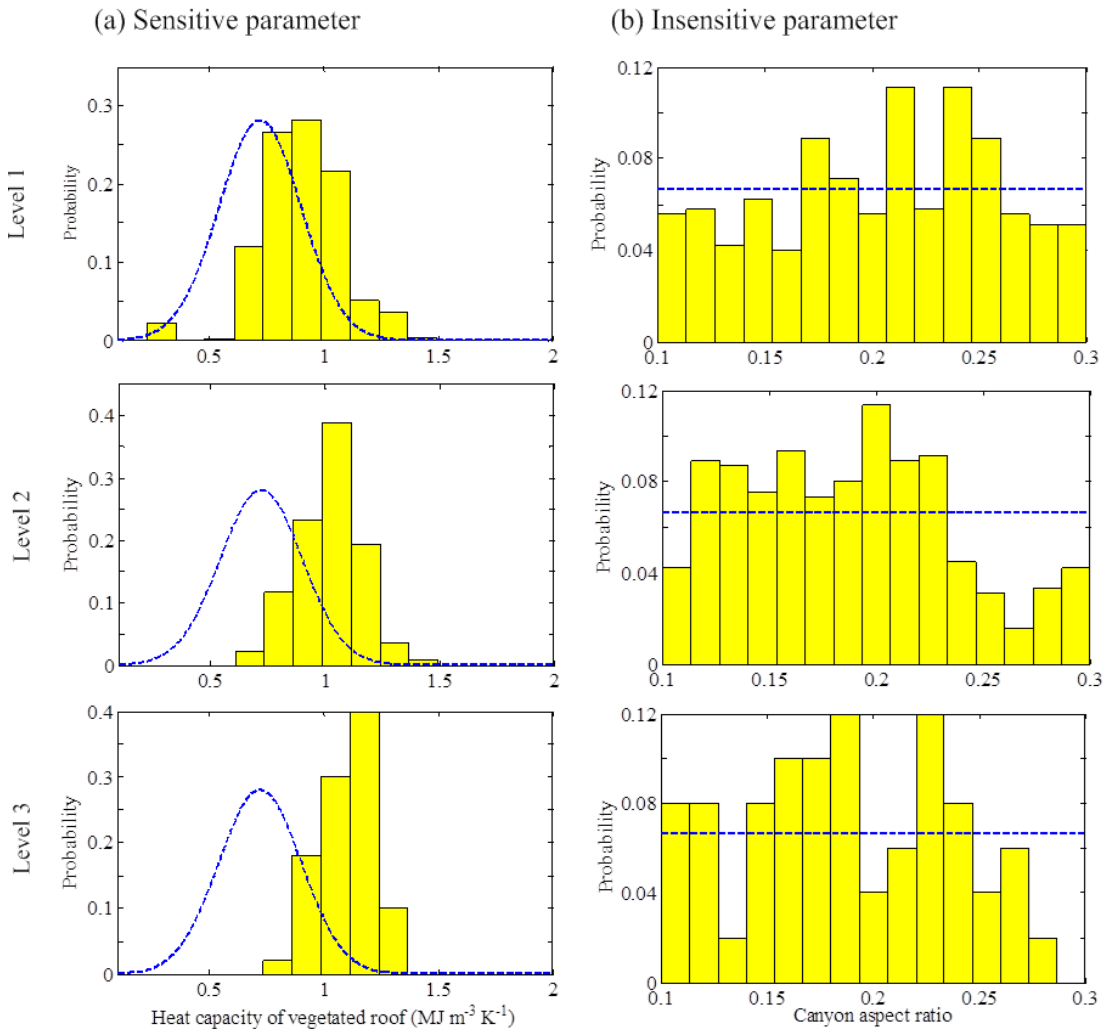

Figure 3.5: Histogram of conditional samples at different conditional levels for (a) a sensitive parameter, and (b) an insensitive parameter for a typical simulation with f_{veg} = 1.0 and critical q as model output.

To better quantify the parameter sensitivity, a percentage sensitivity index (PSI) (Wang et al., 2011a) is adopted here to measure the model sensitivity to an uncertain parameter X by calculating the average deviation of conditional sample means to that of the original PDF:

$$\mathrm{PSI}[X] = \frac{1}{N}\sum_{i=1}^{N}\frac{E\left[X \mid Y > y_i\right] - E[X]}{E[X]}, \tag{3.1}$$

where i is the conditional (MCMC) level index, $N = 3$ the total conditional levels, $E[X]$ the statistical mean (expected value) of the original unconditional distribution in level 0 (as in Table 3.1), $E[X \mid Y > y_i]$ the mean value of X at conditional level i, Y the value of monitored model response, and y_i the threshold values at exceedance probability of each intermediate level i. The magnitude of PSI quantifies the significance of sensitivity, while the sign of PSI indicates the correlation between monitored output Y and input parameter X, i.e. positive PSI means increasing X will lead to an increase of output Y and negative PSI means increasing X will lead to a decreased Y.

PSI values of all uncertain parameters for three different monitored outputs, i.e. z_h, θ_v, and q, with different green roof fractions are presented in Table 3.2. For better visualization, bar plots of PSI values are also shown in Figure 3.6. As shown in Figure 3.6 (a) and (b), both z_h and θ_v are highly sensitive to surface dimensional parameters, including normalized roof width r, canyon aspect ratio h/w, and roughness length of momentum for conventional roofs $Z_{m,Rc}$. Note that r is positively correlated with critical z_h and θ_v for conventional roofs while the correlation is negative for green roofs. Both critical z_h and θ_v are negatively correlated with h/w and positively correlated with $Z_{m,Rc}$. Moderate sensitivity of critical z_h and θ_v is found with respect to thermal parameters of conventional roofs including albedo a_{Rc}, heat capacity C_{Rc}, and thermal conductivity k_{Rc}. Also note that there are opposite correlations for atmospheric parameters w_e and γ_θ: z_h is positively correlated with w_e and negatively correlated with γ_θ; but the correlations are opposite for model output of critical θ_v. From Figure 3.6 (c), mixed layer q is highly sensitive to r and thermal properties of green roofs and moderately sensitive to $Z_{m,Rv}$.

Physical mechanisms governing the model sensitivity and its implications to urban planning are discussed below.

Table 3.2: Estimates of PSI values for critical CBL height z_h, virtual potential temperature θ_v, and specific humidity q in the mixed layer, each averaged over 30 runs.

Uncertain parameters	z_h			θv			q		
	$f_{veg} = 0$	0.5	0	$f_{veg} = 0$	0.5	1	$f_{veg} = 0.1$	0.5	1
a_{Rv}	-1.44	-0.86	2.67	-0.19	0.03	1.65	2.95	7.64	6.81
C_{Rv}	-0.46	3.12	0.21	-0.59	0.27	0.03	22.23	37.78	39.76
k_{Rv}	0.54	-1.60	-0.17	1.13	-0.40	0.06	24.35	36.02	35.48
a_{Rc}	-15.67	-8.30	-1.60	-18.69	-11.79	-0.37	3.73	6.09	-0.98
C_{Rc}	-12.10	-6.41	-0.39	-14.49	-9.50	-0.29	5.93	2.26	-2.02
k_{Rc}	-17.60	-11.29	0.67	-23.33	-11.35	0.65	2.89	3.93	-0.91
W_s	0.35	-1.36	0.24	-0.04	0.34	-0.17	-0.49	1.39	1.84
W_r	1.63	1.41	2.70	0.44	0.22	2.26	3.59	1.11	1.00
K_s	-0.17	-2.48	0.64	0.24	-1.59	-1.89	-0.90	0.53	-1.94
r	29.73	5.59	-25.08	34.60	2.65	-26.72	27.95	33.55	37.17
h/w	-33.23	-69.41	-87.32	-40.08	-79.89	-89.15	3.95	7.55	5.86
$Z_{m,Rc}$	38.53	34.42	1.00	42.58	24.38	-1.13	-9.76	-7.75	7.72
$Z_{m,Rv}$	0.26	-0.31	-5.36	0.53	-1.00	-0.26	-15.41	-16.77	-1.28
w_e	20.16	19.78	10.91	-14.61	-14.93	-6.65	-1.45	-4.03	-1.55
γ_{qv}	-33.46	-32.33	-19.91	27.22	22.62	12.84	6.20	5.20	6.12

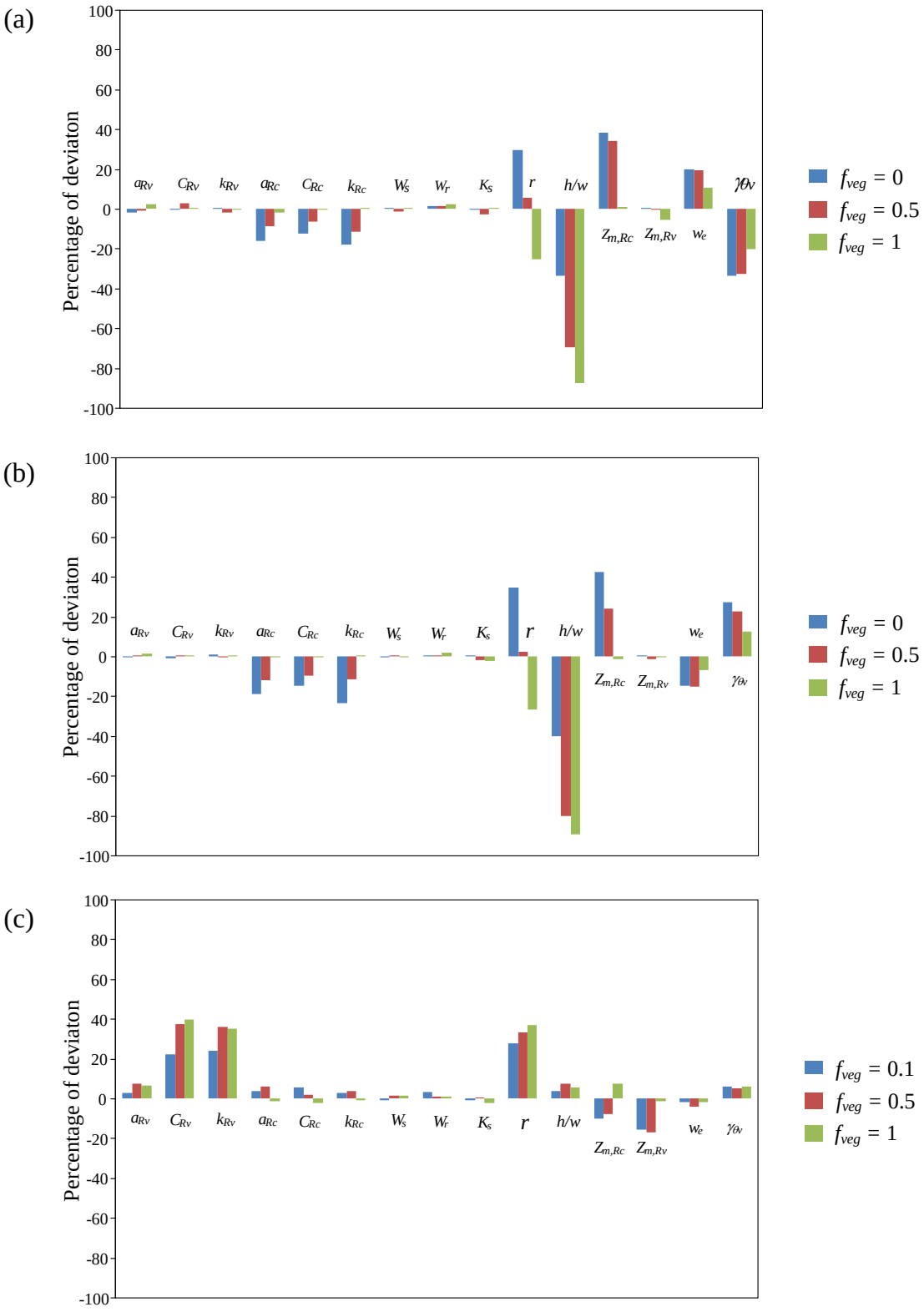

Figure 3.6: PSI values for model outputs of critical (a) z_h, (b) mixed layer θ_v, and (c) mixed layer q, with different green roof fractions.

3.3 Implications of sensitivity results

The UHI effect has attracted significant effort, even heated debate from urban climate researchers and city planners. UHI is characterized by elevated temperature in built environments compared to surrounding rural areas (Oke, 1982). Major contributors of UHI include: (a) excess storage of thermal energy due to radiative trapping by street canyon and thermal properties of pavement materials, (b) reduced vegetation cover and evaporative cooling and (c) the release of anthropogenic heat, moisture, and greenhouse gases (Santamouris, 2014; Sun et al., 2013). Correspondingly, there are several popular UHI mitigation strategies, including (1) changing canyon geometry (characterized by aspect ratio and roughness lengths) to alter the energy distribution through radiative shading and trapping; (2) changing thermal properties, such as installing cool roofs or cool pavements to reflect more solar radiation by increasing surface albedo; (3) adding green spaces, such as green roofs to increase evapotranspiration in urban area. In the subsequent contexts, the effects of these UHI mitigation strategies on the overlying atmosphere are discussed based on the sensitivity study, and its implication to urban planning.

3.3.1 Impact of urban morphology

Building geometry and density in an urban area have a significant impact on the partitioning and redistribution of solar energy in the surface layer, which in turn modulate the energy transport processes in the overlying atmosphere. The canyon aspect ratio h/w is a typical indicator of building geometry and density in urban planning (Ali-Toudert and Mayer, 2006; Krüger et al., 2011; Theeuwes et al., 2013). Low h/w signals low building (small h) or sparse building density (large w), while high h/w indicates high

building (large h) or intensive building density (small w). With variable aspect ratio ranging from 0.25 to 8, log concavity is found in the exceedance probability estimates for critical z_h and θ_v in the case of f_{veg} = 1.0 as shown in Figure 3.7 (a) and (b). This log concavity is correlated with the nonlinear effect of the canyon aspect ratio on CBL height and virtual potential temperature, due to two counteracting processes, viz. shading effect and radiative trapping effect in the street canyon, as investigated by (Song and Wang, 2015a). To further test the nonlinear effect of h/w on CBL dynamics, the canyon aspect ratio is set as constant, and as a result the log concavity disappears as shown in Figure 3.7. The log concavity of variable h/w demarks the switching from small h/w case to high h/w case with a nonlinear interaction between radiative shading and trapping effects. In addition, at mesoscale atmospheric modeling, the canyon aspect ratio is closely related to the surface roughness of a built terrain, which in turn modulates the surface aerodynamic resistance under convective condition and further complicate the nonlinear effect.

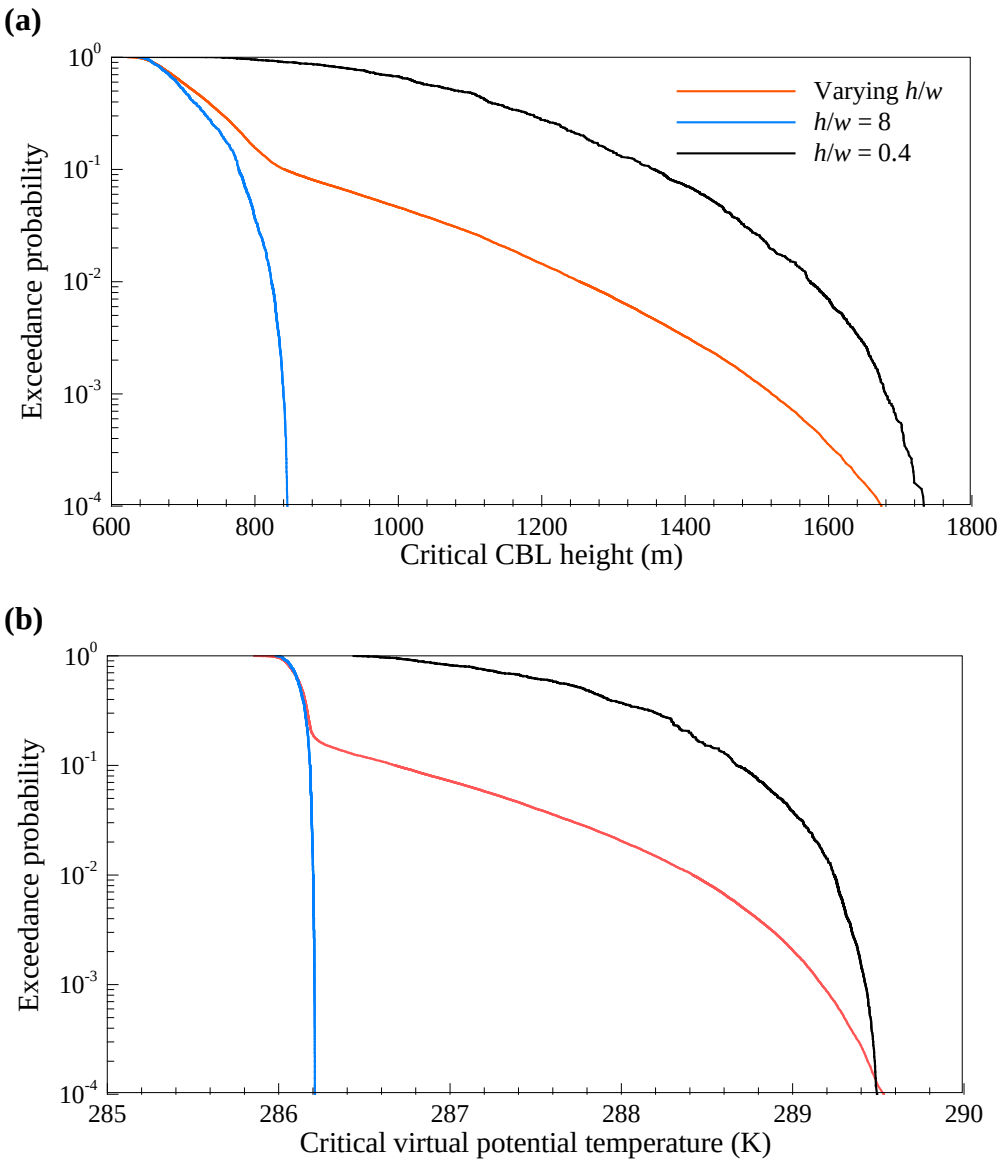

Figure 3.7: Illustration of the nonlinear effect of apect ratio h/w on critical model responses of (a) z_h and (b) θ_v of the CBL.

3.3.2 Impact of thermal properties

As shown in Figure 3.6, CBL states (z_h, θ_v, and q) are moderately sensitive to surface thermal properties. Specifically, a_{Rc}, C_{Rc}, and k_{Rc} of conventional roofs are important parameters in modulating z_h and θ_v, whereas q is sensitive to C_{Rv} and k_{Rv} of green roofs. Higher albedo causes more solar energy being reflected and less sensible

heat arising from roofs, leading to smaller z_h and θ_v. Moderate model sensitivity to a_{Rc} demonstrates that implementation of white/cool roofs with higher reflectivity is an effective way in reducing not only environmental temperature in the urban surface layer, but also the one in the overlying mixed layer.

It is also noteworthy in Figure 3.6 that thermal properties of conventional roofs and those of green roofs have opposite correlation to different CBL dynamics, which can be explained by plausible mechanisms governing surface energy balance. In Figure 3.6 (a)&(b), both boundary layer height (z_h) and temperature (θ_v) are negatively correlated with albedo, heat capacity and thermal diffusivity of conventional roof. In Figure 3.6 (c), boundary layer humidity (q) is positively correlated with heat capacity and thermal diffusivity of green roof. For a conventional roof, larger heat capacity implies that more thermal energy is needed to heat the roof, while higher thermal conductivity implies that less time is needed for heat dissipation, both leading to lower roof surface temperature (Wang et al., 2011b). Lower roof surface temperature will then reduce the surface sensible heat (given other conditions invariant), which will further lead to lower temperature in the mixed layer and lower CBL height according to Eqn. (2.15) and Eqn. (2.30) respectively. On the other hand, to increase boundary layer humidity (q), more latent heat from green roofs needs to be supplied so that sensible heat will decrease. This potentially causes green roof surfaces to be cooler than the atmosphere, giving rise to the "oasis" effect commonly observed over surfaces with significant evaporative cooling (Stull, 1988). As a result, sensible heat flux can be negative and flowing towards the surface. Under this condition, larger heat capacity and thermal conductivity of green roofs increase the ground heat flux, and are positively correlated to q via evaporative

cooling. Nevertheless, it is noteworthy that what PSI values can reveal is limited by the physics of the SLUCM-SCM framework, e.g. the impact of horizontal advection on the sensitivity is not accounted. The actual physics of urban land-atmosphere interactions involves more complicated land surface and atmospheric processes of heat and water transport in the integrated soil-atmosphere system due to complexity of surface energy partitioning (Yang and Wang, 2014a). For example, the existence of phase lags among land surface temperatures and energy budgets, due to subsurface heat transport with pore water advection, can lead to complex hysteresis loops (Sun et al., 2013; Wang, 2014) that are not adequately captured by the current numerical framework.

3.3.3 Impact of green roofs

Due to their ability to modify energy and water budgets in the urban surface layer, city planners are increasingly using green roofs as an effective strategy to mitigate UHI effect (Sailor et al., 2012; Susca et al., 2011; Wang et al., 2016). In our study, four sets of green roof parameters are studied: (1) thermal parameters, i.e. a_{Rv}, C_{Rv}, and k_{Rv}; (2) hydrological parameters, i.e. saturated soil water content W_s, residual soil water content W_r, and saturated hydraulic conductivity K_s; (3) roof width r; and (4) green roof fraction f_{veg}. Humidity in the CBL is moderately sensitive to green roof thermal properties with a positive correlation, as discussed above. In addition, all hydrological parameters are relatively insensitive as shown in Figure 3.6. This is plausibly due to the initial soil moisture condition (90% saturated), which is realistic provided green roofs are carefully maintained with constant irrigation. The assumption is also relevant in this study for more "manageable" urban surface characteristics for urban planning purpose. Sensitivity analysis of boundary layer dynamics related to soil water and hydrological properties of

other urban vegetation (such as urban lawns, urban agriculture, etc.), on the other hand, require further investigation (Cuenca et al., 1996; Song and Wang, 2015b).

In contrast, CBL dynamics are very sensitive to green roof width and areal fractions, as they determine the area of green roof in a built environment, which in turn strongly influence the soil water availability for evaporation. It is shown that larger green roof width r and fraction f_{veg} lead to lower z_h, smaller θ_v, and higher q in the mixed layer as a result of evaporative cooling by green roofs. This result is expected and clearly indicates the effectiveness of green roofs in regulating atmospheric dynamics above an urban area. To further test the effectiveness of green roofs, the same set of model outputs, viz. z_h, θ_v and q was monitored with f_{veg} ranging from 0% to 100% with an increment of 10%. Threshold values at three conditional sampling levels are plotted in Figure 3.8, i.e. y_i for i = 1, 2, and 3, with corresponding exceedance probability of 10^{-1}, 10^{-2}, and 10^{-3}, respectively. For all output variables at different conditional levels, the results can be well fitted using linear relations with high R^2 values: z_h and θ_v decrease linearly with the green roof fraction, while q increases linearly with f_{veg}. As far as UHI mitigation is concerned, the mean mixed layer temperature can be reduced by 3-4 K in either a more statistically probable (level 1) or a more statistically extreme (level 3) case with an increase of green roof fraction from 0 to 100%. It is noteworthy that in this study, the supply of soil water content to green roof systems is assumed to be ample (e.g. via urban irrigation). In an arid environment such as Phoenix, especially during drought, the trade-off between water (for irrigation) and energy (cooling load) needs to be carefully measured by city planners.

(a)

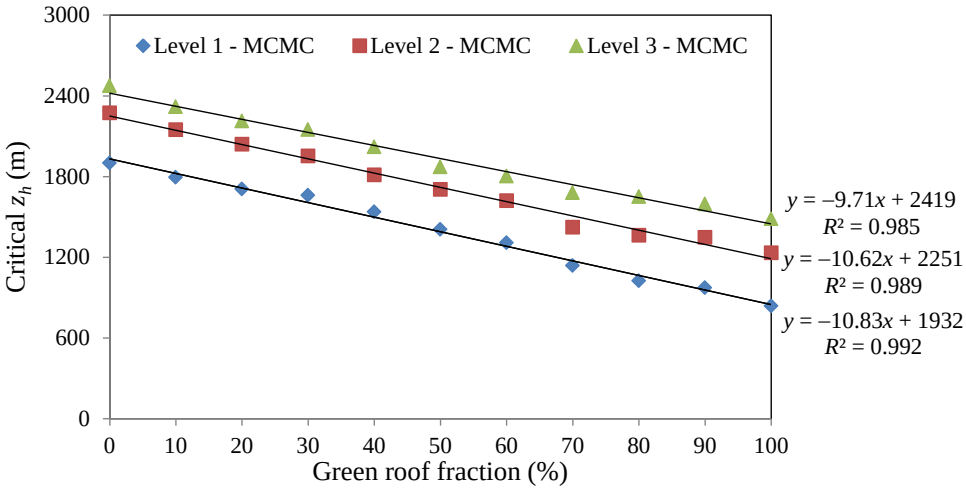

(b)

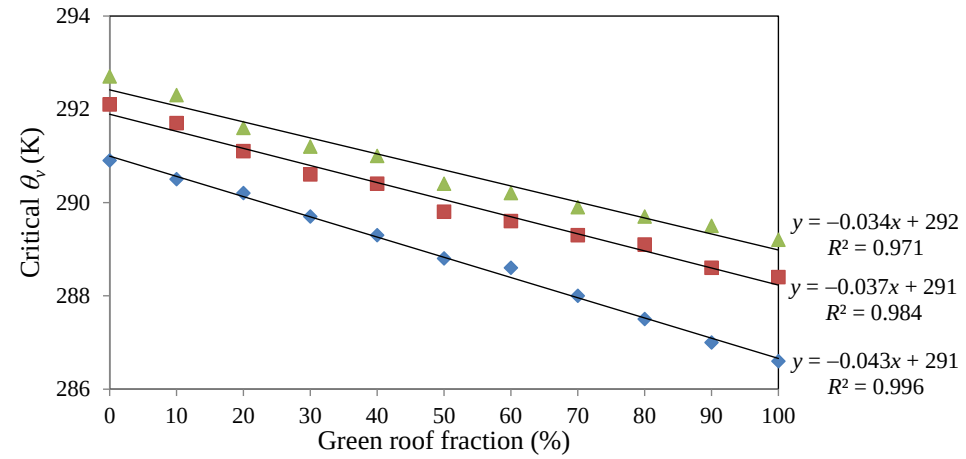

(c)

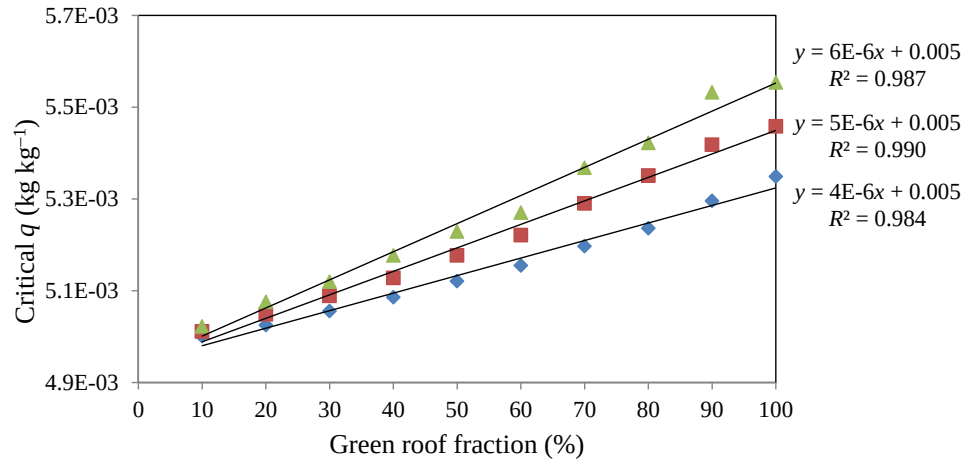

Figure 3.8: Threshold values at different conditional levels as functions of green roof fractions for critical (a) z_h, (b) mixed layer θ_v, and (c) mixed layer q. MCMC levels 1, 2 and 3 correspond to exceedance probabilities of 10^{-1}, 10^{-2}, and 10^{-3}, respectively.

3.3.4 Impact of roughness lengths

Roughness lengths of momentum and heat transfer are important land surface characteristics that regulate the aerodynamic resistance related to turbulent transport of mass, momentum and energy in the surface layer (Grimmond and Oke, 1999). Specifically, aerodynamic resistance is a function of roughness length based on MOST (Mascart et al., 1995; Wang et al., 2013). In this section, the roughness lengths of momentum at the roof level are set as uncertain parameters for both conventional and green roofs. The roughness lengths of heat transfer follow a simple parameterization that $Z_h = Z_m/10$ (Mascart et al. 1995). From Figure 3.6, both z_h and θ_v in the mixed layer are highly sensitive to $Z_{m,Rc}$, while $Z_{m,Rv}$ of green roofs plays an important role in regulating q. As indicated in Table 3.3, when critical z_h is monitored, PSI value of $Z_{m,Rc}$ is 38.53% for $f_{veg} = 0$ and 34.42% for $f_{veg} = 0.5$; for critical θ_v, PSI of $Z_{m,Rc}$ is 42.58% for $f_{veg} = 0$ and 24.38% for $f_{veg} = 0.5$. These high PSI values indicate a strong correlation between aerodynamic resistance of turbulent transfer and the CBL dynamics. This implies that altering roughness lengths of roofs (i.e. changing different vegetation types with different height over green roof and changing different materials over conventional roof) is an effective way to influence energy transport from surface to the overlying CBL without fundamental changes to the urban morphology or geometry in the street canyon.

In addition to urban landscape characteristics, the coupled SLUCM-SCM numerical framework also involves physical parameterizations at the top of CBL, i.e. in the inversion layer. The uncertainties of two atmospheric parameters, namely the entrainment rate w_e and the lapse rate of virtual potential temperature $\gamma_{\theta v}$ are tested. From Figure 3.6 (a), z_h increases with w_e and decreases with $\gamma_{\theta v}$, as expected according to Eq.

(2.23). From Figure 3.6 (b), impacts of w_e and $\gamma_{\theta v}$ on critical mixed layer θ_v are opposite. This is because larger w_e or smaller $\gamma_{\theta v}$ result in larger z_h according, which further cause smaller non-local mixing effects, leading to decrease of θ_v in the mixed layer.

3.4 Summary

In this chapter, an advanced Monte Carlo method is used to quantify the sensitivity of atmospheric boundary layer dynamics to urban land surface characteristics based on a coupled urban land–atmosphere model. Results show that in general the CBL dynamics over a built terrain are largely dictated by the urban geometry, roughness lengths, and hydrothermal properties of landscape materials. In particular, the urban geometry, represented by canyon aspect ratio, introduces a nonlinear impact on the CBL height and temperature. This is inherited from the nonlinear impact on bottom conditions of the CBL, viz. surface energy processes with two counteracting mechanisms of radiative trapping and shading in the street canyon. In addition, rooftop planning strategies strongly dictates CBL dynamics. Specifically, thermal properties of conventional and green roofs exhibit different impacts on CBL height, mixed layer temperature, and humidity, due to different surface energy partitioning. Besides, changing roughness lengths or thermal properties on rooftops (e.g. by planting different species of vegetation for green roofs, or using porous pavement materials for conventional roofs) can also be effective means in reducing urban environmental temperatures in both the surface layer and the CBL).

CHAPTER 4 IMPACT OF URBAN GREEN INFRASTRUCTURE ON URBAN MICROCLIMATE

4.1 Urban greening

Urban vegetation is effective in mitigating thermal stress (such as the heat island effect and extreme heatwaves), buffering stormwater, and fostering a healthy and friendly living environment, especially for arid cities by creating an "oasis" (Oke, 1973; Harlan et al., 2006; Yu and Hien, 2006; Bowler et al., 2010; Susca et al., 2011; Wilhelmi and Hayden, 2010; Schatz and Kucharik, 2015). Urban greening has been applied at different spatial scales by constructing public parks, residential yards, and rooftop gardens, etc. (Li et al., 2005; Gill et al., 2007; Bowler et al., 2010). For example, city parks with sizable vegetation covers usually cool the park area and the surrounding built environment (Yu and Hien, 2006; Oliveira et al., 2011). On the other hand, it is the concentrated built areas where people spend most of their time in working and living (Alexandri and Jones, 2008). The most popular way of urban greening at microscale is to vegetate envelopes of buildings, such as implementation of green roofs and walls (Alexandri and Jones, 2008; Pérez et al., 2011; Yang and Wang, 2014a), or to increase the abundance of vegetation in the built environment with parks, lawns and sidewalk trees (Spronken-Smith and Oke, 1998; Yu and Hien, 2006).

Vegetation and manmade materials differ significantly in hydrological, thermal, and aerodynamic properties, and therefore interact with the overlying ABL through different mechanisms (Bowler et al., 2010; Song and Wang, 2015a&b). The heat stress can be relieved by urban vegetation in different ways: (i) mesic vegetation (e.g. urban lawns and green roofs) is effective to reduce surface and near-surface air temperatures

compared with surrounding non-vegetated areas due to increased evapotranspiration, small heat capacity, and radiation attenuation of leaves (Park et al., 2012; Hedquist and Brazel, 2014), and (ii) xeric vegetation (e.g. xeric shade trees) can directly shade a pedestrian and limit reflected radiation in the street canyon (Martin and Stabler, 2002; Shashua-Bar et al., 2011; Martinelli et al., 2015). In the meanwhile, different vegetation types require different amounts of water for irrigation. Mesic urban landscape usually requires irrigation by sprinklers with high water demand, which is a sustainability challenge especially for arid and semi-arid cities (Gober et al., 2009; Guhathakurta and Gober, 2007). On the other hand, xeric trees are often irrigated by individual drip emitters with low water demand, which offers an attractive alternative to ameliorate urban heat problems (Martin and Stabler, 2002; Volo et al., 2014). Therefore, the vegetation type needs to be carefully selected in urban planning to achieve the balance between thermal comfort and water consumption. In addition, since urban vegetation modifies the surface energy and water budgets, these modifications may be further reflected in the dynamics of the overlying atmospheric boundary layer (ABL) due to land-atmospheric interactions.

More specifically, two types of urban heat island (UHI) need to be differentiated when urban green infrastructure is used for mitigating the UHI effect, viz. the urban canopy heat island and urban boundary-layer heat island (Oke, 1976). The thermal environment in the urban canopy layer (roughly from ground to roof level) is directly related to the thermal comfort of urban residents, while the thermal environment in the urban boundary layer (above rooftop level to ~1000m) links the local microclimate and the regional climate (Arnfield, 2003). Urban land surface modification modulates the overlying boundary layer dynamics leading to environmental changes at larger scales,

which in turn affects the hydrological and ecological processes on land surface through urban land-atmospheric interactions (Song and Wang, 2016; Seneviratne and Stöckli, 2008). Most recent urban environmental studies are focused on urban canopy layer (Georgescu et al., 2014; Li et al., 2014), while urban boundary-layer dynamics are rarely studied and in-depth analysis is hitherto lacking (Sharma et al., 2016). The objective of this study is to assess the impact of different urban greening strategies on UBL dynamics, particularly boundary-layer temperature and height. This study adds to the existing studies by bridging the gap by extending the locality in urban canopy layer studies to boundary layer environment, hence linking urban hotspots to global change at large.

4.1.1 Mesic vegetation

Here two types of mesic vegetation, i.e. lawn and green roof are selected for investigation in this chapter. The main difference between lawn and green roof lie in that the soil layer has infinite depth and heat storage underground for lawn, whereas the soil layer depth above green roof is limited (Foster et al., 2011). Different depths of soil layer above roof relate to different types of green roofs, specifically, shallow soil for extensive roof and deep soil for intensive roof (Foster et al., 2011; Li et al., 2014). Both lawn and green roof mitigate urban heat stress by reducing sensible heat flux and increasing latent heat flux. The latent heat fluxes (LE_{veg}) above lawn and green roof are calculated via

$$LE_{veg} = \frac{L_v \rho_a \left(q^*_{veg} - q_a \right)}{r_a + r_s}, \tag{4.1}$$

where L_v is the latent heat of water vaporization, ρ_a is the density of the air, q^*_{veg} is the saturated specific humidity over vegetated surface, q_a is the specific humidity of the air, r_a is the aerodynamic resistance, which is obtained from a closed-form relation proposed

by Mascart et al. (1995) as functions of surface roughness and atmospheric stability (see Appendix B for more details), r_s is the stomatal resistance of vegetation, which can be calculated by relating to vegetation type and meteorological condition. The parameterization of r_s is given in Eq. (2.12) (Noilhan and Planton, 1989; Niyogi and Raman, 1997), and reproduced here:

$$r_s = r_{s,\min} f_{SR} f_w f_e f_T / \mathrm{LAI}, \tag{4.2}$$

where $r_{s,min}$ is the minimum stomatal resistance related to the vegetation type, LAI is the leaf area index, f is the adjusting factor for meteorological variables with the subscripts SR, w, e, T denoting solar radiation, soil-water content, vapour pressure deficit and temperature respectively.

4.1.2 Xeric tree

Due to the compound shading effects of trees and walls, the radiative exchange inside the street canyon will be difficult to solve using analytical solution (Wang, 2014; Krayenhoff et al., 2014). Here, a stochastic "ray-tracing" method based on Monte Carlo algorithm is adopted to capture the radiative exchange processes inside the street canyon with xeric shade trees (Wang, 2014). For simplicity and without much loss of generality, the following assumptions are made: (1) the total incoming radiation is composed of bundles of rays with random directions and the trajectory of each ray is separately generated and traced, with its emitting directions generated by random numbers; (2) The presentation of tree crowns is simplified using cylindrical geometry with a radius of R_t, in the 2D big canyon, as shown in Figure 4.1; and (3) The dimensions of tree trunks are much smaller as compared to tree crowns, and their ray-blocking effect is negligible. Other dimensions for the geometric presentation of trees in the street canyon include the

vertical perpendicular distance from tree crown center to the ground h_t, and the horizontal perpendicular distance from tree crown center to the nearest wall d_t (see Figure 4.1).

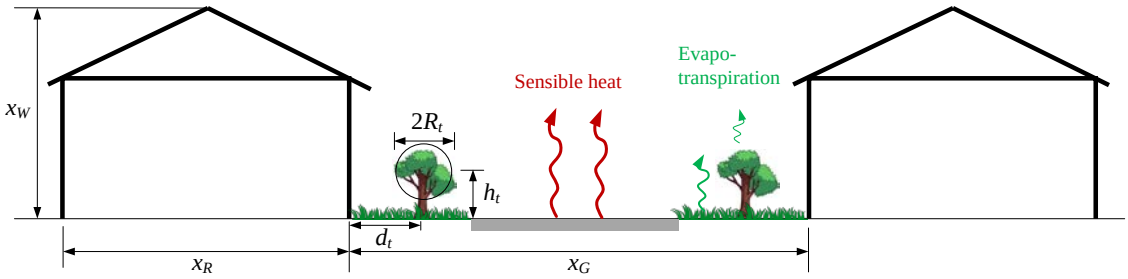

Figure 4.1: Schematic of urban land configuration and processes represented by a two-dimensional big canyon: xeric and mesic landscapes are represented by irrigated lawns and shade trees respectively.

To trace a radiative ray emitted from each canyon facet, the direction of an emitted ray from a surface (surface i) is determined by the polar angle θ_i and the azimuth angle η_i, which are given by

$$\theta_i = 2\pi R_\theta , \tag{4.3}$$

$$\eta_i = \arcsin\left(\sqrt{R_\eta}\right), \tag{4.4}$$

where R_θ and R_η are independent random numbers. This emitted ray will be traced along a randomly generated direction using Monte Carlo algorithm. If absorbed by a generic surface j, it is counted into the view factor F_{ij}. Since all reflections between six canyon and tree facets (i.e. sky, ground, two facing walls, and two symmetric tree crowns) are considered, both i and j range from 1 to 6 ($i \neq j$). Another assumption is made that all participating facets in the radiative heat exchange are Lambertian and gray, and all radiative reflections (shortwave or longwave) are diffuse in nature. Once the view factors between urban facets are determined, the radiative heat exchange for both shortwave and

longwave radiation can be readily obtained (Masson, 2000; Kusaka et al., 2001; Wang et al., 2013).

Physically, with shade trees in the street canyon, the rays emitted from a generic canyon facet (road, walls or the sky) are possibly intercepted by tree crowns, which effectively reduces the view factors between all canyon surfaces (the shading effect) (Song and Wang, 2015b). Besides, the location and size of the tree will also influence the view factors. To illustrate, typical view factors from wall to ground (FWG) and wall to wall (FWW) were presented and compared for different horizontal tree locations d_t, tree trunk heights h_t, and tree crown sizes R_t, one in a turn. The canyon dimensions are: wall height x_W = 4.5 m, roof width x_R = 15 m, and road width x_G = 20 m. The results of comparison are shown in Figure 4.2. In Figure 4.2 (a), by keeping tree size as constant (h_t = 2 m, R_t = 2 m) and moving the tree horizontally from the wall, i.e. d_t ranging from 1 m to 3 m, FWG increases while FWW remains nearly constant. The reason is when the tree is farther from a wall, fewer rays emitted from the wall are intercepted by trees and more rays will be received by the ground, thus resulting in larger FWG. On the other hand, FWW represents the average view factor seen by the two opposite-faced walls. As the size of the tree does not change (h_t and R_t are kept as constant), roughly the same number of rays is exchanged between the two walls, leading to roughly constant FWW.

By keeping tree location and tree crown size as constant (d_t = 2 m, R_t = 2 m) and changing the tree trunk height h_t from 1 m to 3 m, it is found that both FWG and FWW will decrease first and then increase with the turning point at 2.5 m (Figure 4.2 b). This non-monotonic pattern is physical, because when h_t is small, the top of the tree crown is lower than the top of the wall (tree crown is completely within the canyon), a taller tree is

more effective in shading the canyon. As h_t increases beyond the limit where tree crown top levels off with the rooftop (in this case h_t = 2.5 m), part of the tree crown is outside the canyon and becomes less effective in shading the canyon facet (part of the shade is casted on roof instead of walls or ground), leading to a slight increase in FWG. Lastly, if the tree location and the tree trunk height are kept as constant (h_t = 2 m, d_t = 2 m), both the FWG and FWW will decrease by increasing the tree crown radius, because more rays can be intercepted by the tree with larger tree crown radius (Figure 4.2 c). With the presence of trees in the street canyon, the view factors between all canyon facets are reduced and the emitted radiative heat received by the canyon facets are decreased, which contributes to the cooling of both walls and ground surfaces.

(a)

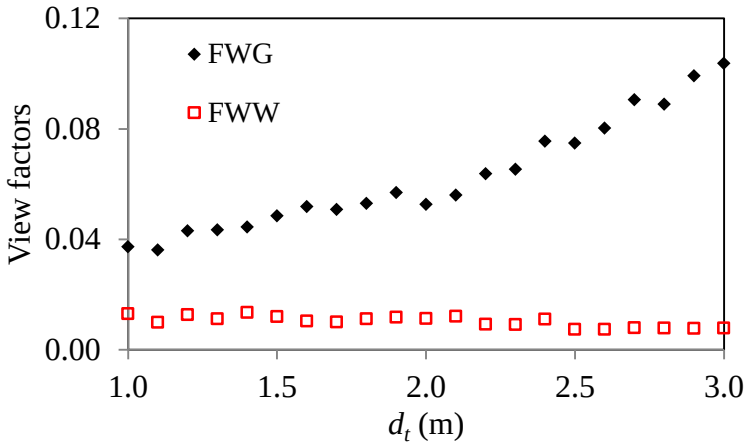

(b)

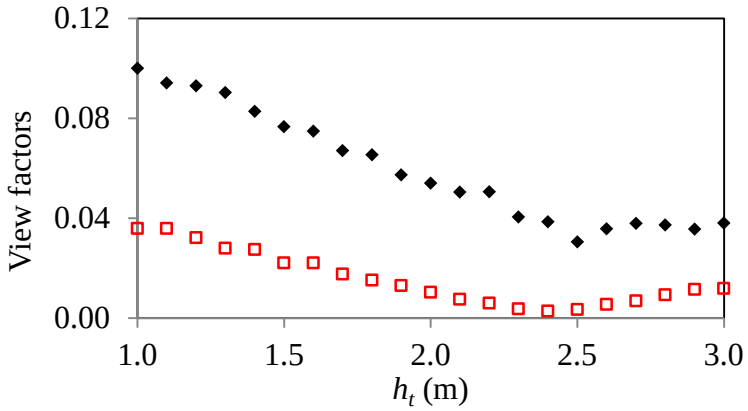

(c)

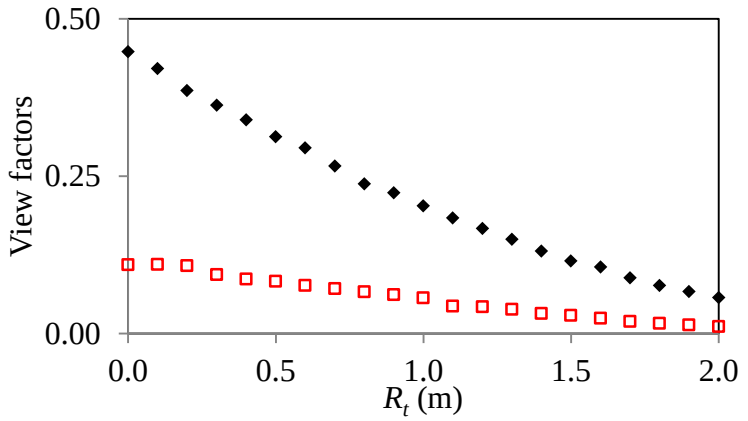

Figure 4.2: Variations of view factors (FWG and FWW) for different (a) tree location d_t, (b) tree trunk height h_t, and (c) tree crown radius R_t.

4.2 Impact of various forms of green infrastructure

In this section, the Phoenix Metropolitan in Arizona State, USA is selected as our testbed. Located in the northeast of the Sonoran Desert, Phoenix is known for its mild winters with mean temperature of 10 °C and hot summers with mean temperature of 32 °C (Baker et al., 2002). This area consists of a wide variety of heterogeneous landscapes, including not only remnant desert and “gray” (buildings, roads, parking lots, etc.) landscapes, but also large green landscapes (mesic lawns, xeric trees, golf courses, urban lakes, etc.) for the sake of amenity, recreation, ecosystem service, stormwater harvesting, and urban heat mitigation (Baker et al., 2002; Foster et al., 2011; EPA, 2013). In particular, there are four common types of residential landscape in Phoenix (see Figure 4.3), including desert (with little or no vegetation, and no irrigation system), xeric vegetation (plants that require drip irrigation systems with low water use, e.g. native desert trees), mesic (non-native plants such as lawns that require sprinkler irrigation systems with high water use), and oasis (a combination of xeric tree and mesic lawn) landscapes (Yabiku et al., 2008).

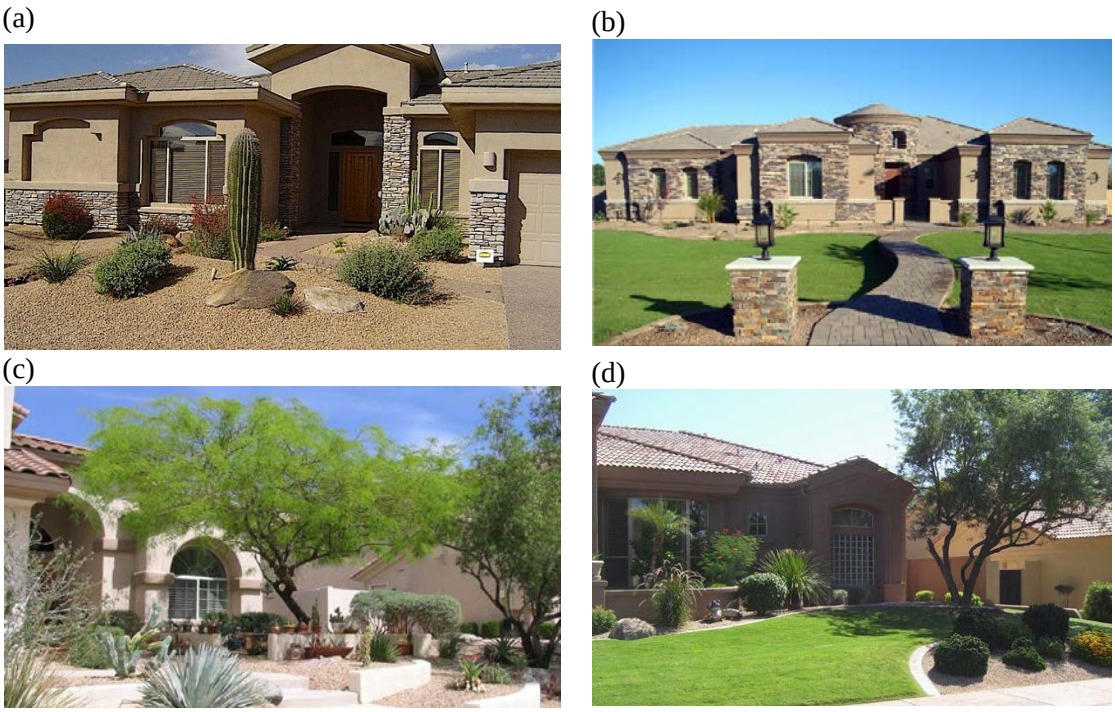

Figure 4.3: Four typical landscapes in Phoenix, Arizona: (a) desert, (b) mesic, (c) xeric, and (d) oasis landscapes.

In the subsequent context, the coupled SLUCM-SCM framework will be applied to simulate different scenarios of green infrastructure in the Phoenix residential area. Summer meteorological conditions with cloud-free sunny days from June 13 to June 30, 2012 were collected from EC Tower site (Table 2.1) to drive the model. The street canyon representation for a typical Phoenix residential area was set with the following dimensions: x_W = 4.5 m, x_R = 15 m, x_G = 20 m, d_t = 2 m, h_t = 2 m (see Fig. 4.1). The model also accounts for the difference in water consumption of different vegetation types: irrigation is not applied for xeric trees; whereas for mesic lawns, the initial soil moisture was set as 90% saturated and the lawn is irrigated at 9 pm (local time) every night in the simulation period to maintain saturated soil moisture in the model so that the cooling efficiency of lawns is not restrained by water availability.

To study the relative impact of different forms of urban green infrastructure, different combinations of green infrastructure forms (i.e. tree, lawn, green roof) are added to the control case. The baseline greening scenario consists of the set of (i) various xeric tree crown radii ranging from 0 m to 1 m with an interval of 0.2 m, (ii) various mesic lawn fraction ranging from 0% to 50% with an interval of 10%, and (iii) various green roof coverage ranging from 0% to 50% areal fraction with an interval of 10%. The range of parameters is determined from practical concerns of deployment of urban green infrastructure in the study area (e.g. EPA 2013, Wang *et al* 2016).

In total, nine combinations of green infrastructure strategies are tested (see Table 4.1), including Scenarios (a), (b), (c) with nominal (as in the baseline scenario) variation of xeric trees and mesic lawns, and 0, 25%, and 50% green roof fraction respectively, Scenarios (d), (e), (f) with nominal variation of urban lawns and green roofs, and tree crown size of 0 m, 0.5 m, and 1 m respectively, and Scenarios (g), (h), (i) with nominal variation of trees and green roofs, and mesic lawns of 0%, 25%, and 50% lawn coverage, respectively. The intercomparison of simulated results of these scenarios is presented in Figures. 4.4-4.7, where the subplot captions are identical to the scenario numbers.

Table 4.1: Description of the nine scenarios of urban greening

Scenario #	Tree crown radius (m)	Lawn fraction (%)	Green roof fraction (%)
a	[0,1]	[0,50]	0
b	[0,1]	[0,50]	25
c	[0,1]	[0,50]	50
d	0	[0,50]	[0,50]
e	0.5	[0,50]	[0,50]
f	1	[0,50]	[0,50]
g	[0,1]	0	[0,50]
h	[0,1]	25	[0,50]
i	[0,1]	50	[0,50]

4.2.1 Boundary-layer temperature

Figure 4.4 and Figure 4.5 show the impact of urban greening on the UBL thermal states, measured in terms of maximum and minimum UBL temperature respectively, averaged from the top of urban canopy layer to the top of UBL. Comparing Figure 4.4 and Figure 4.5 clearly shows that the cooling effect of urban green infrastructure is more significant during daytime than nighttime. Despite the mechanisms of different urban vegetation in re-distributing the surface energy balance (evaporative cooling by lawns and green roofs and radiative shading by xeric trees), the potential cooling effect is constrained by the ultimate energy incident on urban facets. The absence of solar radiation during nighttime therefore ultimately limits the potential cooling effect of all forms of urban mitigation strategies, leading to less surface cooling, which in turn circumscribes the air temperature reduction in the nocturnal UBL.

The first rows, viz. Figure 4.4 and 4.5 (a)-(c) clearly indicate that the cooling effect of green roofs is significant over all different landscapes. For a desert landscape (with no lawn or tree coverage), the maximum UBL temperature $\theta_{v,\max}$ reduces by 1 K

per 25% green roof fraction increment, while the minimum UBL temperature $\theta_{v,\min}$ decreases 0.6 K and 0.4 K, with green roof coverage increased from 0% to 25% and from 25% to 50%. For an oasis landscape (with maximum urban lawns and trees), every 25% increase of roof greening reduces $\theta_{v,\max}$ by 1-1.5 K, and $\theta_{v,\min}$ by 0.6 K. Similarly, for xeric (slighter wetter than desert) and mesic (slighter drier than oasis) landscapes, the same degree of roof greening leads to a similar amount of cooling. The cooling effect of roof greening can also be seen from Figures 4.4 and 4.5 (d)-(i), where the distribution of contours for green roof fractions $f_{v,R}$ is roughly uniform in all these subplots, indicating a relatively uniform UBL cooling rate (0.5 K at daytime and 0.2 K at nighttime) per constant 10% increase of green roof coverage. Similar linear cooling effect of green roof on surface temperature has been reported in earlier studies (e.g. Yang and Wang 2014a). But the current study identifies that uniform cooling by green roofs can "penetrate" from urban surface into the overlying UBL under both stable and unstable conditions.

Unlike green roofs, the cooling effect of urban vegetation in street canyons, viz. mesic lawns and shade trees, is apparently limited by the abundance of total vegetation cover. This can be seen from the change of contour patterns for lawns in Figures 4.4&4.5 (d)-(f), and for trees in Figures 4.4&4.5 (g)-(i), which is more prominent during nighttime. For example, when there is no green roof, greening urban canyons with 50% mesic lawn can effectively reduce $\theta_{v,\max}$ and $\theta_{v,\min}$ by 2.5 K and 1.0 K respectively when no shade tree is present in the canyon (Figures 4.4d and 4.5d), whereas with the presence of shade trees of 1 m crown radii, the cooling effect of the same amount of lawn coverage decreases drastically to around 0.5 K and 0.2 K for $\theta_{v,\max}$ and $\theta_{v,\min}$ respectively (Figures 4.4f and 4.5f). A similar degree of reduced UBL cooling effect is also observed for xeric

landscape with or without the presence of lawns (cf. Figures 4.4&4.5 g with 4.4&4.5 i). This phenomenon of constrained cooling effect in the UBL by urban lawns and trees in street canyons is consistent with that of the surface temperature (Wang et al., 2016), which can be attributed to the competition for available energy by increases in grass richness, tree shading, and nocturnal radiative cooling.

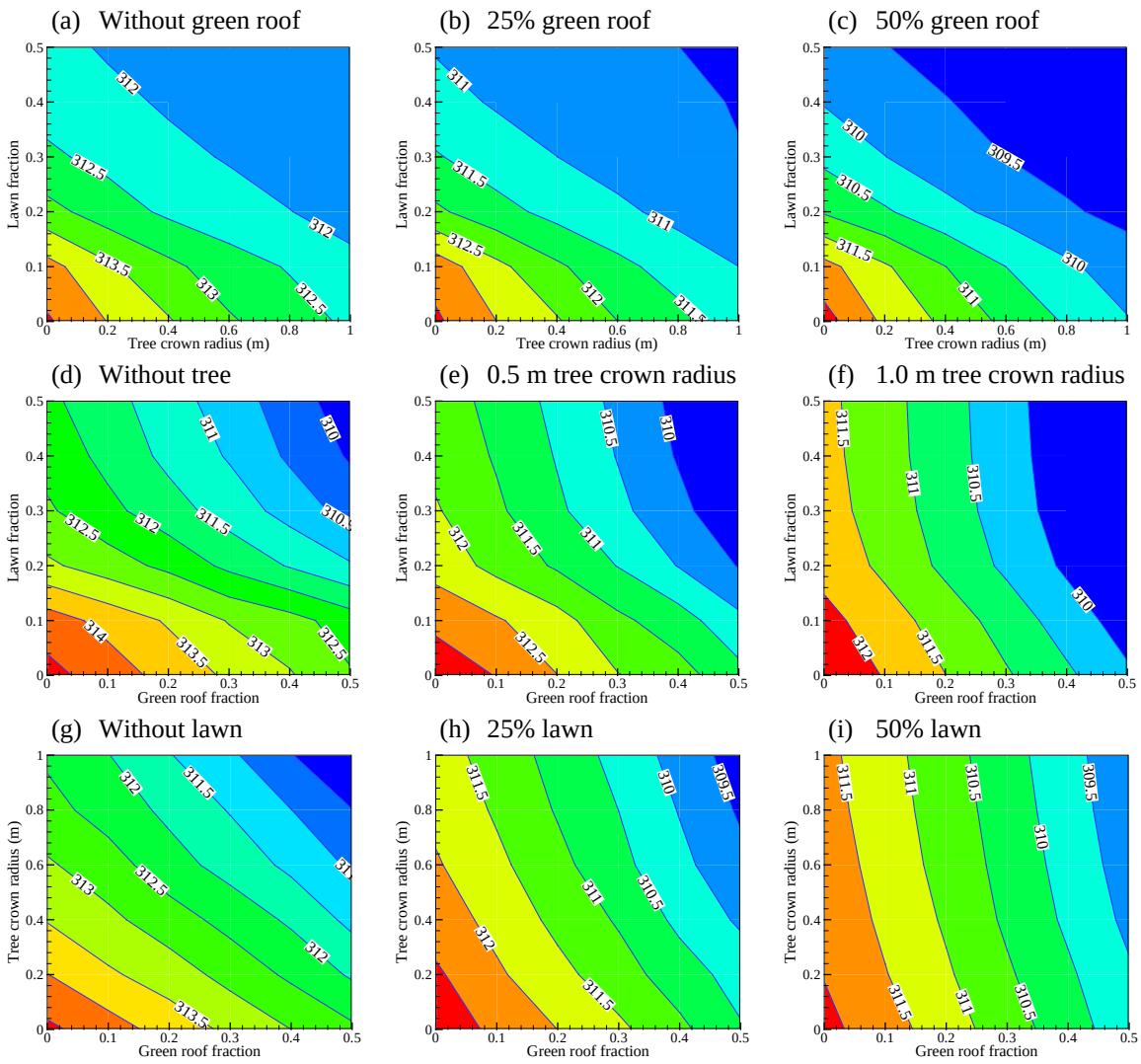

Figure 4.4: Comparison of maximum mean UBL temperature (K) at daytime for different urban greening scenarios: the numbering of subplots corresponds to that of urban greening scenarios. Note that the mean UBL temperature is averaged throughout the mixed layer.

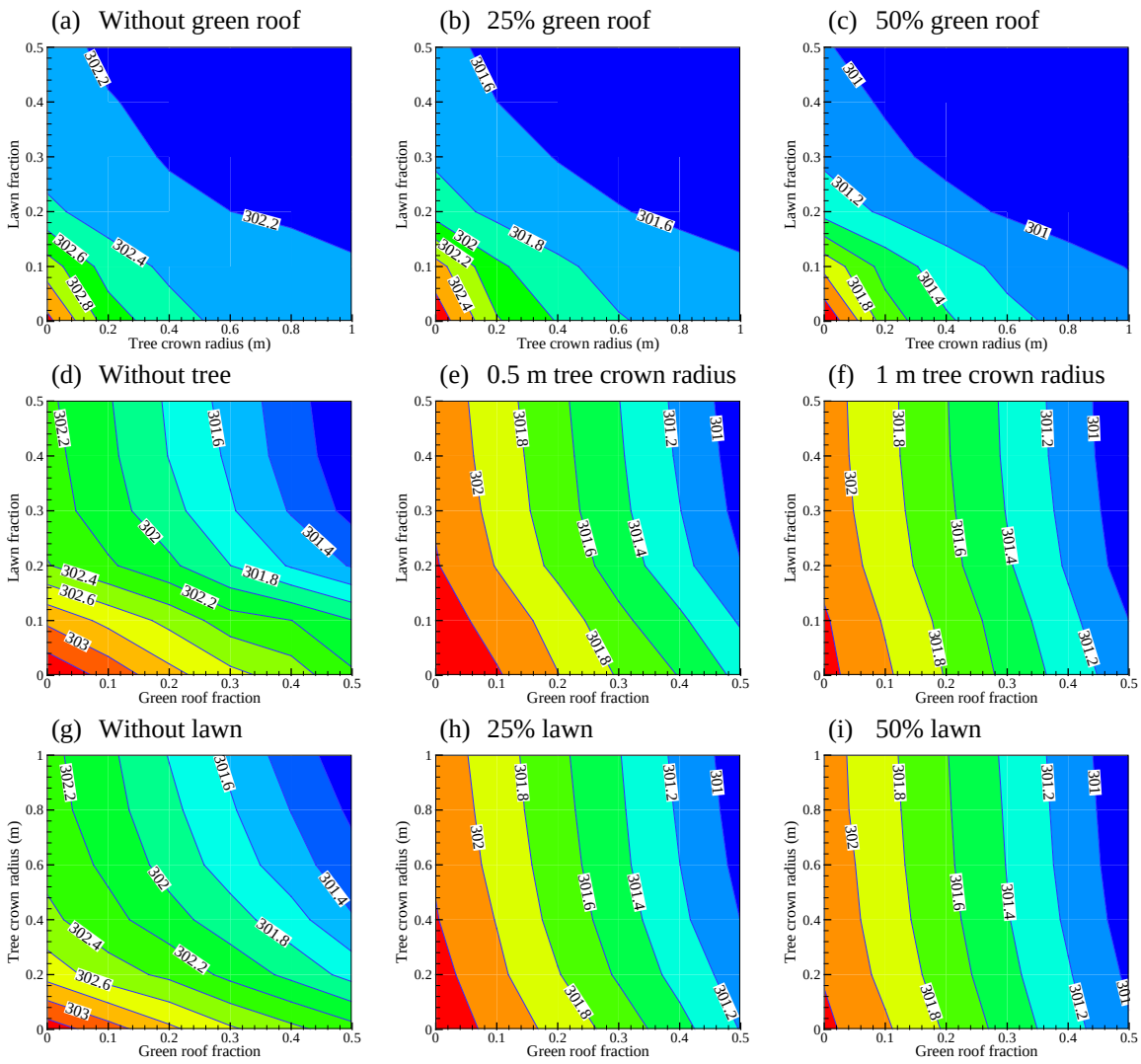

Figure 4.5: As Figure 4.4 but for minimum mean UBL temperature (K)

4.2.2 Boundary-layer height

The impact of urban greening on the evolution of UBL height for convective (daytime) and stable (nocturnal) boundary layers is shown in Figures 4.6 and 4.7, respectively. As the evolution of the UBL height is strongly modulated by the surface thermal state and upwelling (mainly sensible) fluxes (Song and Wang, 2015a), it is expected that patterns of the contour plots in Figures 4.6 and 4.7 follow closely those in Figures 4.6 and 4.7. In general, the overall degree of modification of the UBL height by green infrastructure is greater in daytime than that in nighttime, again attributable to the magnitude of absolute amount of available energy. Furthermore, with increased degree of urban greening, the convective boundary-layer (CBL) height shrinks (Figure 4.6) whereas the stable boundary-layer (SBL) height increases (Figure 4.7). The underlying physics is that urban green infrastructure reduces uprising surface sensible heat flux that is positively related to the CBL height but negatively correlated with the SBL height (Ouwersloot and de Arellano, 2013; Yamada, 1979).

The modification of UBL dynamics by urban greening has strong implications for urban air quality and human health. Firstly, the typical UBL height is ~O (1 km) at daytime, but ~O (100 m) during nighttime. In addition, the daytime boundary layer is highly convective, featuring strong turbulent mixing that favors pollutant dispersion. In contrast, the nocturnal boundary layer is relatively stable and causes accumulation of pollutants (Stull 1988). Due to shallower boundary layer and more stable atmosphere, pollutants, particulate matters, and other scalars produced at the land surface tend to stagnate over a built environment at night, leading to severe degradation of environmental quality. With urban greening, the UBL height decreases at daytime but

increases at nighttime. Pollutant concentration at daytime could be increased due to a shallower boundary layer and weakened vertical mixing (Sharma et al., 2016). However, pollutant concentration at nighttime could be reduced due to a deeper boundary layer. Apart from the indirect influence on improving nocturnal air quality, urban green infrastructure impacts directly on air quality by absorbing the deposition of atmospheric pollutants (Currie and Bass, 2008; Pugh et al., 2012). To accurately quantify the impact of green infrastructure on urban air quality, the coupling of both physical and bio-chemical processes is required and needs interdisciplinary research efforts (Tzoulas et al., 2007; Yang et al., 2008).

In addition, the impact of different urban vegetation on ABL height change varies, similar to their influence on the ABL thermal structure. The effect of green roofs is relatively independent of the urban greening in canyons, and remains effective in modulating both CBL and SBL heights in a relatively uniform rate of increase with green roof coverage. For example, an increase of 50% green roof coverage leads to the reduction of CBL height by 350 m, 350 m, 450 m, and 450 m (Figures 4.6a-c), as well as increase of SBL height by 70 m, 120 m, 130 m, and 130 m (Figures 4.7a-c), over desert, xeric, mesic, and oasis landscapes respectively.

In contrast, urban-greening in the street canyon level is not as effective as green roof systems in a desert city for all landscape types. For example, urban trees of 0.5 m radius can change the CBL height by 300 m (decrease) and the SBL height by 80 m (increase) over a desert landscape (Figures 4.6&4.7, d-e), whiles over an oasis landscape (with 50% lawns), the changes of the CBL and SBL heights by the same trees are reduced to 100 m and 40 m, respectively (Figures 4.6&4.7, e-f). It follows that (i) the

boundary-layer structure is more susceptible to urban trees over desert landscapes than those over oasis landscapes; and (ii) the CBL height is more sensitive to tree crown sizes than the SBL. In street canyons, the shading effect (blockage of direct solar radiation) of trees dominates during daytime, whereas the longwave trapping effect (multiple reflections of diffusive radiation) is overwhelming during nighttime (Wang, 2014). Similar to trees, the effect of urban lawns in regulating UBL heights is also constrained by the overall degree of greening in street canyons, largely resembling their impact on ABL temperatures (see Section 4.2.1). It also follows that adding urban lawns is more effective in regulating ABL height over xeric than mesic landscapes.

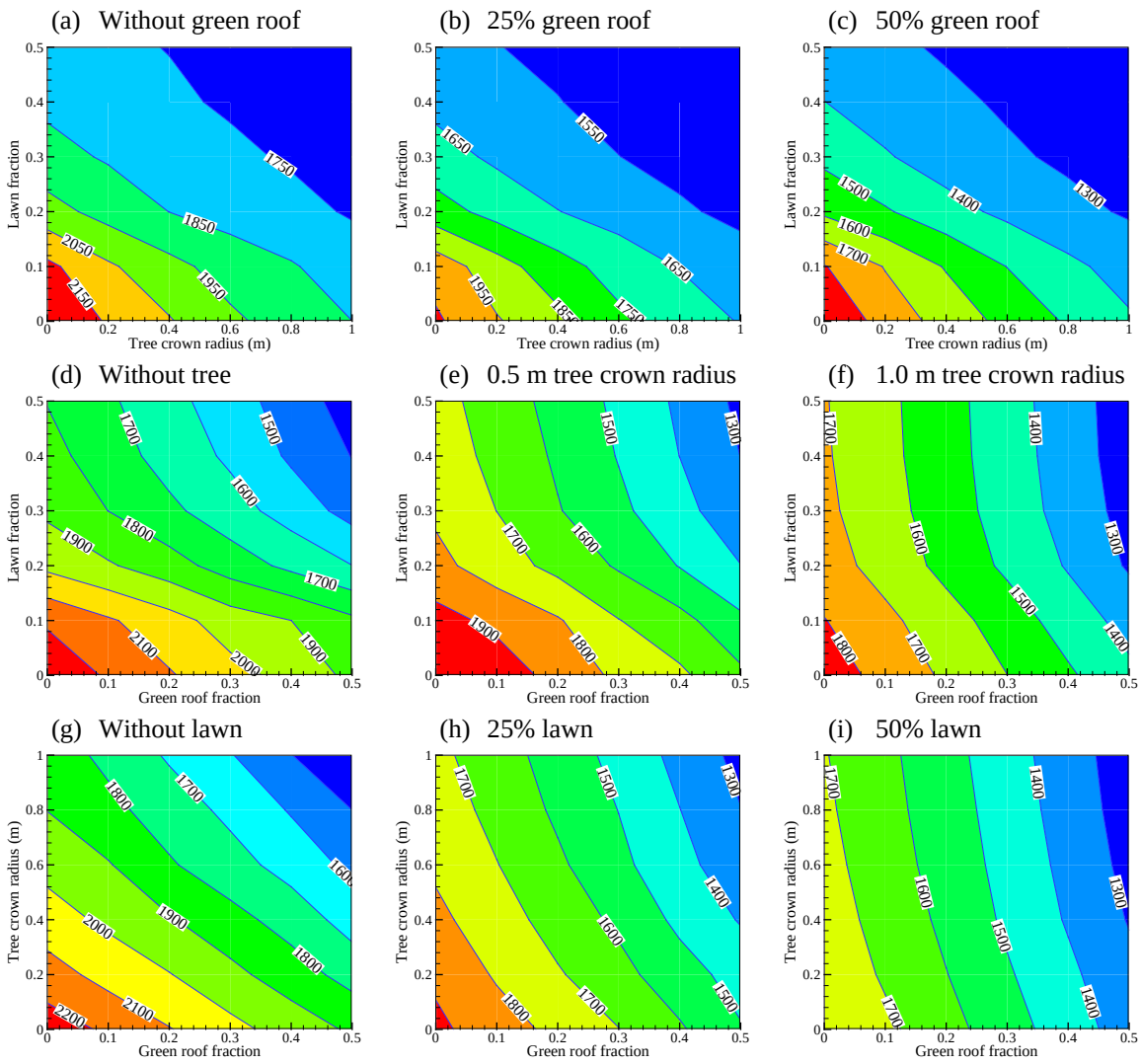

Figure 4.6: As Figure 4.4 but for maximum daytime boundary layer height (m)

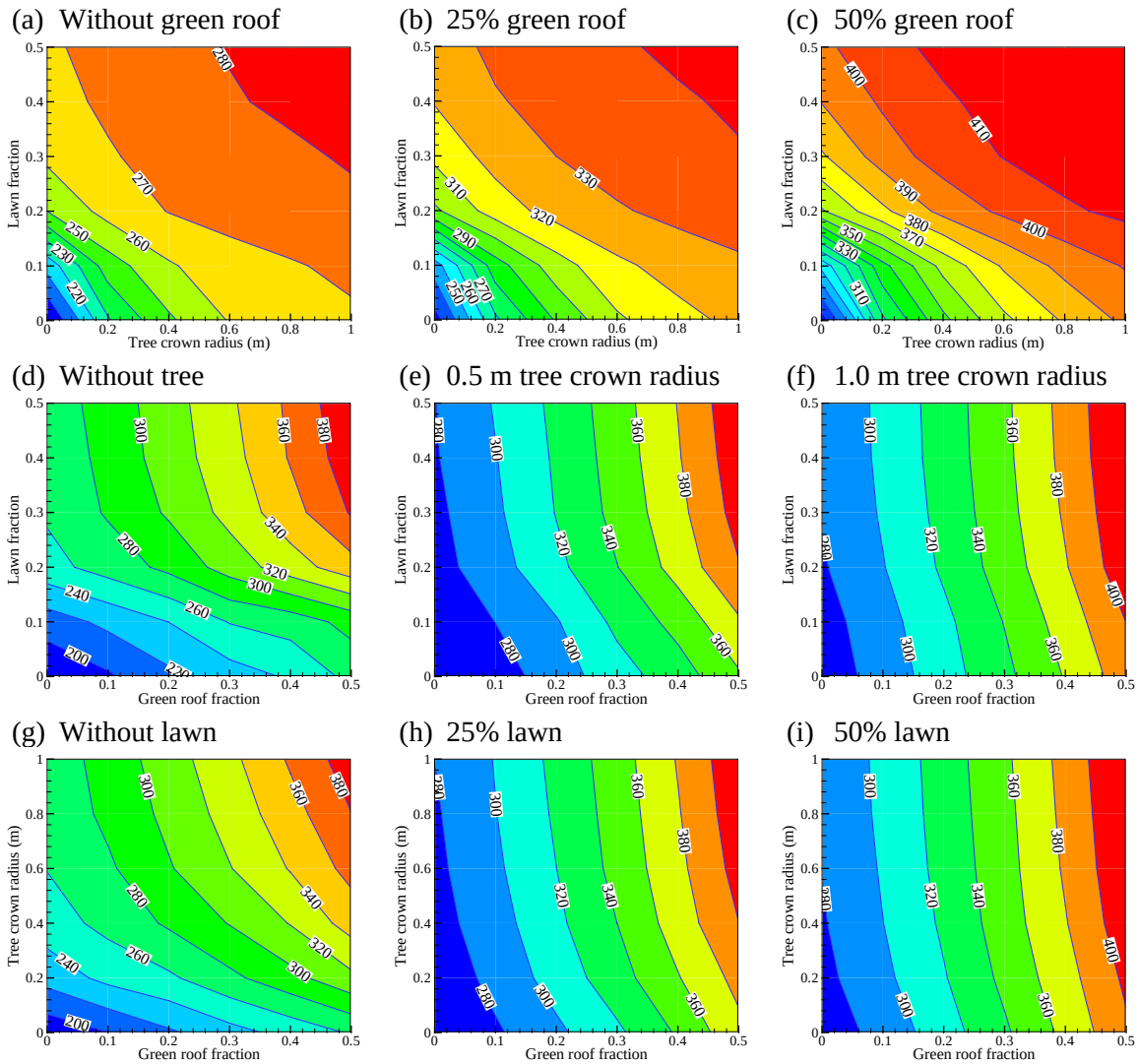

Figure 4.7: As Figure 4.4 but for maximum nighttime boundary layer height (m)

4.3 Summary

This chapter evaluates the impact of urban green infrastructure on urban boundary-layer dynamics over a variety of landscapes using a coupled land-surface-atmosphere modeling framework. In general, the implementation of green infrastructure is found to be effective in regulating the thermal states of the UBL, mainly via the re-partitioning of the urban land surface energy balance and the resulting surface cooling. Constrained by the supply of available energy, the effect of urban greening, specifically

on temperature and boundary-layer height, is more significant on the convective atmospheric layers during daytime than the stable ones. It is also found that the effect of roof cooling, by vegetation or use of reflective materials, is roughly proportional to the degree of roof greening (viz. the areal fraction of coverage), and remains effective despite the presence of urban vegetation in street canyons. However, vegetated roof has a greater cooling capacity than reflective roof especially at nighttime. Specifically, the coverage of 90% vegetated roof lead to additional ~1 K than the reflective roof. On the other hand, the cooling effect of urban lawns and shade trees depends on the initial state of urban greening and the overall abundance of green infrastructure in the neighborhood. The marginal effect of increasing urban lawns and trees diminishes with the total vegetation coverage as well as the soil moisture state (i.e. they are more effective over desert/xeric than mesic/oasis landscapes). With the presence of big trees (such as with tree crown radius of 1 m), the cooling effect of added lawn will be significantly restrained. It is noteworthy that with little demand of water via the drip irrigation system, shade trees over xeric landscapes present a promising urban mitigation strategy as an alternative to more traditional water-demanding urban lawns. This is particularly attractive to house-owners and city planners in an arid or semi-arid environment like Phoenix. Moreover, note that the modeling framework used in this study resolves the vertical transport processes of heat and scalars in the soil-surface-atmosphere continuum. As our focus is on alleviating surface- and boundary-layer thermal stress using green infrastructure, this model setting helps to single out the impact of landscape modification and is representative of calm and clear weather conditions with a UBL dominated by free convection; these conditions are particularly relevant for our study of a desert valley city.

CHAPTER 5 SUMMARY AND FUTURE PERSPECTIVES

5.1 Summary

This dissertation presents a comprehensive effort focused on the development of a novel modeling framework of urban land-atmosphere interactions and its implications to urban environment. A new urban land-atmosphere coupling framework, viz. SLUCM-SCM is developed for modelling the urban land-atmosphere interactions in this study, with the SLUCM enabling the realistic representation of urban geometry and green infrastructure and the SCM capturing both convective and stable boundary layer dynamics. The model is test against field measurements over multiple locations for the energy budgets in the urban canopy layer such as net radiation and sensible and latent heat fluxes, as well as ABL dynamics including profiles of temperature and humidity and the evolution of ABL height. The validated model framework is used to study the impact of urban land surface characteristics, including urban geometry, albedo, vegetation fraction and aerodynamic roughness on the growth of the ABL and the distributions of temperature and humidity in the mixed layer under convective conditions. Since model performances largely depend on the accuracy of input parameters, to quantify the model sensitivity to the input model parameters, an advanced Monte Carlo method, i.e. Subset Simulation was adopted to quantify the sensitivity of ABL dynamics to urban land surface changes based on the SLUCM-SCM framework.

Results of case studies and sensitivity analyses show that changes in land-surface properties (hydrothermal or geometric) have a significant impact on the evolution of the overlying boundary layer. In particular, the urban street canyon geometry, represented by the canyon-aspect ratio h/w, imposes non-linear effects on the ABL responses (z_h growth

and θ_v distribution in the mixed layer), through rather complex interactions of the opposing radiative trapping and shading effects co-evolving throughout the daytime. It is also found that widely-used urban planning strategies such as the implementation of cool and green roofs as well as modification of the vertical turbulent transfer through enhanced aerodynamic conductance, are effective in affecting the transport of momentum, heat and moisture in the urban boundary layers.

In particular, the impact of urban green infrastructure on urban boundary layer dynamics is assessed. The implementation of green infrastructure (such as shade trees, lawns and green roofs) is effective in regulating the UBL dynamics (specifically UBL temperature and height) via the re-partitioning of the urban land surface available energy into more latent heat flux and less sensible heat flux. The effect of urban greening is more significant at daytime than at nighttime due to the difference of total available energy. Besides, the cooling effect of roof greening is relatively independent from that of street greening. However, the cooling effect of implementing additional street green infrastructure (i.e. urban lawns and shade trees) is more effective over desert/xeric than mesic/oasis landscapes. Besides, shade trees over xeric landscapes with little water demand present a promising urban mitigation strategy as an alternative to more traditional water-demanding urban lawns, which could be particularly attractive to house-owners and city planners in an arid or semi-arid environment like Phoenix.

5.2 Future perspectives

The current SLUCM-SCM framework only resolves the typical daytime (convective) and nighttime (stable) schemes for the urban boundary layer. The inclusion of early morning and early evening transitions for boundary layer schemes over urban

surfaces will be of significant importance to complete the diurnal cycle physically and to resolve air quality issues at the transitional periods (Wildmann et al., 2015; Sastre et al., 2015). The early morning transition from a SBL to a CBL can be divided into two phases (Stull 1988): (1) warming of land surface enables the growth of a shallow CBL below the remaining nighttime inversion layer, and (2) thermals rise through the whole ABL so that the top of CBL reaches the bottom of remaining inversion layer, forming the fully developed CBL. The early evening transition from a CBL to a SBL is induced by radiative cooling at the ground surface and can be divided into several phases including the sunset, the reversal of surface heat flux, and the establishment of a SBL. Measurements of transition periods are often conducted via remotely-piloted aircrafts with complementary instruments such as scintillometers and sonic anemometers. The vertical profiles of turbulent surface heat fluxes can be simulated via inverse models and large eddy simulations (LES), but simulating moisture flux remains a challenge (Bange et al., 2006).

Secondly, more realistic representations of urban green infrastructure can be incorporated to better resolve the balance and transport of urban surface energy, water and carbon budgets (Bowling et al., 2010). For example, more detailed dynamics, root-soil physics and irrigation schemes should be considered when parameterizing mesic vegetation such as lawn and green roof. Besides, the model framework should take into account more practical concerns of green roof implementation above variable rooftop constructions (e.g. flat vs. sloped). More green roof parameters such as the roof slope, vegetation diversity, vegetation albedo, irrigation schedules, etc. could be added into the current model framework. Moreover, the tree parameterization in the current model is

limited to xeric tree (which has little water demand and small evapotranspiration potential) by only considering the effect on modifying radiative exchange processes. In the future, tree parameterization schemes could be improved in several ways, including (1) adding more realistic evapotranspiration schemes for trees so that the effect of mesic trees can be better resolved; (2) adding other physical parameters of trees such as tree species, tree crown shapes, leaf albedo, etc.

In addition, by incorporating the realistic biological effect of vegetation and soil as well as anthropogenic effect (such as the inventory of anthropogenic emissions from vehicular traffic, human metabolism, electricity consumption, heating fuels, etc.) (Sailor and Lu, 2004), atmospheric dynamics of temperature, carbon and greenhouse gases in urban areas can be better resolved (Song and Wang, 2016b). In particular, by coupling the current model framework with bio-chemical schemes such as a big-leaf dry deposition model (Yang et al., 2008) which incorporates the dynamics of reactive scalars (such as O_3, SO_2, etc.), the impact of urban green infrastructure on air pollution issues can be better explored. Specifically, both the direct impact of vegetation in absorbing air pollutants and the indirect impact of vegetation in regulating the UBL height can be resolved.

It is also noteworthy that the current modeling framework is limited by its inadequacy in capturing the horizontal advection and synoptic wind shear effects. In addition, since it is tested in the one-way (bottom-top) offline (stand-alone) setting, the current numerical framework does not have predictive skills, without projections of future atmospheric forcing. Thus it is of critical importance to run the model in an *online* setting (with two-way coupling including bottom-up and up-bottom feedbacks), e.g. by

incorporating the framework into a mesoscale numerical weather prediction model such as the WRF model, which remains our future work. This way, the proposed numerical framework can be driven by meteorological forcing from numerical predictions at regional scales and become predictive for scenarios of city-scale land-atmosphere interactions downscaled from future climatic projections. With land-surface processes represented by the latest SLUCM, online simulations using the coupled framework should help to provide important guidelines for future development of cities with sustainable urban planning, e.g. UHI mitigation and adaptation strategies.

REFERENCES

Akbari H, Matthews H D and Seto D 2012 The long-term effect of increasing the albedo of urban areas *Environ. Res. Lett.* **7** 024004

Alexandri E and Jones P 2008 Temperature decreases in an urban canyon due to green walls and green roofs in diverse climates *Build. Environ.* **43** 480–93

Ali-Toudert F and Mayer H 2006 Numerical study on the effects of aspect ratio and orientation of an urban street canyon on outdoor thermal comfort in hot and dry climate *Build. Environ.* **41** 94-108

Atmospheric Radiation Measurement (ARM) Program (2011) Balloon-borne sounding system (SONDE), sondewnpn b1 data stream, Available from ARM Archive, Oak Ridge, Tennessee, U.S.A. Data subset: Oct 2010 - Mar 2011, 36° 36' 18.0" N, 97° 29' 6.0" W

Au S-K and Beck J L 2001 Estimation of small failure probabilities in high dimensions by subset simulation *Probabilist. Eng. Mech.* **16** 263-277

Au S-K, Wang Z-H and Lo S-M 2007 Compartment fire risk analysis by advanced Monte Carlo simulation *Eng. Struct.* **29** 2381-2390

Au S-K and Wang Y 2014 Engineering Risk Assessment with Subset Simulation, 336pp, Wiley, Singapore.

Arnfield A J 2003 Two decades of urban climate research: A review of turbulence, exchanges of energy and water, and the urban heat island *Int. J. Climatol*. **23** 1-26

Baker L A, Brazel A J, Selover N, Martin C, McIntyre N, Steiner F R, Nelson A and Musacchio L 2002 Urbanization and warming of Phoenix (Arizona, USA): Impacts, feedbacks and mitigation. *Urban Ecosys.* **6** 183-203

Bange J, Zittel P, Spieß T, Uhlenbrock J and Beyrich F 2006 A new method for the determination of area-averaged turbulent surface fluxes from low-level flights using inverse models *Boundary-layer meteorol.* **119** 527-561

Bellman R and Rand C 1957 Dynamic programming, 140pp, Princeton University Press, Princeton, New Jersey.

Betts A K, Ball J H, Beljaars A C M, Miller M J and Viterbo P A 1996 The land surface-atmosphere interaction: A review based on observational and global modeling perspectives *J. Geophys. Res. - Atmos.* **101** 7209-7225

Blocken B 2015 Computational Fluid Dynamics for Urban Physics: Importance, scales, possibilities, limitations and ten tips and tricks towards accurate and reliable simulations *Build Environ.* **91** 219-245

Bowler D E, Buyung-Ali L, Knight T M and Pullin A S 2010 Urban greening to cool towns and cities: A systematic review of the empirical evidence *Lands. Urban Plan.* **97** 147–55

Bowling D R, Bethers-Marchetti S, Lunch C K, Grote E E and Belnap J 2010 Carbon, water, and energy fluxes in a semiarid cold desert grassland during and following multiyear drought *J. Geophys. Res.: Biogeosci.* **115** G04026

Bonan G B, Oleson K W, Vertenstein M, Levis S, Zeng X B, Dai Y J, Dickinson R E and Yang Z L 2002 The land surface climatology of the community land model coupled to the NCAR community climate model. J. Climate **15** 3123-3149

Businger J A, Wyngaard J C and Bradley E F 1971. Flux-profile relationships in the atmospheric surface layer. J. Atmos. Sci. **28** 181-189.

Brutsaert W 2005 *Hydrology: An Introduction* Cambridge University Press 605 pp

Chen F, Avissar R 1994 Impact of land-surface moisture variability on local shallow convective cumulus and precipitation in large-scale models. J. Appl. Meteorol. **33** 1382-1401

Chen F, Dudhia J 2001 Coupling an advanced land surface–hydrology model with the Penn State–NCAR MM5 modeling system. Part I: Model implementation and sensitivity. Mon. Weather Rev. **129** 569-585.

Chen F, Kusaka H, Bornstein R, Ching J, Grimmond C S B, Grossman-Clarke S, Loridan T, Manning K W, Martilli A, Miao S, Sailor D, Salamanca F P, Taha H, Tewari M, Wang X, Wyszogrodzki A A, and Zhang C 2011. The integrated WRF/urban modelling system: development, evaluation, and applications to urban environmental problems *Int. J. Climatol.* **31** 273-88

Chen F and Avissar R 1994 Impact of land-surface moisture variability on local shallow convective cumulus and precipitation in large-scale models *J. Appl. Meteorol.* **33** 1382-1401

Chen F and Dudhia J 2001 Coupling an advanced land surface–hydrology model with the Penn State – NCAR MM5 modeling system. Part I: Model implementation and sensitivity *Mon. Weather Rev.* **129** 569-585

Cherchi E and Guevara C A 2012 A Monte Carlo experiment to analyze the curse of dimensionality in estimating random coefficients models with a full variance–covariance matrix *Transport Res. B-Meth.* **46** 321-332

Chow W T and Brazel A J 2012 Assessing xeriscaping as a sustainable heat island mitigation approach for a desert city *Build. Environ.* **47** 170–81

Chow W T, Volo T J, Vivoni E R, Jenerette G D and Ruddell B L 2014 Seasonal dynamics of a suburban energy balance in Phoenix, Arizona *Int. J. Climatol.* **34** 3863–80

Clarke R H, Dyer A J and Scientific C 1971 The Wangara experiment: Boundary layer data (CSIRO Australia)

Cohen A E, Cavallo S M, Coniglio M C and Brooks H E 2015 A Review of Planetary Boundary Layer Parameterization Schemes and Their Sensitivity in Simulating Southeastern US Cold Season Severe Weather Environments *Weather Forecast* **30** 591-612.

Collier C G 2006 The impact of urban areas on weather. Q. J. R. Meteorol. Soc. **132** 1-25

Cuenca R H, Ek M and Mahrt L 1996 Impact of soil water property parameterization on atmospheric boundary layer simulation *J. Geophys. Res. Atmos.* **101** 7269-7277

Currie B A and Bass B 2008 Estimates of air pollution mitigation with green plants and green roofs using the UFORE model *Urban Ecosys.* **11** 409-422

de Vrese P, Hagemann S, Claussen M 2016 Asian irrigation, African rain: Remote impacts of irrigation *Geophys. Res. Lett.* **43** 3737-45

Deardorff J W 1980 Stratocumulus-capped mixed layers derived from a three-dimensional model. *Boundary-Layer Meteorol.* **18** 495-527

Dimitrova R, Silver Z, Fernando H J, Leo L, Di Sabatino S, Hocut C, Zsedrovits T 2014 Inter-comparison between different PBL options in WRF model. Modification of two PBL schemes for stable conditions In *94th AMS Annual Meeting*, Atlanta, GA.

Dupont S, Otte T L, Ching J K S 2004 Simulation of meteorological fields within and above urban and rural canopies with a mesoscale model (mm5). *Boundary-Layer Meteorol.* **113** 111-158

Dvorak B, Volder A 2010 Green roof vegetation for north American ecoregions: A literature review. *Landscape Urban Plan* **96** 197-213

Eltahir E A B 1998 A soil moisture-rainfall feedback mechanism. 1. Theory and observations. *Water Resour. Res.* **34** 765-776

EPA 2013 Green infrastructure barriers and opportunities in Phoenix, Arizona – An evaluation of local codes and ordinances

Flagg D D and Taylor P A 2011 Sensitivity of mesoscale model urban boundary layer meteorology to the scale of urban representation *Atmos. Chem. Phys.* 11 2951-2972

Fischer E M, Seneviratne S I, Lüthi D and Schär C 2007 Contribution of land-atmosphere coupling to recent European summer heat waves *Geophys. Res. Lett.* **34** L06707

Foken T 2008 The energy balance closure problem: An overview *Ecol. Appl.* **18** 1351-1367

Foster J, Lowe A, and Winkelman S 2011 The value of green infrastructure for urban climate adaptation. Center for Clean Air Policy

Garratt J R and Brost R A 1981 Radiative cooling effects within and above the nocturnal boundary layer. *J. Atmos. Sci*. **38** 2730-2746

Georgescu M, Mahalov A, and Moustaoui M 2012 Seasonal hydroclimatic impacts of Sun Corridor expansion. *Environ. Res. Lett.,* **7** 034026

Georgescu M, Morefield P E, Bierwagen B G and Weaver C P 2014 Urban adaptation can roll back warming of emerging megapolitan regions *Proc. Natl. Acad. Sci.* **111** 2909–14

Gill S, Handley J, Ennos A and Pauleit S 2007 Adapting cities for climate change: the role of the green infrastructure *Built Environ.* **33** 115–33

Gober P, Brazel A, Quay R, Myint S, Grossman-Clarke S, Miller A and Rossi S 2009 Using watered landscapes to manipulate urban heat island effects: how much water will it take to cool Phoenix? *J. Am. Plann. Assoc.* **76** 109-121

Grimmond C S B, Blackett M, Best M, Baik J J, Belcher S, Bohnenstengel S I, Calmet I, Chen F, Dandou A, Fortuniak K and Gouvea M 2009 The International Urban Energy Balance Comparison Project: Initial Results from Phase 2. In *The 7th International Conference on Urban Climate ICUC-7, Yokohama, Japan* (Vol. 29).

Grimmond C S B, Coutts A, Dandou A, Fortuniak K, Gouvea M L, Hamdi R, Hendry M, Kanda M, Kawai T, Kawamoto Y, Kondo H, Blackett M, Krayenhoff E S, Lee S H, Loridan T, Martilli A, Masson V, Miao S, Oleson K, Ooka R, Pigeon G, Porson A, Best M J, Ryu Y H, Salamanca F, Steeneveld G J, Tombrou M, Voogt J A, Young D T, Zhang N, Baik J J, Belcher S E, Beringer J, Bohnenstengel S I, Calmet I and Chen F 2011 Initial results from phase 2 of the international urban energy balance model comparison. *Int. J. Climatol.* **31** 244-272

Grimmond C S B, Dandou A, Fortuniak K, Gouvea M L, Hamdi R, Hendry M, Kawai T, Kawamoto Y, Kondo H, Krayenhoff E S, Lee S H, Blackett M, Loridan T, Martilli A, Masson V, Miao S, Oleson K, Pigeon G, Porson A, Ryu Y H, Salamanca F, Shashua-Bar L, Best M J, Steeneveld G J, Tombrou M, Voogt J, Young D, Zhang N, Barlow J, Baik J

J, Belcher S E, Bohnenstengel S I, Calmet I and Chen F 2010 The international urban energy balance models comparison project: First results from phase 1. *J. Appl. Meteorol. Climatol.* **49** 1268-1292

Grimmond C S B and Oke T R 1999 Aerodynamic properties of urban areas derived, from analysis of surface form *J. Appl. Meteorol.* **38** 1262-1292

Gutiérrez E, González J E, Martilli A, Bornstein R and Arend M 2015a Simulations of a heat-wave event in New York City using a multilayer urban parameterization *J. Appl. Meteor. Climatol.* **54** 283-301

Gutiérrez E, Martilli A, Santiago J L, and González J E 2015b A mechanical drag coefficient formulation and urban canopy parameter assimilation technique for complex urban environments *Boundary-Layer Meteorol.* **157** 333-41

Hargreaves J C 2010 Skill and uncertainty in climate models *Wiley Interdiscip. Rev. Clim. Change*. **1** 556-64

Higgins C W 2012 A-posteriori analysis of surface energy budget closure to determine missed energy pathways *Geophys. Res. Lett.* **39** L19403

Holdridge D, Ritsche M, Prell J and Coulter R 2011 Balloon-Borne Sounding System (SONDE) Handbook

Holtslag A A M and Moeng C H 1991 Eddy diffusivity and countergradient transport in the convective atmospheric boundary-layer *J. Atmos. Sci.* **48** 1690-1698

Hong S Y, Noh Y and Dudhia J 2006 A new vertical diffusion package with an explicit treatment of entrainment processes *Mon. Weather Rev.* **134** 2318-2341

Hong S Y and Pan H L 1996 Nonlocal boundary layer vertical diffusion in a medium-range forecast model *Mon. Weather Rev.* **124** 2322-2339

Hong S 2010 A new stable boundary-layer mixing scheme and its impact on the simulated East Asian summer monsoon *Q. J. R. Meteorol. Soc.* **136** 1481–96

Howell J R 1968 Application of Monte Carlo to heat transfer problems *Adv. Heat Transf.* **5** 1–54

Jacobson M Z and Ten Hoeve J E 2012 Effects of urban surfaces and white roofs on global and regional climate. *J. Climate* **25** 1028-1044

Janjic Z I 1994 The step-mountain eta coordinate model: Further developments of the convection, viscous sublayer, and turbulence closure schemes. *Mon. Wea. Rev.* **122** 927-945

Jeričević A and Grisogono B 2006 The critical bulk Richardson number in urban areas: Verification and application in a numerical weather prediction model. *Tellus* **58** 19-27

Kikegawa Y, Genchi Y, Yoshikado H and Kondo H 2003 Development of a numerical simulation system toward comprehensive assessments of urban warming countermeasures including their impacts upon the urban buildings' energy-demands *Appl. Energ.* **76** 449-466

Kim J J and Baik J J 2004 A numerical study of the effects of ambient wind direction on flow and dispersion in urban street canyons using the RNG k–ε turbulence model *Atmos. Environ.* **38** 3039-3048

Kim S W, Park S U, Pino D and Arellano J G 2006 Parameterization of entrainment in a sheared convective boundary layer using a first-order jump model. *Boundary-Layer Meteorol.* **120** 455-475

Kondo H, Genchi Y, Kikegawa Y, Ohashi Y, Yoshikado H and Komiyama H 2005 Development of a multi-layer urban canopy model for the analysis of energy consumption in a big city: Structure of the urban canopy model and its basic performance. *Boundary-Layer Meteorol.* **116** 395-421

Koster R D, Dirmeyer P A, Guo Z, Bonan G, Chan E, Cox P, Gordon C T, Kanae S, Kowalczyk E, Lawrence D and Liu P 2004 Regions of strong coupling between soil moisture and precipitation *Science* **305** 1138-1140

Krayenhoff E S, Christen A, Martilli A and Oke T R 2014 A multi-layer radiation model for urban neighbourhoods with trees. *Boundary-Layer Meteorol.* **151** 139-178

Kusaka H, Kondo H, Kikegawa Y and Kimura F 2001 A simple single-layer urban canopy model for atmospheric models: Comparison with multi-layer and slab models *Boundary-Layer Meteorol.* **101** 329–58

Krüger E L, Minella F O and Rasia F 2011 Impact of urban geometry on outdoor thermal comfort and air quality from field measurements in Curitiba, Brazil *Build. Environ.* **46** 621-634

Li D, Bou-Zeid E and Oppenheimer M 2014 The effectiveness of cool and green roofs as urban heat island mitigation strategies *Environ. Res. Lett.* 9 055002

Li F, Wang R, Paulussen J and Liu X 2005 Comprehensive concept planning of urban greening based on ecological principles: a case study in Beijing, China *Lands. Urban Plan.* **72** 325–36

Loridan T, Grimmond C S B, Grossman-Clarke S, Chen F, Tewari M, Manning K, Martilli A, Kusaka H and Best M 2010 Trade-offs and responsiveness of the single-layer urban canopy parametrization in WRF: An offline evaluation using the MOSCEM optimization algorithm and field observations *Q. J. R. Meteorol. Soc.* **136** 997-1019

Maslin M. and Austin P 2012 Uncertainty: Climate models at their limit? *Nature* **486** 183-184

Masson V 2000 A physically-based scheme for the urban energy budget in atmospheric models *Boundary-Layer Meteorol.* **94** 357–97

Martilli A, Clappier A and Rotach M 2002 An urban surface exchange parameterisation for mesoscale models *Boundary-Layer Meteorol.* **104** 261-304

Mascart P, Noilhan J and Giordani H 1995 A modified parameterization of flux-profile relationships in the surface-layer using different roughness length values for heat and momentum *Boundary-Layer Meteorol.* **72** 331-344

McCumber M C and Pielke R A 1981 Simulation of the effects of surface fluxes of heat and moisture in a mesoscale numerical model 1 *Soil layer*, *J. Geophys. Res.* **86** 9929-9938

Meehl G A and Tebaldi C 2004 More intense, more frequent, and longer lasting heat waves in the 21st century *Science* **305** 994-997

Nakanishi M and Niino H 2006 An improved Mellor–Yamada level-3 model: Its numerical stability and application to a regional prediction of advection fog. *Boundary-Layer Meteorol.* **119** 397-407

Nakanishi M and Niino H 2009 Development of an improved turbulence closure model for the atmospheric boundary layer *J. Meteor. Soc. Japan* **87** 895-912

Niyogi D, Mahmood R and Adegoke J O 2009 Land-use/land-cover change and its impacts on weather and climate *Boundary-Layer Meteorol.* **133** 297-298

Niyogi DS, Raman S 1997 Comparison of four different stomatal resistance schemes using FIFE observations. *J. Appl. Meteorol.* **36** 903-917

Noh Y, Cheon W, Hong S and Raasch S 2003 Improvement of the K-profile model for the planetary boundary layer based on large eddy simulation data *Boundary-Layer Meteorol.* **107** 401–27

Noihan J, Planton S 1989 A simple parameterization of land surface processes for meteorological models. *Mon. Weather Rev.* **117** 536-549

Nunez M and Oke T R 1977 The energy balance of an urban canyon *J. Appl. Meteorol.* **16** 11-19

Oke T R 1973 City size and the urban heat island *Atmospheric Environ. 1967* **7** 769–79

Oke T R 1976 The distinction between canopy and boundary-layer urban heat islands Atmosphere **14** 268-277

Oke T R 1982 The energetic basis of the urban heat island, Q. J. R. Meteorol. Soc., 108, 1-24

Oke T R 1988 The urban energy balance. *Prog. Phys. Geogr.* **12** 471-508

Oliveira S, Andrade H and Vaz T 2011 The cooling effect of green spaces as a contribution to the mitigation of urban heat: A case study in Lisbon *Build. Environ.* **46** 2186-2194

Orlowsky B and Seneviratne S I 201Statistical analyses of land-atmosphere feedbacks and their possible pitfalls *J. Climate* **23** 3918-3932

Ouwersloot H and de Arellano J V-G 2013 Analytical solution for the convectively-mixed atmospheric boundary layer *Boundary-Layer Meteorol.* **148** 557–83

Ramamurthy P, Bou-Zeid E, Smith J A, Wang Z, Baeck M L, Saliendra N Z, Hom J L and Welty C 2014 Influence of sub-facet heterogeneity and material properties on the urban surface energy budget *J. Appl. Meteorol. Climatol.* **53** 2114-2129

Ryu Y H, Baik J J and Lee S H 2011 A new single-layer urban canopy model for use in mesoscale atmospheric models *J. Appl. Meteorol.* **50** 1773-1794

Pagowski M 2004 Some comments on PBL parameterizations in WRF. In *The Joint WRF/MM5 Users' Workshop, Boulder, CO* (Vol. 1, No. 9).

Pérez G, Rincón L, Vila A, González J M and Cabeza L F 2011 Green vertical systems for buildings as passive systems for energy savings *Appl. Energy* **88** 4854–9

Phillips T J and Klein S A 2014 Land-atmosphere coupling manifested in warm-season observations on the U.S. Southern great plains *J. Geophys. Res. - Atmos.* 119 2013JD020492

Piringer M, Grimmond C S B, Joffre S M, Mestayer P, Middleton D R, Rotach M W, Baklanov A, De Ridder K, Ferreira J, Guilloteau E and Karppinen A 2002 Investigating the surface energy balance in urban areas–recent advances and future needs *Water Air Soil Pollut. Focus,* **2** 1-16

Pugh T A, MacKenzie A R, Whyatt J D and Hewitt C N 2012 Effectiveness of green infrastructure for improvement of air quality in urban street canyons. *Environ. Sci. Technol.* **46** 7692-7699

Sailor D J and Lu L 2004 A top–down methodology for developing diurnal and seasonal anthropogenic heating profiles for urban areas *Atmos. Environ.* **38** 2737-2748

Sailor D J 2008 A green roof model for building energy simulation programs *Energ. Buildings* **40** 1466-1478

Sailor D J, Elley T B and Gibson M 2012 Exploring the building energy impacts of green roof design decisions–a modeling study of buildings in four distinct climates *J. Build. Phys.* **35** 372-391

Salamanca F, Krpo A, Martilli A and Clappier A 2010 A new building energy model coupled with an urban canopy parameterization for urban climate simulations—part I. formulation, verification, and sensitivity analysis of the model *Theor. Appl. Climatol.* **99** 331-344

Santamouris M 2014 Cooling the cities - A review of reflective and green roof mitigation technologies to fight heat island and improve comfort in urban environments *Sol. Energy* **103** 682-703

Sastre M, Yagüe C, Román-Cascón C and Maqueda G 2015 Atmospheric boundary-layer evening transitions: a comparison between two different experimental sites *Boundary-Layer Meteorol.* **157** 375-399

Schatz J and Kucharik C J 2015 Urban climate effects on extreme temperatures in Madison, Wisconsin, USA *Environ. Res. Lett.* 10 094024

Schwartz B and Govett M 1992 A hydrostatically consistent North American radiosonde data base at the forecast systems laboratory, 1946–present (NOAA technical memorandum) *NOAA Forecast Syst. Lab. Boulder*

Seneviratne S-I, Corti T, Davin E L, Hirschi M, Jaeger E B, Lehner I, Orlowsky B and Teuling A J 2010 Investigating soil moisture–climate interactions in a changing climate: A review *Earth Sci. Rev.* **99** 125-161

Seneviratne S I, Lüthi D, Litschi M and Schär C 2006 Land–atmosphere coupling and climate change in Europe *Nature* **443** 205-209.

Seneviratne S I and Stöckli R 2008 The role of land-atmosphere interactions for climate variability in Europe. In *Climate Variability and Extremes during the Past 100 years* Springer Netherlands 179-193.

Sharma A, Conry P, Fernando H J S, Hamlet A F, Hellmann J J and Chen F 2016 Green and cool roofs to mitigate urban heat island effects in the Chicago metropolitan area: evaluation with a regional climate model *Environ. Res. Lett.* 11 064004

Skamarock W C and Klemp J B 2008 A time-split non-hydrostatic atmospheric model for weather research and forecasting applications *J. Comput. Phys.* **227** 3465-3485

Song J and Wang Z-H 2015a Interfacing the urban land–atmosphere system through coupled urban canopy and atmospheric models *Boundary-Layer Meteorol.* **154** 427–48

Song J and Wang Z-H 2015b Impacts of mesic and xeric urban vegetation on outdoor thermal comfort and microclimate in Phoenix, AZ *Build. Environ.* **94** 558–68

Song J and Wang Z-H 2016a Evaluating the impact of built environment characteristics on urban boundary layer dynamics using an advanced stochastic approach Atmos. Chem. Phys. **16** 6285-6301

Song J, Wang Z-H 2016b Diurnal changes in urban boundary layer environment induced by urban greening. *Environ. Res. Lett.* (Accepted).

Song J, Wang Z-H, Myint SW, Wang C 2016a Revisiting the surface-air temperature relationship in an arid urban environment *Int. J. Climatol.* (under review).

Song J, Wang Z-H, Wang C 2016b Analyzing biospheric and anthropogenic contributors to atmospheric CO_2 variability in a desert city *Atmos. Environ.* (under review).

Song J, Xia J, Zhang L, Wang Z-H, Wan H, She D 2016c Streamflow prediction in ungauged basins by regressive regionalization: a case study in Huai River Basin, China *Hydrol. Res.* **47** 1053-1068

Spronken-Smith R A and Oke T R 1998 The thermal regime of urban parks in two cities with different summer climates *Int. J. Remote Sens.* **19** 2085–104

Spronken-Smith R A and Oke T R 1999 Scale modelling of nocturnal cooling in urban parks *Boundary-Layer Meteorol.* **93** 287-312

Stensrud D J 2009 Parameterization schemes: keys to understanding numerical weather prediction models Cambridge University Press 459pp

Stull R B 1988 An introduction to boundary layer meteorology Kluwer, Dordrecht 666 pp

Stull R B 1991 Static stability-an update *Bull. Amer. Meteor. Soc.* **72** 1521-1529

Sukoriansky S, Galperin B and Perov V 2005 Application of a new spectral theory of stably stratified turbulence to the atmospheric boundary layer over sea ice *Boundary-Layer Meteorol.* **117** 231-257

Sun T, Bou-Zeid E, Wang ZH, Zerba E and Ni GH 2013a Hydrometeorological determinants of green roof performance via a vertically-resolved model for heat and water transport *Build Environ.* **60** 211-224

Sun T, Wang ZH and Ni GH 2013b Revisiting the hysteresis effect in surface energy budgets *Geophys. Res. Lett.* **40** 1741-1747
Susca T, Gaffin S and Dell'Osso G 2011 Positive effects of vegetation: Urban heat island and green roofs *Environ. Pollut.* **159** 2119–26

Taha H 1997 Urban climates and heat islands: Albedo, evapotranspiration, and anthropogenic heat. Energ. Buildings **25** 99-103

Taha H 2008 Meso-urban meteorological and photochemical modeling of heat island mitigation *Atmos. Environ.* **42** 8795-809

The United Nations (UN) 2012 World urbanization prospects: The 2011 revision, New York, 33 pp

Theeuwes N E, Steeneveld G J, Ronda R J, Heusinkveld B G, van Hove L W A and Holtslag A A M 2014 Seasonal dependence of the urban heat island on the street canyon aspect ratio. *Q. J. R. Meteorol. Soc.* **140** 2197-2210

Theeuwes N E, Steeneveld G J, Ronda R J, Heusinkveld B G, van Hove L W A and Holtslag A A M 2013 Seasonal dependence of the urban heat island on the street canyon aspect ratio *Q. J. R. Meteorol. Soc.* **140** 2197-2210

Thunnissen D P, Au S K and Tsuyuki G T 2007 Uncertainty quantification in estimating critical spacecraft component temperatures *J. Thermophys. Heat Transfer* **21** 422-430

Troen I and Mahrt L 1986 A simple model of the atmospheric boundary layer; sensitivity to surface evaporation *Boundary-Layer Meteorol.* **37** 129–48

Trier S B, LeMone M A, Chen F and Manning K W 2011 Effects of surface heat and moisture exchange on ARW-WRF warm-season precipitation forecasts over the central United States *Weather Forecast* **26** 3-25

Tzoulas K, Korpela K, Venn S, Yli-Pelkonen V, Kaźmierczak A, Niemela J and James P 2007 Promoting ecosystem and human health in urban areas using Green Infrastructure: A literature review *Landscape Urban Plan.* **81** 167-178

Van Genuchten M T 1980 A closed-form equation for predicting the hydraulic conductivity of unsaturated soils *Soil. Sci. Soc. Am. J.* **44** 892-898

Wildmann N, Rau G A and Bange J 2015 Observations of the Early Morning Boundary-Layer Transition with Small Remotely-Piloted Aircraft *Boundary-Layer Meteorol.* **157** 345-373

Wilhelmi O V and Hayden M H 2010 Connecting people and place: a new framework for reducing urban vulnerability to extreme heat *Environ. Res. Lett.* **5** 014021

Wang Z H 2010 Geometric effect of radiative heat exchange in concave structure with application to heating of steel I-sections in fire *Int. J. Heat Mass Transfer* **53** 997-1003

Wang Z H, Bou-Zeid E and Smith J A 2011a A spatially-analytical scheme for surface temperatures and conductive heat fluxes in urban canopy models *Boundary-Layer Meteorol.* **138** 171-193

Wang Z H, Bou-Zeid E, Au S K and Smith J A 2011b Analyzing the sensitivity of WRF's single-layer urban canopy model to parameter uncertainty using advanced Monte Carlo simulation *J. Appl. Meteorol. Climatol.* **50** 1795-1814

Wang Z-H, Bou-Zeid E and Smith J A 2013 A coupled energy transport and hydrological model for urban canopies evaluated using a wireless sensor network *Q. J. R. Meteorol. Soc.* **139** 1643–57

Wang Z-H 2014a Monte Carlo simulations of radiative heat exchange in a street canyon with trees *Sol. Energy* **110** 704–13

Wang Z-H 2014b A new perspective of urban–rural differences: The impact of soil water advection *Urban Clim.* **10** 19-34

Wang Z-H, Zhao X, Yang J and Song J 2016 Cooling and energy saving potentials of shade trees and urban lawns in a desert city, *Appl. Energy* **161** 437-44

Wong N H, Jusuf S K, Syafii N I, Chen Y X, Hajadi N, Sathyanarayanan H and Manickavasagam Y V 2011 Evaluation of the impact of the surrounding urban morphology on building energy consumption *Sol. Energy* **85** 57-71

Yabiku S T, Casagrande D G, and Farley-Metzger E 2007 Preferences for landscape choice in a Southwestern desert city. *Environ. Behav.* **3** 382-400

Yamada T 1979 Prediction of the nocturnal surface inversion height *J. Appl. Meteorol.* **18** 526–31

Yang J and Wang Z-H 2014a Physical parameterization and sensitivity of urban hydrological models: Application to green roof systems *Build. Environ.* **75** 250–63

Yang J and Wang Z-H 2014b Land surface energy partitioning revisited: A novel approach based on single depth soil measurement *Geophys. Res. Lett.*, **41** 8348-8358

Yang J, Wang Z-H, Chen F, Miao S, Tewari M, Voogt J, Myint S 2015 Enhancing hydrologic modeling in the coupled Weather Research and Forecasting - urban modeling system, *Boundary-Layer Meteorol.* **155** 87-109

Yang J, Yu Q and Gong P 2008 Quantifying air pollution removal by green roofs in Chicago *Atmos. Environ.* **42** 7266-7273

Yang Z L 1995 Investigating impacts of anomalous land-surface conditions on Australian climate with an advanced land-surface model coupled with the BMRC-GCM *Int. J. Climatol.* **15** 137-174

Yu C and Hien W N 2006 Thermal benefits of city parks *Energy Build.* **38** 105–20

Zilitinkevich S and Baklanov A 2002 Calculation of the height of the stable boundary layer in practical applications *Boundary-Layer Meteorol.* **105** 389-409

APPENDIX A

CALCULATION OF NET RADIATION IN A STREET CANYON

The net shortwave and longwave radiative fluxes for walls and ground inside a street canyon can be computed using a two-reflection model (Kusaka et al. 2001, Wang et al. 2013) as:

$$S_W = (1-a_W)\begin{bmatrix} S_D \frac{l_{shadow}}{2h} + S_Q F_{W\to S} + S_D\left(\frac{w-l_{shadow}}{w}\right) a_G F_{W\to G} \\ +S_Q F_{W\to G} + S_D \frac{l_{shadow}}{2h} a_W F_{W\to W} + S_Q a_W F_{W\to S} F_{W\to W} \end{bmatrix}, \quad \text{(A1)}$$

$$S_G = (1-a_G)\left[S_D\left(\frac{w-l_{shadow}}{w}\right) + S_Q F_{G\to S} + S_D \frac{l_{shadow}}{2h} a_W F_{G\to W} + S_Q a_W F_{W\to S} F_{G\to W} \right], \quad \text{(A2)}$$

$$\begin{aligned} L_W = {} & \varepsilon_W \left(F_{W\to S} L^{\downarrow} + \varepsilon_G F_{W\to G} \sigma T_G^4 + \varepsilon_W F_{W\to W} \sigma T_W^4 - \sigma T_W^4 \right) + \varepsilon_W (1-\varepsilon_G) L^{\downarrow} F_{G\to S} F_{W\to G} \\ & +2(1-\varepsilon_G)\varepsilon_W \sigma T_W^4 F_{G\to W} F_{W\to G} + \varepsilon_W (1-\varepsilon_W) L^{\downarrow} F_{W\to S} F_{W\to W} \\ & +(1-\varepsilon_W)\varepsilon_G \sigma T_G^4 F_{W\to G} F_{W\to W} + \varepsilon_W \varepsilon_W (1-\varepsilon_W) \sigma T_W^4 F_{W\to W} F_{W\to W} \end{aligned}, \quad \text{(A3)}$$

$$\begin{aligned} L_G = {} & \varepsilon_G \left(F_{G\to S} L^{\downarrow} + 2\varepsilon_W F_{G\to W} \sigma T_W^4 - \sigma T_G^4 \right) + 2\varepsilon_G (1-\varepsilon_W) F_{W\to S} F_{G\to W} L^{\downarrow} \\ & +(1-\varepsilon_W)\varepsilon_G F_{G\to W} F_{W\to G} \sigma T_G^4 + 2\varepsilon_G \varepsilon_W (1-\varepsilon_W) F_{W\to W} F_{G\to W} \sigma T_W^4 \end{aligned}, \quad \text{(A4)}$$

where S_W and S_G are the net shortwave radiative fluxes for wall and ground respectively, L_W and L_G are the net longwave radiative fluxes for wall and ground respectively, S_D and S_Q are the direct and diffuse solar radiative fluxes, a is the albedo (solar reflectivity), $F_{i\to j}$ are the view factors for radiation emitted from a generic surface i and received by surface j, and l_{shadow} is the normalized shadow length. The shadow length is estimated by (Kusaka et al. 2001),

$$l_{shadow} = \begin{cases} h \tan\theta_z \sin\theta_n, & l_{shadow} < w \\ w, & l_{shadow} \geq w \end{cases}, \quad \text{(A5)}$$

where θ_z is the solar zenith angle, θ_n is the difference between the solar azimuth angle and canyon orientation. All view factors for radiative exchange between canyon facets are directly related to the aspect ratio *h/w* (Wang 2010).

APPENDIX B

CALCULATION OF AERODYNAMIC RESISTANCE

Based on Monin-Obukhov similarity theory, the aerodynamic resistance (r_a) can be obtained by (Mascart et al. 1995):

$$r_a = \frac{C}{U_a a^2(z_R) F_h(z_R)} , \tag{B1}$$

$$a^2(z_R) = \frac{\kappa^2}{\left[\ln\left(z_R / z_{mR}\right)\right]^2} , \tag{B2}$$

$$F_h(z_R) = \frac{\ln\left(z_R / z_{mR}\right)}{\ln(z_R / z_{hR})} * \begin{cases} \left(1 - \dfrac{bRi_b}{1 + C_h\sqrt{Ri_b}}\right) & Ri_b \le 0 \\ \dfrac{1}{\left(1 + b' Ri_b\right)^2} & Ri_b > 0 \end{cases} , \tag{B3}$$

$$C_h = a^2 b \frac{\ln\left(z_R / z_{mR}\right)}{\ln\left(z_R / z_{hR}\right)} C_h^* \left(\frac{z_R}{z_{hR}}\right)^{p_h} , \tag{B4}$$

$$\mu = \ln\left(z_{mR} / z_{hR}\right), \tag{B5}$$

$$C_h^* = 3.2165 + 4.3431\mu + 0.536\mu^2 - 0.0781\mu^3 , \tag{B6}$$

$$p_h = 0.5802 - 0.1571\mu + 0.0327\mu^2 - 0.0026\mu^3 , \tag{B7}$$

where U_a is wind speed; κ is the von Karman constant; z_R is the roof elevation; z_{mR} is the roughness length of momentum above roof; z_{hR} is the roughness length of heat above roof; Ri_b is the bulk Richardson number; some empirical constants include C = 0.74, b = 9.4, b' = 4.7 when $Ri_b \le 0.21$, b' = 1 when $Ri_b > 0.21$.